

---

# Revealing nucleosome conformations by AFM imaging and large-scale data analysis

SEBASTIAN FERDINAND KONRAD

---



Munich, September 2021



---

# Revealing nucleosome conformations by AFM imaging and large-scale data analysis

---

DISSERTATION

an der  
Fakultät für Physik  
Ludwig–Maximilians–Universität München

vorgelegt von  
Sebastian Ferdinand Konrad  
aus Landshut



München, 07. Sep 2021

Erstgutachter: Prof. Dr. Jan Lipfert  
Zweitgutachter: Prof. Dr. Steven De Feyter  
Tag der mündlichen Prüfung: 28.10.2021

## Zusammenfassung

Das Genom eukaryotischer Lebewesen wird durch mehrere Kompaktierungsschritte hierarchisch in den Zellkern gepackt, wobei die Bildung sogenannter Nukleosome der erste Schritt ist. Kanonische Nukleosome bestehen aus je zwei Kopien der vier Histone H2A, H2B, H3 und H4, die zusammen das Histonoktamer bilden. Dieses Histonoktamer wird von ca. 147 Basenpaaren DNA umwickelt. Hierbei sorgen elektrostatische Wechselwirkungen und spezifische molekulare Kontakte dafür, dass die DNA fest mit dem Histonoktamer verbunden ist. Allerdings ermöglichen bestimmte, intrinsische Mechanismen dynamische Prozesse im Nukleosom wie beispielsweise das Entlanggleiten an der DNA. Dies geschieht auf Zeitskalen im Bereich von Millisekunden bis Minuten. Die Zugänglichkeit bestimmter Chromatinabschnitte und das Auslesen von Genen wird durch epigenetische Markierungen reguliert. Hierbei spielen vor allem post-translationale Modifikationen (PTMs) eine besondere Rolle. Zahlreiche dieser PTMs beeinflussen die Wechselwirkungen sowohl innerhalb des Histonoktamers als auch zwischen dem Histonoktamer und der DNA, wodurch unterschiedlich stabile und umwickelte Nukleosome entstehen.

Die Rasterkraftmikroskopie stellt eine leistungsfähige Technik zur Untersuchung der Nukleosomstruktur und von Interaktionen des Nukleosoms dar. Sie ermöglicht die Visualisierung einzelner Moleküle ohne Markermoleküle und im Subnanometerbereich. Bisher war es jedoch nicht möglich bestimmte, feine strukturelle Besonderheiten des Nukleosoms wie zum Beispiel die 5 Basenpaar Periodizität der Abwicklung oder die Anti-kooperativität, also den Mechanismus des einseitigen Abwickelns, mit Hilfe der Rasterkraftmikroskopie zu beobachten. Im Rahmen dieser Arbeit, entwickelte ich eine Analysemethodik, die eine schnelle und hochquantitative Auswertung tausender Moleküle mit Einzelmolekülaufösung ermöglicht. Mit Hilfe dieses Arbeitsablaufs konnte ich zum ersten Mal die zuvor genannte 5 Basenpaar Abwicklungsperiodizität und die Anti-kooperativität des Nukleosomes mittels Rasterkraftmikroskopie beschreiben.

Da ich durch diese neu entwickelte Analysepipeline die Möglichkeit hatte, Nukleosomstrukturen mit sehr guter Auflösung zu untersuchen, wandte ich die Methodik daraufhin auf Varianten des kanonischen Nukleosomes an, hierunter beispielsweise Nukleosome, die die Histonvariante CENP-A enthalten, eine Variante die vor allem innerhalb des Zentromers vorkommt, und auf Nukleosome, die kleine post-translationale Modifikationen innerhalb der Histone besitzen. Hierbei erarbeitete ich Einblicke in die mechanistischen Details der jeweiligen Nukleosomvarianten. So fand ich beispielsweise heraus, dass sich sowohl die CENP-A Nukleosome als auch Nukleosome, welche drei zusätzliche Methylgruppen am Endteil des Histons H3 besitzen, überwiegend stochastisch abwickeln, im Gegensatz zu den sich anti-kooperativ abwickelnden Nukleosomen des Wildtyps. Dieses Ergebnis, in Verbindung mit anderen Erkenntnissen der hier vorliegenden Arbeit, zeigt wie verschiedene Histonvarianten und PTMs durch eine Reihe verschiedener Mechanismen ihre Funktion ausüben können.

Zusammenfassend habe ich gezeigt, dass die Rasterkraftmikroskopie in der Lage ist, die Nukleosomstruktur und -dynamik in außerordentlichem Detail zu erfassen. Meine Arbeit führte zu interessanten Erkenntnissen auf dem Gebiet der Epigenetik und wird in Zukunft weitere Einblicke ermöglichen, da der hier entwickelte Arbeitsablauf leicht auf andere Nukleosomvarianten sowie deren Interaktionen mit Bindungspartnern anwendbar ist.

## Abstract

Nucleosomes, the fundamental units of chromatin, regulate readout and expression of eukaryotic genomes. Canonical nucleosome core particles consist of two copies each of the four histone proteins H2A, H2B, H3 and H4 assembled into a histone octamer that is wrapped by ~147 base pairs (bp) of DNA. Electrostatic interactions and specific molecular contacts stably pack the DNA onto the histone octamer but DNA breathing, sliding, gaping, and loosening allow for nucleosomal dynamics on millisecond to minute time scales. Chromatin accessibility and gene readout is heavily regulated by epigenetic marks, among which post-translational modifications (PTMs) of histones play a key role. Numerous PTMs alter histone-histone and histone-DNA interactions, yielding nucleosomal structures with varying degrees of stability and DNA wrapping.

Atomic force microscopy (AFM) is a powerful tool to probe nucleosome structure and interactions due to its capability to image molecular complexes at the single molecule level label-free and with sub-nanometer resolution, well suited to visualize the DNA and protein components of nucleosomes. Yet, so far it was not possible to detect subtle structural features of the nucleosome by AFM such as the 5 bp unwrapping periodicity or the anti-cooperativity of nucleosome unwrapping both of which were previously observed with other measurement techniques. Within this thesis, I developed a high-throughput analysis pipeline that makes possible rapid and highly quantitative assessment of thousands of molecules with single-molecule resolution. Utilizing this workflow, I was able to observe the 5 bp unwrapping periodicity and the anti-cooperativity of nucleosome unwrapping for the first time by AFM imaging.

Being able to study nucleosomal conformations at this level of detail by leveraging the automated multi-parameter analysis approach, I then applied the pipeline to nucleosomes containing the histone variant CENP-A - a variant that often replaces histone H3 in nucleosomes within the centromere - and to nucleosomes that contain subtle post-translational modifications. Here, I was able to unravel the mechanistic details and the effect on nucleosome wrapping of these nucleosome variants. For example, I found that both CENP-A nucleosomes and nucleosomes containing three additional methyl groups within the tail of histone H3 unwrap mostly stochastically, in stark contrast to the anti-cooperative unwrapping of wild type nucleosomes. This finding, in combination with other insights from work within this thesis, highlight how histone variants and PTMs involved in transcriptionally active chromatin act through a range of mechanisms.

In summary, I demonstrated that AFM imaging is able to capture the nucleosome unwrapping landscape in unprecedented detail. My work yielded interesting findings within the field of epigenetics and will allow for additional insights in the future due to the workflow's easy applicability to other nucleosome modifications and variants as well as their interaction with binding partners.

# Contents

|  |             |
|--|-------------|
| <b>Zusammenfassung</b>   | <b>v</b>    |
| <b>Table of Contents</b>   | <b>viii</b> |
| <b>List of Figures</b>   | <b>x</b>    |
| <b>List of Publications</b>  | <b>xiii</b> |
| <b>1 Why we study nucleosomes</b>  | <b>1</b>    |
| <b>2 Atomic Force Microscopy</b>   | <b>5</b>    |
| 2.1 Working principle . . . . .  | 5           |
| 2.1.1 Contact mode . . . . .   | 6           |
| 2.1.2 Tapping mode . . . . .   | 6           |
| 2.1.3 Peak Force Tapping . . . . .   | 7           |
| 2.1.4 Sample environment . . . . .   | 7           |
| 2.2 AFM resolution and fast scanning . . . . .   | 7           |
| 2.2.1 AFM resolution . . . . .   | 8           |
| 2.2.2 High-speed AFM . . . . .   | 9           |
| 2.3 Where to go with the AFM . . . . .   | 9           |
| <b>3 Introduction to DNA and nucleosomes</b>   | <b>11</b>   |
| 3.1 DNA and DNA compaction . . . . .   | 11          |
| 3.2 The nucleosome . . . . .   | 13          |
| 3.2.1 Nucleosome structure . . . . .   | 13          |
| 3.2.2 Nucleosome dynamics . . . . .  | 14          |
| 3.2.3 Nucleosome structure and dynamics by AFM . . . . .   | 17          |
| 3.3 Epigenetics . . . . .  | 19          |
| 3.3.1 Histone tail modifications . . . . .   | 19          |
| 3.3.2 Histone variants . . . . .   | 22          |
| <b>4 A high-throughput pipeline to determine DNA and nucleosome conformations by AFM imaging</b> | <b>25</b>   |
| 4.1 Background . . . . .   | 25          |
| 4.2 Materials and reagents . . . . .   | 26          |
| 4.3 Equipment . . . . .  | 27          |
| 4.4 Software . . . . .   | 27          |
| 4.5 Procedure . . . . .  | 28          |
| 4.5.1 Surface deposition of the sample . . . . .   | 28          |

|          |   |            |
|----------|---|------------|
| 4.5.2    | AFM imaging of nucleosomes and DNA . . . . .  | 30         |
| 4.5.3    | AFM image analysis . . . . .  | 34         |
| 4.6      | Notes . . . . .   | 37         |
| <b>5</b> | <b>High-throughput AFM analysis reveals unwrapping pathways of H3 and CENP-A nucleosomes</b>              | <b>39</b>  |
| 5.1      | Introduction . . . . .  | 39         |
| 5.2      | Results . . . . .   | 41         |
| 5.2.1    | Automated AFM image analysis to quantify nucleosome conformations . . . . .                               | 41         |
| 5.2.2    | Identifying wrapping intermediates by multi-parameter analysis . . . . .                                  | 41         |
| 5.2.3    | Opposing effects of salt concentration on nucleosome wrapping . . . . .                                   | 45         |
| 5.2.4    | Histone H3 nucleosomes unwrap anti-cooperatively . . . . .  | 46         |
| 5.2.5    | CENP-A nucleosomes do not follow distinct unwrapping pathways . . . . .                                   | 48         |
| 5.2.6    | Differences in DNA wrapping reconcile conflicting results on CENP-A nucleosomes . . . . .                 | 50         |
| 5.3      | Discussion . . . . .  | 51         |
| 5.4      | Conclusion . . . . .  | 52         |
| 5.5      | Methods . . . . .   | 53         |
| 5.6      | Supplementary Information . . . . .   | 55         |
| <b>6</b> | <b>Quantifying epigenetic modulation of nucleosome breathing by high-throughput AFM imaging</b>           | <b>63</b>  |
| 6.1      | Background . . . . .  | 64         |
| 6.2      | Results . . . . .   | 65         |
| 6.2.1    | Quantifying nucleosome conformations <i>via</i> automated AFM image analysis with deconvolution . . . . . | 65         |
| 6.2.2    | Quantifying nucleosome wrapping populations by multi-parameter analysis. . . . .                          | 67         |
| 6.2.3    | Post-translational modifications alter wrapping of H3K36me3 nucleosomes. . . . .                          | 68         |
| 6.2.4    | Post-translational modifications can affect nucleosome unwrapping pathways. . . . .                       | 70         |
| 6.3      | Discussion . . . . .  | 72         |
| 6.4      | Methods . . . . .   | 75         |
| 6.5      | Supplementary information . . . . .   | 76         |
| <b>7</b> | <b>Conclusion</b>   | <b>83</b>  |
|          | <b>Bibliography</b>   | <b>85</b>  |
| <b>A</b> | <b>Protocols</b>  | <b>103</b> |
| A.0.1    | PCR for nucleosome reconstitution . . . . .   | 103        |
| A.0.2    | Nucleosome reconstitution . . . . .   | 106        |
|          | <b>Acknowledgements</b>   | <b>109</b> |

## List of Figures

|      |   |    |
|------|---|----|
| 2.1  | Nucleosome heights . . . . .  | 5  |
| 2.2  | AFM setup . . . . .   | 6  |
| 2.3  | AFM operating modes . . . . .   | 7  |
| 2.4  | DNA plasmids at base-pair resolution . . . . .                                    | 8  |
| 2.5  | Scheme of the effect of AFM tip convolution . . . . .                             | 9  |
| 2.6  | Myosin walking on an actin filament . . . . .                                     | 9  |
|      |   |    |
| 3.1  | DNA . . . . .   | 12 |
| 3.2  | Electron micrograph of chromatin . . . . .  | 12 |
| 3.3  | Hierarchical chromatin folding . . . . .  | 13 |
| 3.4  | Nucleosome structure and superhelical locations . . . . .                         | 14 |
| 3.5  | Asymmetric unwrapping of the W601 sequence . . . . .                              | 15 |
| 3.6  | Nucleosome structure and superhelical locations . . . . .                         | 16 |
| 3.7  | Salt dependency of nucleosomes . . . . .  | 17 |
| 3.8  | Salt dependency of nucleosomes . . . . .  | 17 |
| 3.9  | Nucleosome unwrapping by HS-AFM . . . . .   | 18 |
| 3.10 | CENP-A nucleosome loop-formation . . . . .  | 18 |
| 3.11 | Overview of analysis frameworks . . . . .   | 20 |
| 3.12 | Histone tails and their modifications . . . . .                                   | 21 |
| 3.13 | CENP-A vs. histone H3 . . . . .   | 23 |
|      |   |    |
| 4.1  | Surface deposition . . . . .  | 28 |
| 4.2  | Mounting the sample in the AFM . . . . .  | 30 |
| 4.3  | AFM software and settings for imaging . . . . .                                   | 31 |
| 4.4  | DNA length as a quality control parameter . . . . .                               | 33 |
| 4.5  | Plane correction of AFM images . . . . .  | 34 |
| 4.6  | Image analysis post-processing software . . . . .                                 | 35 |
| 4.7  | Example analysis of DNA and nucleosome conformations . . . . .                    | 36 |
| 4.8  | DNA length and nucleosome volume as quality control parameters . . . . .          | 37 |
|      |   |    |
| 5.1  | DNA and nucleosome structure parameters by automated AFM image analysis . . . . . | 42 |
| 5.2  | Structure parameters for H3 nucleosomes from AFM imaging . . . . .                | 43 |
| 5.3  | Nucleosome heights . . . . .  | 43 |
| 5.4  | Assigning nucleosome wrapping states . . . . .                                    | 44 |
| 5.5  | Effect of salt concentration on H3 nucleosome wrapping . . . . .                  | 46 |
| 5.6  | Nucleosomes and magnesium . . . . .   | 46 |
| 5.7  | Anti-cooperative unwrapping of H3 nucleosomes . . . . .                           | 47 |
| 5.8  | Unwrapping and heights of CENP-A nucleosomes . . . . .                            | 49 |
| 5.9  | Detection efficiency, manual molecule classification, and DNA length . . . . .    | 56 |

|      |  |     |
|------|--|-----|
| 5.10 | DNA and nucleosome simulations to quantify the effect of AFM tip convolution . . . | 57  |
| 5.11 | Effect of salt concentration on DNA contour and persistence length . . . . .       | 58  |
| 5.12 | Surface functionalization control . . . . .  | 59  |
| 5.13 | Determination of the occupancies of different wrapping states . . . . .            | 60  |
| 5.14 | Non-palindromic nature of the W601 positioning sequence . . . . .                  | 61  |
| 5.15 | W601 nucleosome positioning . . . . .  | 62  |
| 6.1  | Automated AFM image analysis with deconvolution . . . . .                          | 66  |
| 6.2  | Estimation of nucleosome wrapping populations . . . . .                            | 67  |
| 6.3  | DNA wrapping populations of post-translationally modified nucleosomes . . . . .    | 69  |
| 6.4  | Unwrapping pathways of post-translationally modified nucleosomes . . . . .         | 71  |
| 6.5  | Tracing of bare DNA and nucleosomes . . . . .                                      | 77  |
| 6.6  | Tip shape estimation . . . . .   | 78  |
| 6.7  | Bare DNA lengths . . . . .   | 79  |
| 6.8  | Quantification of anti-cooperative unwrapping . . . . .                            | 80  |
| 6.9  | Nucleosome positioning . . . . .   | 81  |
| 6.10 | Simulation of anti-cooperative and stochastic unwrapping . . . . .                 | 82  |
| A.1  | Agarose gel after PCR . . . . .  | 104 |





## List of Publications

### Publications included in this work

- Sebastian F. Konrad, Willem Vanderlinden, Wout Frederickx, Tine Brouns, Bjoern Menze, Steven De Feyter and Jan Lipfert. High-throughput AFM analysis reveals unwrapping pathways of H3 and CENP-A nucleosomes. *Nanoscale*, Feb 2021, 13, 5435-5447  
<https://doi.org/10.1039/D0NR08564B>
- Sebastian F. Konrad, Willem Vanderlinden, and Jan Lipfert. A High-throughput Pipeline to Determine DNA and Nucleosome Conformations by AFM Imaging. *Bio-protocol*, in press, [no link available yet](#)
- Sebastian F. Konrad, Willem Vanderlinden, and Jan Lipfert. Quantifying epigenetic modulation of nucleosome breathing by high-throughput AFM imaging. *Under review at Biophysical Journal*, Preprint at bioRxiv: <https://doi.org/10.1101/2021.07.29.454136>

### Publications not included in this work

- Tine Brouns, Herlinde De Keersmaecker, Sebastian F. Konrad, Noriyuki Kodera, Toshio Ando, Jan Lipfert, Steven De Feyter and Willem Vanderlinden. Free Energy Landscape and Dynamics of Supercoiled DNA by High-Speed Atomic Force Microscopy. *ACS Nano*, Dec 2018, <https://doi.org/10.1021/acsnano.8b06994>
- Willem Vanderlinden, Pauline Kolbeck, Wout Frederickx, Sebastian F. Konrad, Thomas Nicolaus, Carola Lampe, Alexander S. Urban, C. Moucheron and Jan Lipfert. Ru(TAP)<sub>3</sub><sup>2+</sup> uses multivalent binding to accelerate and constrain photo-adduct formation on DNA. *Chemical Communications*, Jul 2019, <https://doi.org/10.1039/c9cc02838b>
- More publications I contributed to, such as work on the bending of DNA "teardrops" and a project that looks into the interaction between nucleosomes and LEDGF, are in preparation.



# 1

## Why we study nucleosomes

In 2017, about 167 million people worldwide suffered from a major depressive disorder with up to 20 % of people, depending on the country of living, being affected by depression at some point in life<sup>1</sup>. In 2018, approximately 18 million deaths per year were caused by cancer making it responsible for 1 out of 6 deaths worldwide that year<sup>2</sup>. In the same year, Alzheimer's disease was the sixth leading cause of death in the US with a total of 5.8 million people above 65 suffering from Alzheimer's in total<sup>3</sup>.

Something that all of these terrible diseases and disorders have in common is their close relation to epigenetics<sup>4-6</sup> according to ongoing research. In short, epigenetics describes processes and mechanisms that control gene activity by small chemical changes and modifications to the DNA or histones without changing the DNA sequence itself<sup>7</sup>. For example, a study found and related decreased histone H3 acetylation levels, followed by a persistent increase, to depression when studying parts of the limbic brain of depressed humans postmortem<sup>8</sup>. Similarly, work on cancer cells found regions in the DNA that were excessively methylated and therefore causing genes to be wrongfully silenced<sup>9</sup>.

Over the last two decades, a lot of effort has been put into understanding the mechanisms and modes of action behind epigenetics<sup>10;11</sup> and also into the utilization of this knowledge for therapeutic purposes<sup>12</sup>. Current clinical trials for the treatment of cancer, for example, involve histone deacetylase inhibitors that lead to changes in the epigenome<sup>13</sup>. Overall, epigenetic therapies are currently a major field of research, that bears immense hope for the treatment of manifold diseases<sup>14</sup> and gave rise to an abundant number of companies that try to bring drugs and therapies based on epigenetic principles to the market.

Unfortunately, our current understanding of epigenetics is still far from complete with researchers around the globe trying to gain deeper insights into the mechanistic details and the biological implications of epigenetics. While studies that investigate epigenetic modification on the genome level allow for a better understanding of epigenetics on the larger scale, combination of these findings with work on the

biomolecular level are necessary to enable a broad understanding of the working principles of the epigenome in the future. The epigenome is the umbrella term for all the chemical modifications to the DNA and histone proteins of an organism that incorporate an additional layer of information above the genome. Herein, the compaction of DNA into the cell nucleus and the accessibility of DNA confined within nucleosomes as the basic units of compaction play a key role. Therefore, studies of the implications of epigenetic modifications on short stretches of DNA and their effect on the compaction of DNA into the cell nucleus on the nucleosomal level are of specific interest as they might enable a better understanding of the mode of action of epigenetic processes such as gene activation or silencing by partially exposing or hiding DNA stretches from the transcription machinery<sup>15;16</sup>.

The goal of this work is to develop an experimental workflow that allows to study the nucleosomal structure in detail to enable investigation of both the structure and the unwrapping dynamics of the nucleosome in unprecedented detail in general and to enable the investigation of the effect of epigenetic modifications on the single-molecule level. Having this experimental pipeline established, a thorough investigation of nucleosome structure and dynamics for wild type and epigenetically modified nucleosomes will provide a first step towards a better understanding of the mechanistic details behind nucleosomes specifically and epigenetics in general.

### **Outline of this thesis**

In chapter 2, an introduction to the main experimental method applied in this work - the atomic force microscope (AFM) - is given. First, the working principle and the main modes of operation of common AFM systems are discussed. Second, a current view on AFM image resolution and high-speed AFM is given.

In chapter 3, DNA and the need for DNA compaction mechanisms within the cell nucleus are introduced. While giving a quick overview of the hierarchical packing of DNA, the first step of DNA compaction - the wrapping of DNA around a histone octamer to form a nucleosome - is elucidated in detail. Here, both nucleosome structure and dynamics are presented in the light of the current state of research on the single molecule level and by different experimental techniques. Afterwards, epigenetics and its effect on nucleosome structure and its biological implications are introduced concluding with open questions that will be investigated throughout this work.

In chapter 4, a detailed description of the experimental methods and the subsequent data analysis used in this work is given. The workflow described here provides enough detail to readily reproduce the experiments performed throughout this work and to apply it to other open research questions that will be stated in more detail in the outlook.

In chapter 5, the atomic force microscopy imaging and readout workflow presented in chapter 4 is applied to wild type and CENP-A nucleosomes, proving the capabilities of our analysis pipeline and elucidating new mechanistic details behind the wrapping of the respective nucleosomes.

In chapter 6, epigenetically modified nucleosomes containing subtle changes to their amino acids are investigated to provide a better understanding of the modes of action behind several key epigenetic modifications.

Finally, a summary of the findings of this work will be given in chapter 7, stating remaining open questions and defining possible future research goals continuing what was started in this work.



# 2

## Atomic Force Microscopy

In 1981, Gerd Binnig and Heinrich Rohrer - then working at IBM Zurich - invented the Scanning Tunneling Microscope that earned them the Nobel Prize five years later in 1986<sup>17</sup>. In STM, a metal tip is scanned over a conductive surface. Displacements of the metal tip can be captured by monitoring the resulting voltages applied to the piezo-drives that then lead to a topographic picture of the surface<sup>17</sup>. The STM turned out to be able to precisely study the atomic surface structure of conductors. Yet, a technique to study the surface of insulators at the same level of detail was still lacking. Therefore, in 1986, - the year Gerd Binnig became a nobel laureate - Binnig proposed the Atomic Force Microscope (AFM) to study the surface of insulators with a similar working principle as the STM<sup>18</sup> (Fig. 2.1).

### 2.1 Working principle

In contrast to STM where a tunneling current is utilized to extract the topographic surface profile, in AFM, the cantilever deflection that is induced by the interaction force acting on the sharp tip in proximity to the surface is carefully monitored and leading to the surface profile. The AFM tip is usually made of silicon and integrated near the end of an AFM cantilever. The lateral and the vertical position of the AFM cantilever is controlled by a piezoelectric scanner. Deflections of the AFM cantilever when moving over the surface features are tracked by a laser beam reflected from the back of the AFM cantilever. A photodetector collects the reflected laser signal which, in combination with the movement of the piezos, allows generation of the topographic image of the surface. The exact working principle of the image generation depends on the mode of operation of the AFM. Over the years, several techniques have evolved among which contact mode, tapping mode, non-contact mode and the recently emerged peakforce tapping are the most prominent ones.

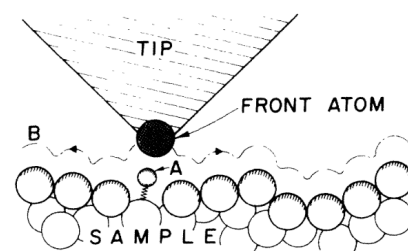
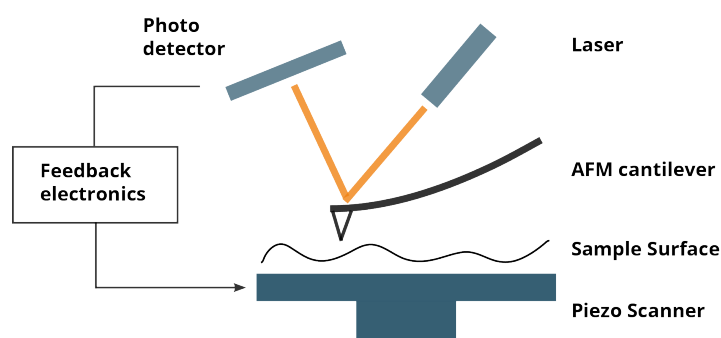


**Figure 2.1:** Schematic of the AFM working principle as originally proposed by Gerd Binnig. Reprinted with permission from<sup>18</sup>. Copyright by the American Physical Society.

**Figure 2.2:** Schematic of the basic components of an AFM setup. A laser is focused onto the back of the very end of the AFM cantilever and is reflected back towards a photo-sensitive detector. While scanning over the surface, the reflection of the laser signal is changing continuously and thus also the signal caught by the detector. A feedback loop controls the vertical extension of the scanner. The coordinates tracked from the AFM tip movement during the scan are used to generate the topographic image of the surface.



### 2.1.1 Contact mode

The mode of operation proposed by Binnig in 1986<sup>18</sup> is called contact mode (Fig. 2.3i). Here, the tip is continuously in contact with the surface under a directly-controlled force. When the tip is moving along the surface, the sample induces a vertical deflection of the cantilever. The feedback loop retains this deflection at a preset loading force and uses the feedback response to generate a topographic image. The main disadvantage of contact mode imaging are the high lateral forces acting on the tip that can degrade the tip quickly and therefore decrease image resolution. Similarly, the forces acting on the sample can cause deformations of the surface and affect the conformation of the molecules under investigation<sup>19</sup>. To reduce the forces acting on the surface, soft cantilevers are used.

### 2.1.2 Tapping mode

In tapping mode or amplitude modulation (AM-AFM), typically a rather stiff AFM cantilever is oscillated near its resonance frequency by a piezoelectric element (Fig. 2.3ii). Typical oscillation frequencies range from kHz up to some MHz in the case of cantilevers that are designed for the purpose of ultrafast oscillation. At the lower end of the AFM cantilever oscillation the tip slightly touches the surface or interacts with it via van der Waals forces and therefore its oscillation amplitude is damped. A feedback loop keeps the oscillation amplitude of the AFM cantilever constant and thus maintains a constant interaction force between the cantilever and the surface<sup>20</sup>. Compared to contact mode, the lateral forces acting on both the molecules under investigation and the AFM tip are drastically reduced<sup>21</sup>.

### Non-contact mode

Similar to the tapping mode, in non-contact mode, the cantilever is oscillated at its resonance frequency (frequency modulation AFM - FM-AFM) at amplitudes of a few nanometers. The AFM tip is kept away from the surface at a distance with van der Waals forces acting on the cantilever and decreasing the resonance frequency of the cantilever. A feedback loop acts to maintain a constant oscillation frequency and tip-sample interaction is monitored directly via a shift in the resonance frequency of the cantilever, instead of monitoring the change in the cantilever amplitude as done in tapping mode<sup>22</sup>. FM-AFM is applied in UHV and low-temperature physics<sup>23</sup> as well as in biological applications<sup>24</sup>. The advantage of FM-AFM is that it offers the lowest possible interaction between the AFM tip and the sample under investigation. When tuned properly, the shape can be preserved over long times allowing

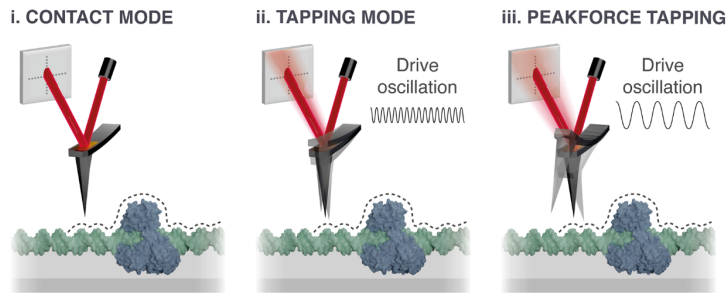


**Figure 2.3:** The main modes of operation in AFM are depicted: contact mode, tapping mode and peakforce tapping. Figure adapted from<sup>22</sup> - licensed under CC BY 4.0.

continuous scanning at high resolution.

### 2.1.3 Peak Force Tapping

A variation compared to the other imaging modes to map the surface is taken in the Peak Force Tapping (PFT) mode that was first proposed in 2009<sup>25</sup>. In contrast to the other dynamic AFM imaging modes, in PFT, the oscillation of the AFM cantilever is performed way below the resonance frequency<sup>26</sup>. A force curve is recorded at each oscillation and the interaction between the tip and the sample is controlled by a feedback loop. The resulting highest force, i.e. the "peak force" is used to modulate the z-piezo position to keep a constant interaction force between the tip and the sample<sup>22</sup> that can then be used to generate a topographic image of the sample. While being a relatively slow imaging mode when first introduced, nowadays, force curves for PFT can be taken at frequencies up to 10 kHz allowing high-resolution scans of single molecules within a few minutes. The main advantage of peak force tapping is its ability to compensate for drift enabling the continuous measurement of single molecules over extended time periods while preventing damage to the AFM tip.

### 2.1.4 Sample environment

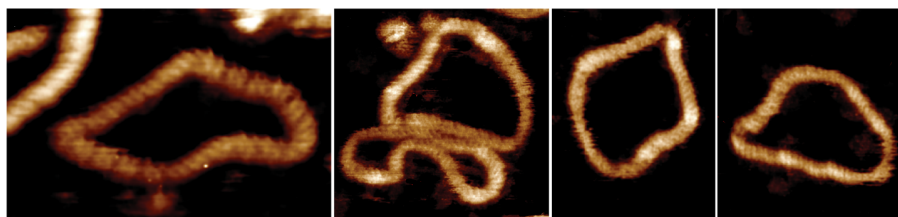
All AFM imaging modes can be performed in air and in liquid. For imaging biological samples in air, the sample is typically deposited in its buffer solution on the surface for a certain incubation time and afterwards the surface is dried with a gentle stream of nitrogen gas. In contrast, for AFM in liquid, the surface is constantly kept wet in a buffer solution and the AFM tip is immersed in liquid. The minimum volume is in the range of microliters that can be contained in a liquid cell or in a droplet formed by the capillary forces between the surface and the cantilever holder.

## 2.2 AFM resolution and fast scanning

Since the first set up of an atomic force microscope, the technique has come a long way making it a reliable, fast and highly resolved imaging tool in research labs around the world. An example of what can currently be achieved with high-end AFM imaging is shown in Figure 2.4. In this work, AFM imaging was used to analyze the effect of supercoiling on DNA flexibility on the base-pair level<sup>27</sup> showcasing the resolution of the AFM at a few Ångstrom.

In principle, AFM image resolution is mainly defined by two elements: The sharpness of the AFM tip and the stability of the AFM system when scanning over an

**Figure 2.4:** High-resolution AFM images of supercoiled DNA minicircles showcasing the potential of AFM to image DNA at base-pair resolution and directly visualizing major and minor grooves. Adapted from<sup>27</sup> - licensed under CC BY 4.0.



extended period of time. Atomic resolution can only be achieved if the AFM tip is terminated with a single atom. At typical tip curvatures with a radius of 10 nm, DNA with a diameter of 2 nm is imaged at a width of ~6 nm.<sup>28</sup>

### 2.2.1 AFM resolution

The effect of overestimating the size of the sample due to the finite size of the AFM tip is called AFM tip convolution (Fig. 2.5) and has been an area of ongoing investigation within the AFM community. The most direct approach to overall increase AFM resolution is to reduce the dimension of the AFM tip and reproducibly produce AFM tips of the same shape. However, manufacturing cantilevers is based on chemical processes, such as etching, making every cantilever unique. There are many different AFM probe manufacturers on the market that all offer a wide range of AFM cantilevers for manifold applications. For example, typically small cantilever spring constants (0.1 - 3 N/m) are used in liquid AFM measurements whereas dry imaging typically requires larger spring constants in the range of 5 - 30 N/m. In the product sheets of the respective cantilevers, the tip radius is usually not specified as an exact value but rather as a range. For example, FASTSCAN-A cantilevers manufactured by Bruker, that we commonly use in our dry AFM measurements, are specified to have a nominal tip radius of 5 nm with a maximum value of 12 nm. Only when using the individual AFM tip during a measurement run, the final resolution with that AFM tip becomes apparent.

Besides the direct approach of improving AFM tips, work has been put into estimating the effect of AFM tip convolution on biological molecules<sup>29-31</sup> and consecutively applying deconvolution algorithms. However, to apply a deconvolution to the AFM image, good knowledge of the AFM tip shape is required. The two main approaches to estimate the AFM tip shape are either experimental methods in which well known calibration structures are used to extract the tip shape or mathematical approaches that utilize the final AFM image to perform a blind tip reconstruction<sup>32-34</sup>. Two example studies for estimating the AFM tip shape experimentally are based on a calibration grid etched onto a silicon wafer<sup>35</sup> or on the thermally stable, non-abrasive tobacco mosaic virus that can be deposited next to other biological molecules and act as a calibration structure<sup>36</sup>.

In the work presented here, a blind tip reconstruction approach based on the experimentally taken AFM images is utilized to estimate the AFM tip shape and consecutively apply a deconvolution for more accurate tracing of the structural parameters of DNA and nucleosomes. A detailed description of the method and the results is given in Chapter 6.

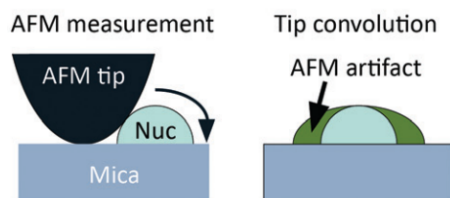


**Figure 2.5:** AFM tip convolution results in an overestimation of the dimensions of biological molecules. In this case, a nucleosome deposited on a flat mica surface is imaged with an AFM tip of finite dimensions. Convoluting the shape of the AFM tip with the actual shape of the molecule under investigation results in the final image obtained by the AFM.

### 2.2.2 High-speed AFM

X-ray crystallography, cryo-EM and NMR had great impact in providing high-resolved structures of DNA and a wide range of biological molecules. However, it is still often difficult to study the dynamics of the respective molecules in a direct approach, i.e. label-free and by directly visualizing the sample under investigation. AFM is a method that is capable of directly visualizing biological samples at high resolution and without the need of additional markers<sup>37</sup>. Yet, one critical factor to study the dynamics of molecules is the ability to enable fast scan speeds and thus capture slight movements or conformational changes over time. To enable these high scan speeds for AFM, a lot of effort has been put into optimizing the various components of AFM setups over the years<sup>38;39</sup>. Based on these efforts the response speed of all the components of the AFM to the feedback loop has been drastically reduced including the development of short cantilevers, with small spring constants and high resonance frequencies<sup>40</sup> or dynamic feedback controllers that reduce the impact of the AFM tip on the sample during fast scanning<sup>41</sup>.

While AFM scanning speed has increased continuously over time and there is no clear definition of the required scanning speed for high-speed AFM (typically a few frames per second), the term "High-speed AFM" has first been established in a study from 2008 with an imaging speed of 10-30 frames/s (fps). However, the number of frames measured per second very much depends on the amount of pixels and scan lines imaged per second<sup>43</sup>. For example, walking of myosin on an actin filament was captured in a famous high-speed AFM study imaging at 7 fps over 150 x 75 nm<sup>2</sup> (Fig. 2.6).<sup>42</sup> Due to the commercial availability of high-speed AFM systems and AFM cantilevers, the amount of studies utilizing high-speed AFM for protein investigation has increased significantly<sup>44</sup>. High-speed AFM has also extensively been used to study DNA and nucleosomes which are the focus of this thesis. A detailed view of these efforts and their findings will be given in Chapter 3.

### 2.3 Where to go with the AFM

Since its first experimental implementation over 30 years ago, AFM imaging has gone through manifold enhancement cycles and adaptations for a wide range of applications. Currently, a broad range of AFM systems from different manufactures all over the world is commercially available with diverse application purposes. From scanning large fields of views with thousands of molecules to scanning intact cells or performing video rate imaging of single proteins, the potential applications for AFM in biomolecular studies seem endless. Combination of AFM with other experimental techniques such as fluorescence microscopy, optical microscopy, Förster resonance energy transfer, or total internal reflection fluorescence is also an active area of research that will likely result in additional use cases to study biomolecules

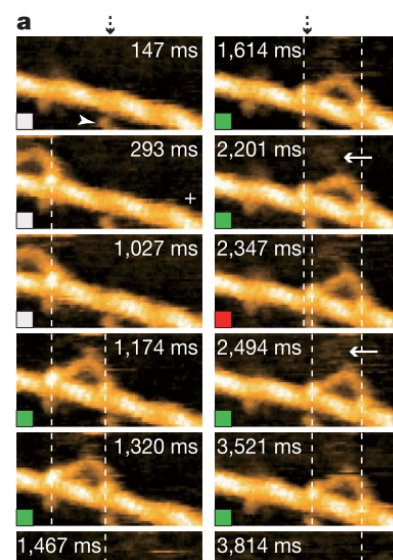


**Figure 2.6:** Subsequent images taken by high-speed AFM of the movement of myosin scanning 7 images per second. Reprinted with permission from<sup>42</sup>. Copyright by Springer Nature.

at unprecedented detail<sup>45</sup>. For example, combination of AFM with optical microscopy is often used to study the mechanical properties of cells or their mechanical interaction with the environment<sup>46</sup>. Additionally, a lot of work is put into pushing the resolution of AFM itself. Only recently, in a study that tries to push the resolution of AFM - they call it localization AFM or LAFM - to the Ångstrom level, a read-out method of AFM images that is somewhat comparable to the working principle behind super-resolution microscopy was proposed and has the potential of taking AFM imaging resolution to the next level<sup>47</sup>.

AFM and many other experimental methods enabled researchers around the globe to gain a detailed understanding of biomolecules on the single-molecular level. This chapter set the foundation to understand and follow the experimental work performed throughout this thesis. In the following chapter, an introduction to DNA, proteins, and nucleosomes in particular is given together with the current status of research regarding nucleosomes. This will provide the framework that has been the starting point of this thesis and will introduce the biological questions that were addressed in the subsequent chapters.

# 3

## Introduction to DNA and nucleosomes

The ability to store, retrieve, and translate genetic information is critical to creating and maintaining a living organism and thus to life in general. At cell division, hereditary information is passed on to the daughter cell. These instructions that make life possible are stored in genes that contain the components required to define the traits of a species as a whole and of the individuals within that species<sup>48</sup>. Deoxyribonucleic acid (DNA) is the carrier of this hereditary information - the human genome - that is compacted into the cell via hierarchical packing with a first step being the formation of nucleosomes. Despite the enormous efforts undertaken to completely decode the human genome in the 90s, it took researchers 50 years until the complete genome was officially decyphered<sup>49</sup> after James Watson and Francis Crick first discovered the double helical structure of DNA<sup>50</sup>. Over the last couple of decades, our knowledge and understanding of DNA, the basic information carrier of life, has increased rapidly. Yet, there is still a vast amount of open questions about DNA in general and the compaction mechanisms of DNA into nucleosomes in particular as the compaction and therefore the accessibility of DNA for transcription plays a key role in cellular processes. In this chapter, an introduction to DNA will be given at first. Afterwards, the mechanism behind compacting DNA with the help of nucleosomes is described and later a detailed view of our current understanding of nucleosome structure and dynamics is presented. The chapter will end with a brief description of the questions on nucleosome structure that were addressed during this thesis.

### 3.1 DNA and DNA compaction

The human genome consists of approximately 3.2 billion base pairs. One base pair consists of two nucleotides, the basic building blocks of DNA. Nucleotides consist of a nucleobase, a phosphate group and a five carbon sugar. The four different nucleobases adenine (A), thymine (T), guanine (G) and cytosine (C) connect to pairs (A + T or G + C) that stack upon each other to form the characteristic DNA double helix (Fig. 3.1). When stacking the base pairs (bp) a rotation perpendicular

**Figure 3.1:** Schematic of the building blocks of DNA. Bonds between nucleotides with bases G and C or A and T form to make up a base pair. Stacking of these base pairs results in the well know double helical structure: The DNA double helix. Reprinted with permission from<sup>48</sup>. Copyright by the American Society of Cell Biology.

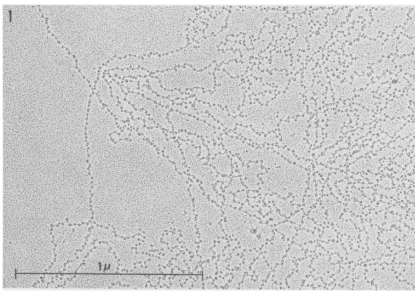
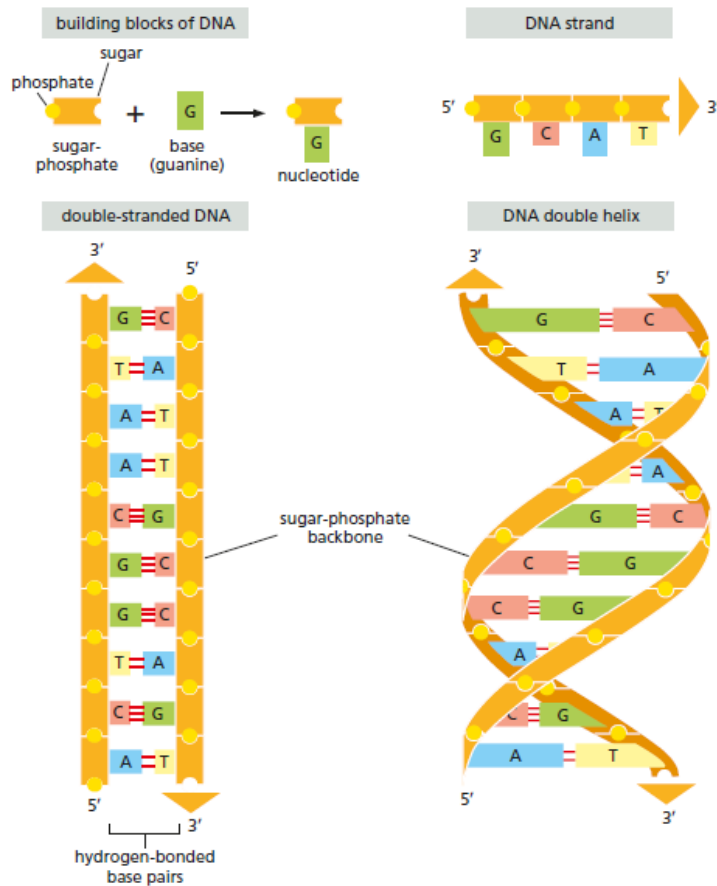


**Figure 3.2:** Electron micrograph of *Drosophila* preblastoderm chromatin, showing proteins wrapped by DNA and linker regions between the proteins. Reprinted with permission from<sup>53</sup>. Copyright by Elsevier.

to the stacking plane is introduced that, in combination with the shape of the nucleotides, leads to void spots in the DNA structure - the major and minor grooves - with a 10.5 bp periodicity. The full human genome of 3.2 billion base pairs corresponds to a length of 2 m DNA ( $\sim 0.34$  nm/bp) that has to be confined within the narrow constraints of the cell nucleus. While knowledge of the existence of the histone proteins was already there for a longer time, a first glimpse on the specific compaction mechanism in play was gained over 40 years ago in the late 1970s. Experiments with micrococcal nuclease (MNase) that digested 'free DNA' but kept DNA tightly wrapped around proteins intact, revealed DNA fragments with certain DNA repeat lengths that, with current knowledge, represent mono-, di- and trinucleosomes<sup>51-55</sup> (Fig. 3.2).

Further research led to our current understanding of the compaction of DNA into the cell nucleus, where DNA is compacted in a hierarchical manner via manifold protein-DNA interactions to finally form compact chromatin. The first step of compaction consists of wrapping of  $\sim 147$  bp of DNA around an octamer of four different histone proteins, the nucleosome. By adding another histone protein, the so called chromatosome is formed, confining  $\sim 167$  bp of DNA in total. Subsequent nucleosome particles are separated by 'free' unbound linker DNA with lengths between 20 bp and 50 bp. Hierarchical folding of the chromatosome via short-range internucleosomal interactions and long-range fiber-fiber interactions leads to compact chromatin<sup>56</sup> (Fig. 3.3). Until recently, it was thought that these nucleosome repeats form the so called 30 nm fiber due to its appearance when reconstituting chromatin in vitro (as depicted in 3.3). However, recent research made it widely accepted

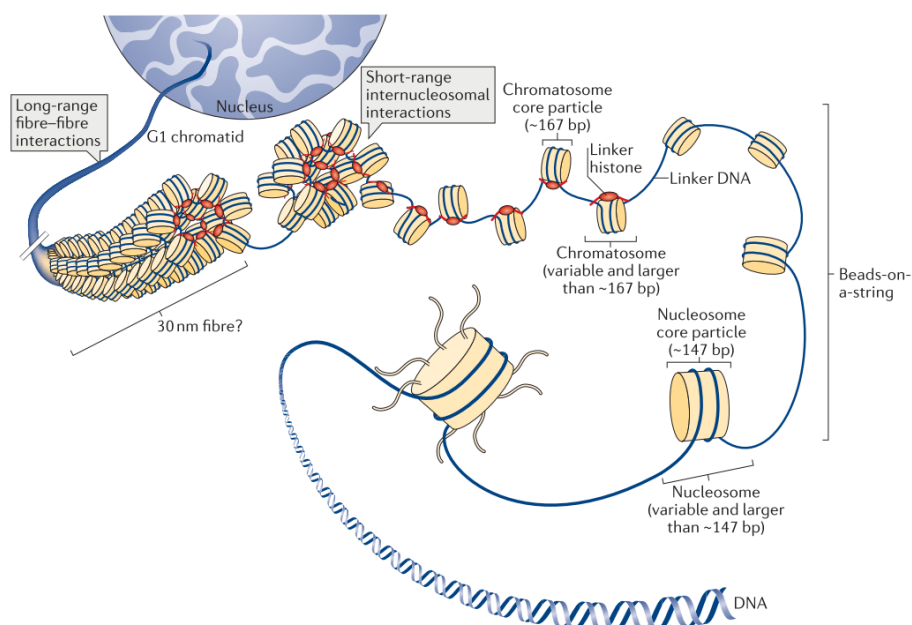


**Figure 3.3:** Manifold levels of chromatin folding. DNA within the nucleus is hierarchically compacted through many histone-DNA interactions. At first, DNA is wrapped in 1.7 turns around the histone octamer and subsequent binding of histone H1 results in the chromatosome. Further compacting interactions result in the formation of larger ordered structures. As indicated by the question mark in the figure legend, it is not clear yet whether the so called 30 nm fiber is the correct structure of compaction of DNA into chromatin. Reprinted with permission from <sup>56</sup>. Copyright by Springer Nature.

that nucleosome fibers do generally not fold into this 30 nm fiber in the nucleus but come in different high-level hierarchical structures and aggregates<sup>55;57</sup>. The resulting compacted DNA is termed chromatin and comes in two main forms: Euchromatin is a lightly packed form of chromatin that has a high density of genes, and is often under active transcription. In contrast, heterochromatin is a more tightly packed form of DNA that can still be transcribed but due to its tight packing it is overall less accessible for the transcription machinery<sup>58</sup>.

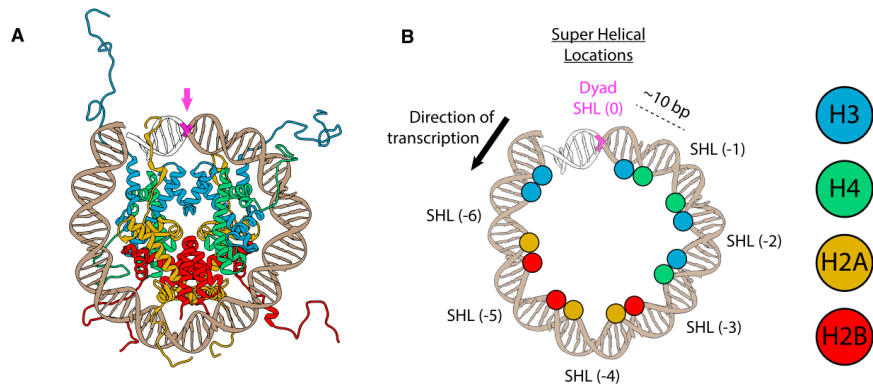
## 3.2 The nucleosome

The first step of DNA folding - the formation of the nucleosome - plays a key role in the mechanism behind chromatin compaction. In 1984, it was possible to resolve the crystal structure of a nucleosome for the first time at 7 Ångstrom, revealing that a canonical nucleosome consists of two copies each of the four histone proteins H2A, H2B, H3 and H4 wrapped by ~146 bp of DNA and thus resulting in a molecular weight of ~206 kDa<sup>59</sup>. Further work subsequently captured the nucleosomal crystal structure at resolutions as high as 1.9 Ångstrom<sup>60;61</sup>. In the following sections, at first a detailed introduction to the nucleosome structure is given (even though it is important to realize that DNA sequence plays a role and that there are now many nucleosome crystal structures<sup>62</sup>). Afterwards, the current state of knowledge of nucleosome dynamics in general and in the light of atomic force microscopy is reviewed to provide a starting point of ongoing research for subsequent chapters. Before completing this chapter, an introduction to epigenetics and their implications on genomics and nucleosome structure are given.

### 3.2.1 Nucleosome structure

Today, the formation of the histone octamer and the wrapping of the DNA around the core particle are well known: The four core histone proteins all share a common structural motif with a folded central region being composed of three  $\alpha$ -helices connected by intervening loops. At the N-terminal end a tail protruding<sup>63</sup>. No-

**Figure 3.4:** A, Rendering of the nucleosome core particle depicting histone H2A (yellow), H2B (red), H3 (blue), H4 (green), and one half of the wrapped nucleosomal DNA. Note the histone tails that protrude from the nucleosome core particle. The magenta arrow indicates the nucleosome dyad. B, The same schematic from A without the core histones to visualize the positions of contacts between the DNA and the histones for the first half of DNA wrapping the histone octamer. The positions of contact are marked according to their superhelical location (SHL) along the DNA starting at the nucleosome dyad. Reprinted with permission from<sup>65</sup>. Copyright by Elsevier



tably, the N-terminal tail of histone H3 is partially folded into another helix ( $\alpha$ -N). H3 and H4 form a tetramer with two copies each of the histones and two H2A-H2B dimers - connected via a 'handshake' motif - interact with the H3-H4 tetramer via H2B-H4 contacts to finally form the histone octamer. This histone octamer is wrapped by 146 bp of DNA in 1.67 left-handed superhelical turns via electrostatic interaction and hydrogen bonds (Fig. 3.4). A recent study utilized ion-counting to demonstrate that nucleosomes have a largely negative electrostatic potential with some stretches of positive charge among the tails and the protein patches<sup>64</sup>. To provide a system for orientation along the DNA path around the histone octamer, superhelical locations (SHL) with respect to the nucleosome dyad - the midpoint of nucleosome wrapping - are defined. SHLs are separated by  $\sim 10$  bp and defined as negative numbers (-1, ..., -7) upstream and positive numbers (+1, ..., +7) downstream of the nucleosome dyad<sup>65</sup> (Fig. 3.4). The predominant contacts between DNA and histone octamer are located around the  $\pm X.5$  locations of the SHL ( $\pm 0.5, \pm 1.5, \dots$ ) where the minor groove of the DNA is facing towards the histone octamer. A high-resolution force-induced unwrapping study based on an optical trap was able to draw three main conclusions about the histone-DNA interaction within the nucleosome core particle<sup>66</sup> **(i)**, A nucleosome has three broad regions of strong interaction located at the nucleosome dyad and approximately both  $\pm 40$  bp upstream and downstream of the dyad, *i.e.* at SHL 0 and between SHL  $\pm 3.5$  and SHL  $\pm 4.5$ . **(ii)**, Unwrapping occurs with a  $\sim 5$  bp periodicity reflecting the major/minor groove periodicity of DNA. **(iii)**, The interaction of DNA and histones is particularly weak at the DNA entry/exit region of the nucleosome. In hindsight, especially observation **(iii)** seems of specific importance for a later set of studies that investigated nucleosome dynamics, an area of research that quickly emerged over the last couple of years. This owes to the fact that nucleosomes are highly dynamic - especially at the arm entry/exit site - and exhibit dynamics on the millisecond to second timescale. In the following section, an introduction to these nucleosomal dynamics and the work that originally described them with different experimental approaches will be given.

### 3.2.2 Nucleosome dynamics

In 1995, a study by Polach and Widom first proposed partial DNA arm unwrapping to enable the binding of specific regulatory proteins to their DNA target sequence<sup>67</sup>. They developed a gel based assay that involves a restriction enzyme that

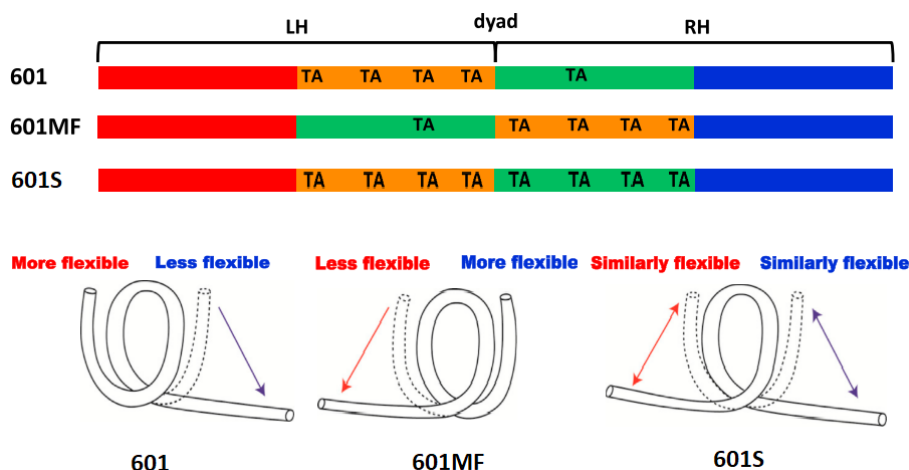


**Figure 3.5:** Illustration of the different versions of the W601 sequence used to study the asymmetry of the nucleosome unwrapping process. Unwrapping occurs only from one side at the same time (anti-cooperativity) and predominantly from the stiffer side, *i.e.* with less AT dinucleotide repeats at the major/minor groove (asymmetry). Flipping the inner part of the sequence (601MF) led to predominant unwrapping from the opposite side and symmetrizing the stiffness of the inner halves (601S) led to similar unwrapping probabilities of each side. Reprinted with permission from<sup>69</sup>. Copyright by Elsevier.

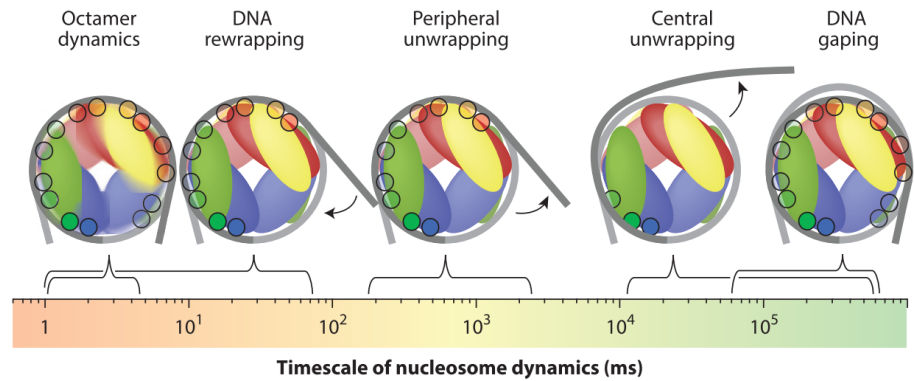
cannot bind to its target DNA sequence hidden within the nucleosome core particle when the nucleosome is fully wrapped. However, they observed that the restriction enzyme will often be able to access its target sequence and cut the DNA leading them to the suggestion that nucleosomes can partially unwrap to expose parts of their wrapped DNA. Today, nucleosome unwrapping has been extensively investigated but is still a matter of ongoing investigation. A recent study based on cryo-EM provided a detailed analysis of the structural rearrangements the nucleosome core particle exhibits when partially unwrapping<sup>68</sup>. About ~10 % of the nucleosomes occurred in states of partial unwrapping. They were then able to separate these partially unwrapped nucleosomes into 7 classes of 5 bp unwrapping steps up to an unwrapping of 35 bp. Importantly, unwrapping of 35 bp resulted in a more flexible H2A-H2B dimer and when unwrapping even more, the dimer seemed to dissociate, showing that DNA is required to stabilize the histone octamer.

Interestingly, Halic and coworkers also observed anti-cooperative unwrapping of the nucleosome core particle, *i.e.* dissociation of the DNA from one nucleosome side inhibiting unwrapping from the other side, and traced it back to structural rearrangements within the histone octamers that lead to a *latch mechanism* on the wrapped side. This anti-cooperative unwrapping was already observed before in a study based on single-molecule force manipulation and FRET<sup>69</sup> where Ngo et al. also found unwrapping predominantly to occur from one specific DNA end owing to the non-palindromic DNA sequence that is wrapping the nucleosomes: the Widom 601 (W601) DNA sequence. The W601 sequence was first described in a study that aimed on finding DNA sequence rules for high affinity histone octamer binding<sup>70</sup> and is currently used in a wide range of in vitro nucleosome experiments.

### The Widom 601 positioning sequence

One of the features of the W601 sequence is a 10 bp periodicity of AT dinucleotides in the central region (see Fig. 5.15). These AT dinucleotides positioned at the minor groove facilitate the winding of the DNA around the histone octamer. However, the dinucleotides are not placed symmetrically with respect to the dyad position of the W601 sequence making one side of the W601 sequence *stiffer* compared to the opposite more *flexible* side (Fig. 3.5). Flipping the inner halves of the W601 sequences led to unwrapping now predominantly occurring on the opposite side and

**Figure 3.6:** Illustration of the different types of reported spontaneous nucleosomal structural changes. The time scale on which the respective dynamics occur are indicated by the scale bar and brackets. Reprinted with permission from<sup>16</sup>. Copyright by Annual Reviews.



when symmetrizing the stiffness of the inner halves of the DNA wrapped around the nucleosome, unwrapping occurred equally likely from both sides<sup>69</sup>. The W601 sequence has an exceptional value for studies of nucleosomes on the single molecule level due to its high affinity to bind to the histone octamer, yet, it is an artificial sequence and a lot of work is put in understanding how DNA sequence might regulate and affect nucleosome positioning and DNA accessibility in vivo<sup>55;71-74</sup>. For example, a recent study based on an advanced DNA cyclization method found that DNA mechanics play a role in codon selection, since codons - sequences that encode the same amino acid - have a varying stiffness and therefore affect nucleosome wrapping and DNA accessibility in general<sup>75</sup>.

### More nucleosome dynamics and their time scales

The time scale of partial nucleosome unwrapping and rewrapping was studied in several studies by different experimental methods such as magnetic tweezers<sup>76</sup>, optical tweezers<sup>77</sup> or stopped-flow fluorescence<sup>78;79</sup> in the presence of the transcription factor LexA and found time constants in the milliseconds to minute range at a wide range of ionic conditions. Besides unwrapping and rewrapping - also termed *nucleosome breathing* -, nucleosomes can also exhibit other dynamic processes (see Fig. 3.9):

(i). During *nucleosome sliding*, the histone octamer moves along the DNA without dissociating from it. To perform sliding, numerous contacts between the wrapped DNA and the histone octamer must be broken. Nucleosome sliding has been observed both triggered by remodeling enzymes<sup>80;81</sup> and just by spontaneous fluctuations<sup>82;83</sup>.

(ii). *Nucleosome gapping* describes a DNA movement of about 5-10 Ångstroms perpendicular to the DNA wrapping plane at the minute time scale and was first predicted theoretically<sup>84</sup> and later observed in a FRET study<sup>85</sup>.

(iii). In *DNA tightening/loosening* the DNA underwraps or overwraps the histone octamer, either decreasing or increasing the amount of DNA bound to the histone core<sup>86</sup>.

(iv). Finally, the histone octamer itself can undergo structural fluctuations both within the stable core particle as well as in the extruding DNA arms as described in recent Cryo-EM<sup>68;87</sup> and NMR studies<sup>88;89</sup>.

All of these different dynamic processes took part in transforming the perception of the nucleosome as described in 2019 by Zhou et al.<sup>90</sup>: "The nucleosome is no

longer considered a simple barrier that blocks access to DNA during transcription and replication. Instead, it serves as a dynamic platform linking and integrating many biological processes.”

### 3.2.3 Nucleosome structure and dynamics by AFM

In addition to the other techniques mentioned in the past few sections such as Cryo-EM, NMR, FRET etc., AFM imaging, both of larger scan areas with single scans or in high-speed applications with video rate imaging of smaller scan areas, is used to study nucleosome structure and dynamics. An overview of previous findings within these AFM nucleosome studies will be given in the following subsections.

#### Salt-dependence of nucleosome wrapping

DNA is carrying two negative charges per base pair resulting in a strong energy barrier when trying to compact DNA due to DNA/DNA self-repulsion<sup>92</sup>. Electrostatic interactions between the net positively charged histone octamer and the negatively charged DNA are a driving factor for the assembly of the nucleosome core particle that is also influenced by the availability of ions that can attenuate electrostatic repulsion or attraction<sup>64</sup>. Early AFM work<sup>93</sup> evaluating the number of DNA turns wrapped in nucleosomes found a substantial decrease in DNA wrapping when comparing images taken at ionic conditions of 50 mM NaCl with and without 5 mM MgCl<sub>2</sub>. Similarly, a recent AFM study of nucleosome wrapping under varying ionic conditions found a substantial increase of nucleosome wrapping in the presence of solely 4 mM MgCl<sub>2</sub> compared to the presence of solely monovalent NaCl at 140 mM<sup>91</sup> (see Fig. 3.7). This led them to the conclusion that Mg<sup>2+</sup> facilitates the crossing of the negatively charged DNA arms right at the DNA entry/exit region and therefore taking on their ”crossed linker” conformation as it is the case in the chromosome when adding histone H1.

#### Chromatosomes

Upon addition of histone H1 - the linker histone - to the nucleosome core particle, the chromatosome is formed. Histone H1 binds to the DNA entry/exit site confining and additional ~10 bp of DNA on each side. An early AFM study on nucleosome wrapping found an increase of a nucleosome population at smaller nucleosome opening angles upon addition of H1<sup>95</sup> in line with previous AFM studies<sup>96;97</sup>. With current understanding, the reduction of the nucleosome opening angle is caused by the overlap of the exiting DNA arms that is introduced upon binding of histone H1 (see chapter 5 for a detailed description of nucleosome opening angles). Recent AFM work that utilizes an automated image analysis platform made similar findings with an increase of wrapping length and a decrease in the opening angle (when converting their opening angles to the same opening angle definition that was used in the previous work) upon addition of histone H1 to wild type nucleosomes<sup>94</sup>. Notably, the same work was also able to show the intrinsic asymmetric unwrapping of the non-palindromic W601 sequence for the first time by AFM.

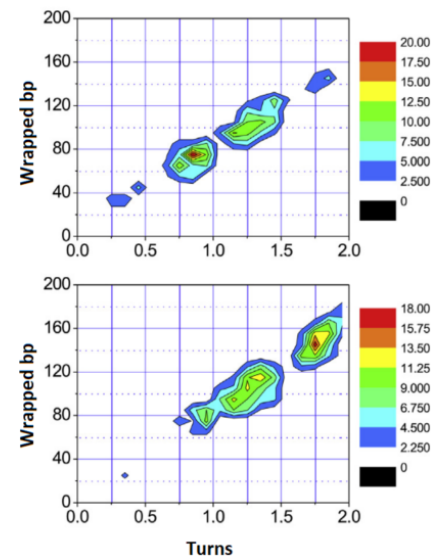


**Figure 3.7:** Plots of wrapped nucleosome DNA length at varying salt concentrations: (Top) 10 mM Tris + 140 mM NaCl, (bottom) 10 mM Tris + 4 mM MgCl<sub>2</sub>. Reprinted with permission from<sup>91</sup>. Copyright by Elsevier.

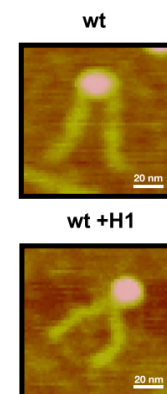
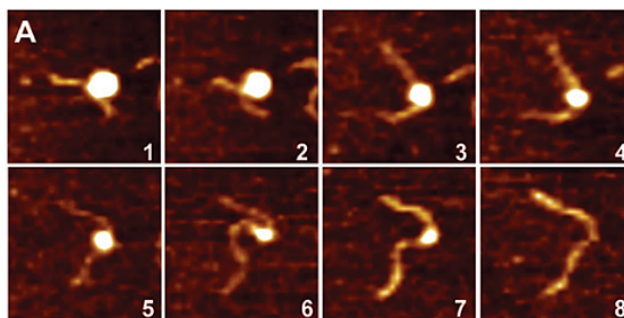


**Figure 3.8:** Example AFM images of a wild type nucleosome without and with the linker histone H1. Reprinted under a CC BY license from<sup>94</sup>. Copyright by Springer Nature.

**Figure 3.9:** Two-step unwrapping process of nucleosomes by high-speed AFM. The consecutive images show the individual steps of DNA unwrapping from the histone octamer. Reprinted with permission from <sup>104</sup>. Copyright by 2009 American Chemical Society.



### Nucleosome heights

The fundamental information that is gained by AFM imaging are the heights of molecules. Logically, AFM has also been used to study the measured height and the compressibility of nucleosomes and several variants. A study that investigated the Young's modulus of CENP-A nucleosomes, centromeric nucleosomes that contain the histone H3 variant CENP-A, found increased elasticity in CENP-A nucleosomes compared to wild type nucleosomes, leading them to the conclusion that CENP-A nucleosomes undergo more substantial structural fluctuations<sup>98</sup>. However, using the directly measured parameter height to draw biological conclusions also has its drawbacks and has to be used carefully. For example, the measurement of the heights of CENP-A<sup>99</sup> compared to wild type nucleosome heights led to some controversy<sup>100–103</sup> about the reliability of heights measured by AFM that depend on the surface chemistry, the ionic conditions and the measurement parameters of the AFM system in use. Still, comparing heights that were imaged under exactly the same conditions will definitely allow for interesting insights into the molecules under investigation.

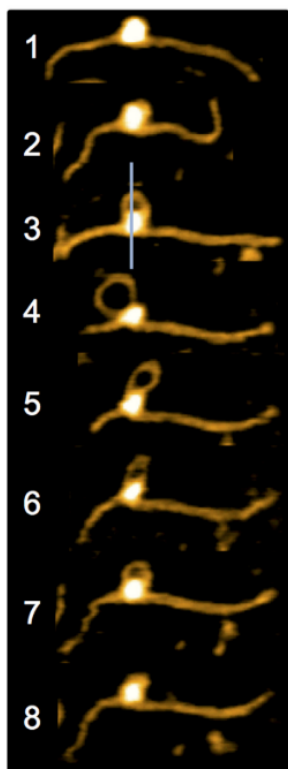


**Figure 3.10:** Spontaneous looping of CENP-A nucleosomes imaged with high-speed AFM. Reprinted with permission from <sup>105</sup>. Copyright by 2017 Oxford University Press.

### Nucleosome dynamics by high-speed AFM

Due to the rapid advancement of the capabilities of AFM to perform video-rate measurements at high resolution, high-speed AFM has been used to study nucleosome dynamics over the last couple of years. Many of these studies were performed by Yuri Lyubchenko and coworkers. Their early work described the sequential unwrapping accompanied by histone octamer dissociation<sup>104</sup> and nucleosome sliding<sup>82</sup>. In more recent work, they investigated the dynamic unwrapping pathways of CENP-A nucleosomes compared to wild type nucleosomes and observed pathways not seen in H3 nucleosomes<sup>105</sup>. Here, formation of DNA loops around the histone octamer was observed for CENP-A nucleosomes and CENP-A histone cores sometimes exhibited large reversible translocations along the DNA of up to 180 bp. For H3 nucleosomes these translocations - *i.e.* nucleosome sliding - have only been observed over short distances of  $\sim 40$  bp<sup>82</sup>.

Besides the findings described above in detail, AFM has also been used to tackle many other questions such as the DNA sequence dependent binding of nucleosomes<sup>106</sup>, the interaction of RNA polymerase and nucleosomes during transcription<sup>107</sup>, and the structure and dynamics of dinucleosomes<sup>108</sup>. Yet, structural studies based on AFM are often still limited by small sample sizes compared to techniques such as cryo-EM and the often still manual data analysis that is tedious and

error-prone. Therefore, several attempts have been undertaken to automate AFM image analysis with tools such as *Gwyddion* and *ImageJ* or custom built software that is often developed for very specific tasks such as the measurement of bend angles of DNA<sup>109;110</sup>, the analysis of nucleosome wrapping and opening angles<sup>94</sup>, or the automated extraction of heights for well defined molecules in images<sup>111</sup>. Developing a versatile tool that is capable of automated analysis of biological molecules with respect to manifold parameters is very difficult to realize and therefore still lacking. An attempt on reliable automated tracing of the structural parameters of nucleoprotein complexes is described and applied in chapters 4, 5 and 6. An overview of the capabilities of several analysis tools and the analyzed parameters of the respective studies - including what the method developed in this work was able to achieve - is given in Fig. 3.11.

### 3.3 Epigenetics

Something that all studies and findings regarding nucleosomal structure and dynamics described in this chapter so far have in common is their focus on wild type nucleosomes (except for quickly mentioning CENP-A nucleosomes). However, epigenetics - the study of heritable phenotype changes that do not involve alterations of the DNA sequence - has developed to a major area of ongoing research as it has become more and more apparent that the epigenome provides an additional layer of information and cell signaling next to the DNA sequence itself<sup>114</sup>. The epigenome is the umbrella term for all the chemical modifications to the DNA and histone proteins of an organism that incorporate this additional layer of information above the genome such as turning on or off certain genes or guiding the transcription machinery within cells. In contrast to the genome, the epigenome is continuously dynamically changed during the cell cycle<sup>7;80</sup>. In the following paragraphs, a quick introduction to some of the wide range of epigenetic modifications will be given together with a close look on the effect of these epigenetic modifications on the structure and dynamics of nucleosomes on the single molecule level. Here, the focus lies primarily on modifications of the histones and the histone tails instead of chemical modifications of the DNA that also play a key role within the epigenome.

#### 3.3.1 Histone tail modifications

First observations of the introduction of acetyl and methyl groups to histones were made in 1964 in experiments concerned with the role of histones in nuclear function<sup>116</sup>. Today, a wide range of epigenetic modifications to the histones is known. Methylation, acetylation and phosphorylation are three key modifications that are observed on manifold locations along the histone tails and the globular domains of the histones (see Fig. 3.12) next to other modifications such as ubiquitination, glycosilation, carbonylation, or citrullination<sup>117</sup>.

##### Acetylation

In histone acetylation, an acetyl functional group is introduced to the amino acid mostly at the N-terminal tail and thereby neutralizing the positive charge of the re-

| Method/Software name  | Our method (no name)  | QuantAFM  | Femtoscan Online and Gwyddion (Preselection of HS-AFM frames with Igor Pro)   | Femtoscan Online   |
|---|---|---|---|--|
| References  | Konrad et al., <i>Nanoscale</i> , 2021; Konrad et al., <i>Bio-protocol</i> , 2021; Konrad et al., <i>bioRxiv</i> , 2021, (DOI: 10.1101/2021.07.29.454136);  | Würtz et al., <i>Scientific Reports</i> , 2019;   | Stumme-Diers et al, <i>NAR</i> , 2018;  | Menshikova et al., <i>Int J Biochem Mol Biol</i> , 2011; Miyagi et al., <i>Biochemistry</i> , 2011;          |
| <b>Demonstrated capabilities</b>                              |   |   |   |  |
| DNA tracing   | ✓   | ✓   | ✓   | ✓  |
| Nucleosome tracing  | ✓   | ✓   | ✓   | ✓  |
| Detection efficiency nucleosomes (depending on image quality) | ~ 95 %  | ~ 65 %  | visual/manual detection   | visual/manual detection  |
| Analyzed nucleosomes  | <i>Nanoscale</i> : > 10,000; <i>bioRxiv</i> : > 25,000;   | ~ 2,500;  | ~ 500 (static nucleosomes) and > 50 movies of nucleosomes (for 5 of those analysis of a several hundred frames is shown ; | several movies and smaller amounts of static nucleosome images (no exact values given)                       |
| Automation  | ✓<br>(manual input possible if desired)   | ✓   | ✗   | ✗  |
| Free DNA contour length                                       | 0.32 ± 0.01 nm/bp (@200 mM NaCl and 10 mM TRIS, pH 7.6)   | 0.34 ± 0.01 nm/bp (@15 mM NaCl, 0.1 mM EDTA, and 10 mM TRIS, pH 7.5)  | 0.32 ± 0.01 nm/bp (@4 mM MgCl <sub>2</sub> and 10 mM HEPES, pH 7.5)   | 0.33 nm/bp (no STD given) (@4 mM MgCl <sub>2</sub> and 10 mM HEPES, pH 7.5)                                  |
| Other features  | Tip deconvolution   | ✗   | ✗   | ✗  |
| Main observations   | 5 bp unwrapping periodicity; asymmetric unwrapping of W601; anti-cooperative unwrapping; stochastic unwrapping of CENP-A and H3K36me3 nucleosomes; Unwrapping landscapes of wildtype, CENP-A and epigenetically modified nucleosomes; | Increased wrapping of chromatosomes; asymmetric unwrapping of W601; opening of nucleosomes with mutated H2A residues; | Reduced wrapping and increases structural dynamics of CENP-A nucleosomes;   | Pathways of nucleosome dynamics and nucleosome sliding; Stabilizing effect of CHAPS on nucleosome structure; |
| <b>Demonstrated parameters</b>                                |   |   |   |  |
| DNA length  | ✓   | ✓   | ✓   | ✓  |
| Nucleosome arm lengths  | ✓   | ✓   | ✓   | ✓  |
| Nucleosome opening angle                                      | ✓   | ✓   | ✗   | ✗  |
| Nucleosome volume   | ✓   | ✗   | ✓   | ✗  |
| Nucleosome height   | ✓   | ✗   | ✓   | ✗  |
| <b>Availability</b>   |   |   |   |  |
| License   | free<br><a href="https://github.com/SKonrad-Science">https://github.com/SKonrad-Science</a>   | free<br><a href="https://github.com/BMCV/quantAFM">https://github.com/BMCV/quantAFM</a>                               | Femtoscan online and Igor Pro are licensed; Gwyddion is freely available  | Femtoscan online licensed  |
| Software requirements   | Python 3 and MS Excel   | MATLAB  | Femtoscan online, Gwyddion, Igor Pro  | Femtoscan online   |

Figure 3.11: Overview of several previously applied analysis frameworks to study nucleosome conformations. The focus of this overview lies on studies that investigated nucleosomes in large, static AFM images or via HS-AFM. Besides the studies mentioned in the overview<sup>82;94;105;112;113</sup>, some other recent nucleosome studies did not specify the analysis tools<sup>91;106</sup> or publish the custom code<sup>83</sup>.

spective amino acid. Histone tails are rapidly undergoing acetylation and deacetylation with an average acetylation event comprising a half-life of a few minutes<sup>118</sup>. Examples of prominent histone acetylations are H3K56ac, an acetylation of lysine 56 of histone H3, and H4K16ac, an acetylation of lysine 16 of histone H4. H3K56ac is linked to regulation of gene expression and transcription and was found to play a role in DNA damage response<sup>119–121</sup>. On the single molecule level, H3K56ac increases DNA accessibility<sup>122</sup> and breathing of the DNA ends<sup>123</sup>. Similarly, H4K16ac is related to gene activation and DNA damage repair<sup>124</sup> and plays a prominent role in controlling chromatin structure and protein interactions<sup>125;126</sup>. The effect of H4K16ac on the structure of nucleosomes on the single molecule level will be investigated in chapter 6 and a more detailed introduction to this modification will

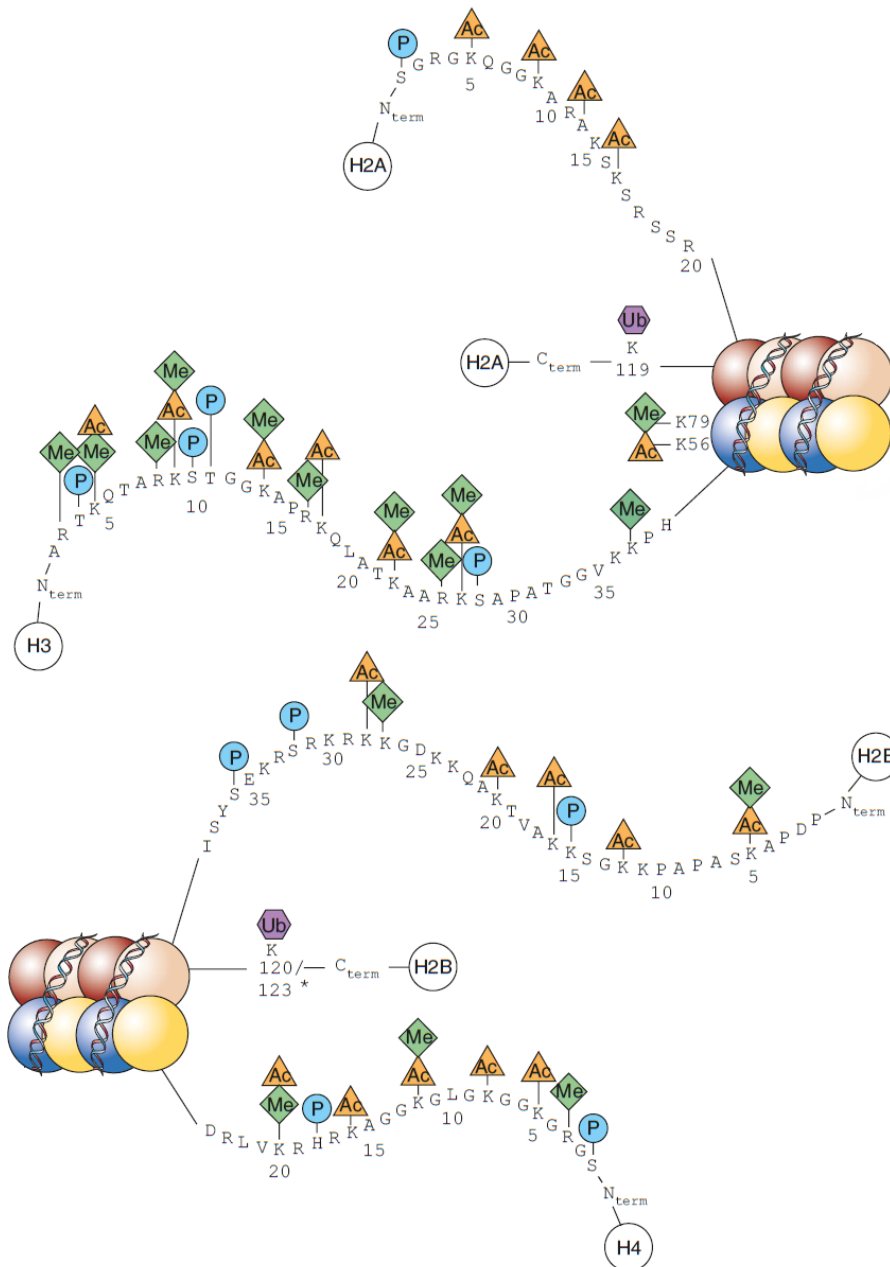


**Figure 3.12:** Common positions of modifications to the histone tails are marked by triangles, squares and circles. Modifications K79 and K56 of histone H3 are located within the globular domain of the histone whereas the other modifications depicted here are located at the histone tails. The modifications include acetylation (Ac), phosphorylation (P), methylation (Me), and ubiquitination (Ub). Figure adapted with permission from <sup>115</sup>. Copyright by 2008 Informa UK Ltd.

be given then.

### Methylation

Methylation does not change the charge of the residue but it alters the hydrophobic character and the overall size of the modified residue <sup>118</sup>. Each methylation adds 14 Daltons to the histone protein. In general, methylation of H3K4, H3K36, and H3K79 is linked to transcriptional activity whereas methylation of H3K9 and H3K27 relates to a repressed state <sup>117</sup>. Interestingly, together with other histone marks, H3K9me3 has also been found responsible for transcriptional elongation <sup>127</sup>, demonstrating the dual role of this marker in transcription on the one hand and in repression on the other hand and thereby showcasing the importance of crosstalk and combinatory effects of the manifold histone modifications. On the single molecule level, methylation has been shown to have an effect on intrinsic nucleosome dynam-

ics such as nucleosome destabilization in the case of H3K64me3 or histone-histone destabilization in the case of H4R92me<sup>15</sup>. A detailed description of the biological implications of H3K36me3 will be given in chapter 6 together with an investigation of the effect of H3K36me3 on the nucleosome structure.

### Phosphorylation

Phosphorylation adds two negative charges and occurs at serine, tyrosine, and threonine residues. A study investigating nucleosomes containing phosphorylation mimics at H3Y41 and H3T45, *i.e.* at the DNA entry/exit region of the nucleosome found increased DNA unwrapping and increased DNA accessibility to transcription factor binding<sup>128</sup>. Similarly, phosphorylation of H3T118 enhances DNA accessibility on the nucleosome dyad and nucleosome mobility<sup>129</sup> in addition to being able to induce the formation of alternative nucleosome arrangements<sup>130</sup>. Other phosphorylations were also linked to gene regulation and DNA repair<sup>118</sup>. In particular, H3S10phos controls mitosis and gene expression and also plays a role in transcriptional activation of numerous genes<sup>131</sup>. A more thorough description of the H3S10phos modification including an investigation of its implication on the nucleosome structure will be given in chapter 6.

Whereas histone tail modifications mostly only introduce small chemical changes to the amino acids of the histone tails, histone variants often introduce significant changes to the amino acid sequence of the respective histones and often have large structural implications on the nucleosome core particle. Examples of histone variants that affect nucleosome structure on the single molecule level or on the chromatin level are H2A.Z that was found to compact chromatin fibers more readily compared to H2A nucleosomes<sup>132</sup> or macroH2A and H2A.Bbd (Barr body deficient) that wrap DNA more stably or more poorly respectively<sup>133;134</sup>. Histone H3.3, a variant of histone H3, is highly enriched in euchromatin<sup>135</sup> and it is suggested that nucleosomes containing H3.3 have a reduced stability compared to H3 containing nucleosomes<sup>136</sup>. A prominent variant of histone H3 is the centromere protein A (CENP-A) that was previously mentioned (see chapter 3 and Fig. 3.13). A high resolution structure of CENP-A containing nucleosomes was first published in 2011 at 3.6 Ångstroms<sup>137</sup>. CENP-A pertains only 48 % sequence identity to the canonical histone H3 and has strong implications for the nucleosome core particle such as reduced DNA wrapping and overall stability. In chapter 5 CENP-A nucleosome structure is investigated by AFM and compared to the structure of H3 containing nucleosomes.

### 3.3.2 Histone variants

Today, the modes of action of many of the previously described histone modifications and variants is still often poorly understood. Due to the abundant amount of diverse modifications in play at the same time and the crosstalk and coupling effects between these modifications, a complete understanding of the processes involved takes enormous effort and is still a matter of ongoing research. A first step towards a better understanding lies in understanding the effects of distinct histone modifications on the single molecule level. However, so far, there's a lack of single molecule

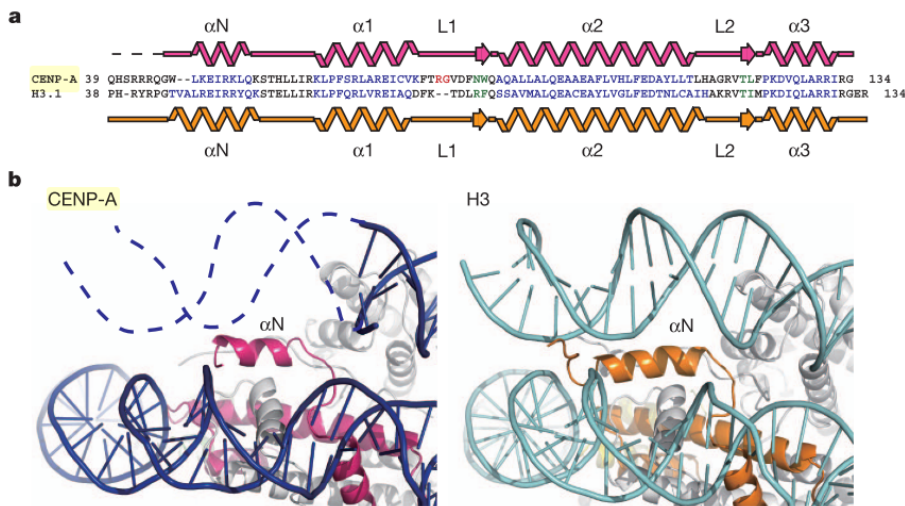


**Figure 3.13:** **a**, The amino acid sequence and secondary structure of CENP-A compared to H3. **b**, The close up view of the crystal structure of CENP-A and H3 nucleosomes show significant differences between the two structures such as the reduced wrapping of DNA and the shorter N-terminal  $\alpha$ -helix. Figure taken with permission from <sup>137</sup>. Copyright by 2011 Springer Nature.

techniques that allow for highly quantitative and reproducible studies while providing sufficient resolution to detect the small changes to the nucleosomal structure and dynamics introduced by these subtle chemical changes. In the following chapters, an easily reproducible and highly quantitative framework based on AFM imaging and automated image analysis is developed for the study of nucleosome structure and the effect of these subtle modifications herein. After proving the strength of the framework in the investigation of wild type nucleosomes, the framework is then subsequently applied to CENP-A nucleosomes and nucleosomes containing the histone tail modifications H3S10phos, H3K36me3, and H4K5/8/12/16ac.



# 4

## A high-throughput pipeline to determine DNA and nucleosome conformations by AFM imaging

Atomic force microscopy (AFM) is a powerful tool to image macromolecular complexes with nanometer resolution and exquisite single molecule sensitivity. While AFM imaging is well-established to investigate DNA and nucleoprotein complexes, AFM studies are often limited by small datasets and manual image analysis that is slow and prone to user bias. Recently, we have shown that a combination of large scale AFM imaging and automated image analysis of nucleosomes can overcome these previous limitations of AFM nucleoprotein studies. Using our high-throughput imaging and analysis pipeline, we have resolved nucleosome wrapping intermediates with 5 base pair resolution and revealed how distinct nucleosome variants and environmental conditions affect the unwrapping pathways of nucleosomal DNA. Here, we provide a detailed protocol of our workflow to analyze DNA and nucleosome conformations focusing on practical aspects and experimental parameters. We expect our protocol to drastically enhance AFM analyses of DNA and nucleosomes and to be readily adaptable to a wide variety of other protein and protein-nucleic acid complexes.<sup>1</sup>

### 4.1 Background

Nucleosomes are the basic units of compaction of eukaryotic DNA into chromatin and function as regulators of gene readout and activity.<sup>15;55;117</sup> Canonical nucleosome core particles consist of two copies each of the four histones H2A, H2B, H3 and H4 assembled into a histone octamer that is tightly wrapped by 147 bp of DNA.<sup>60;138</sup> Accessibility to the genetic code for readout and processing is facilitated by (partial) unwrapping of nucleosomal DNA and can be achieved either by active processes involving e.g. RNA polymerase or nucleosome chaperones that ex-

---

<sup>1</sup>This chapter was reproduced from *Konrad et al., Bio-protocol, 2021, in press*, with permission from Bio-protocol. Author contributions: All authors designed research. S.F.K. performed research, analyzed data, and wrote the manuscript with input from all authors.

ert forces and torques on the nucleosomes<sup>81;139–141</sup>, or spontaneously by thermal fluctuations.<sup>142</sup> Using single-molecule micromanipulation techniques such as optical tweezers, the energetics of force-induced nucleosome unwrapping have been probed at high resolution.<sup>66;69;143–145</sup> However, the unwrapping landscape in the absence of force has been more difficult to access.

Atomic force microscopy (AFM) is a powerful tool to probe nucleosome structure and interactions due to its capability to image molecular complexes at the single molecule level label-free and with sub-nanometer resolution, well suited to visualize the DNA and protein components of nucleosomes.<sup>82;83;104;107;140</sup> Recent improvements in hardware make fast imaging of thousands of molecules possible and combination with automated image analysis enable highly quantitative and reproducible studies of DNA and nucleoprotein complexes.<sup>45;94;110;146;147</sup>

By combining large field of view AFM imaging and automated image analysis of DNA and nucleosomes, we have recently elucidated the nucleosomal wrapping landscape for passive invasion of nucleosomes with linker DNA, in contrast to the previous force-induced unwrapping assays.<sup>112</sup> While we have demonstrated the strength of our methodology by quantitatively capturing the conformational ensemble of wildtype and CENP-A nucleosomes – centromeric nucleosomes where histone H3 is replaced with the CENP-A variant –, the methodology can be easily adapted to study a wide range of open questions such as the effect of post-translational modifications on nucleosome wrapping or the impact of DNA sequence on nucleosome positioning on the single-molecule level.

The current protocol describes all steps necessary to study DNA and nucleosomes by AFM imaging, starting with the surface deposition of the molecules and ending with the quantitative image analysis after AFM imaging. The protocol describes AFM imaging of dry samples in air. However, it can be readily adapted for AFM measurements in liquid. In liquid, the deposition protocol and imaging parameters have to be adjusted. In particular, instead of drying the surface after depositing the sample, the sample buffer solution remains on the surface for imaging. Examples of how to perform liquid AFM measurements have been published previously.<sup>147;148</sup> Subsequent analysis of the AFM images might also require adjustment of the image analysis parameters (see AFM image analysis).

## 4.2 Materials and reagents

### For surface deposition of the sample

1. Mica Grade V-1 25 mm discs (SPI supplies, catalog number: 01926-MB)
2. Marking tape ROTI (Carl Roth, catalog number: 8000.1)
3. 50 ml irrigation syringes (Braun, catalog number: 4617509F)
4. PARAFILM (Carl Roth, catalog number: H666.1)
5. Milli-Q H<sub>2</sub>O (Merck, catalog number: Z00Q0V0WW)
6. Poly-L-lysine (Sigma Aldrich, catalog number: P0879 – diluted to 0.01 % in milli-Q H<sub>2</sub>O)

7. N<sub>2</sub> gas (to blow dry the surface)
8. Protein LoBind Tubes 0.5 ml (Eppendorf, catalog number: 0030108094)
9. DNA/nucleosome sample – prepared as described previously (Krietenstein et al., 2012)
10. Deposition buffer (e.g. 200 mM NaCl + 10 mM TRIS, pH 7.6 – filtered; the concentration of salt can be varied – for example, we have obtained high quality images at 200/50/10 mM NaCl or 50 mM NaCl + 2 mM MgCl<sub>2</sub>, always in 10 mM TRIS, pH 7.6)
11. Petri dishes (Carl Roth, catalog number: 0690.1)
12. Ethanol (Carl Roth, catalog number: T171.4 – diluted to 80 % with milli-Q water)
13. Kimwipes (Kimtech, catalog number: 5511)

#### For AFM imaging

1. Glass slides (Thermo Scientific Menzel, catalog number: 15998086)
2. Double sided adhesive discs (SPI supplies, catalog number: 05095-AB)

### 4.3 Equipment

1. Self-closing tweezers (SPI supplies, catalog number: SN5AP-XD)
2. Vortex mixer (Scientific Industries, catalog number: SU-0236)
3. Centrifuge (to fit 0.5 ml Eppendorf tubes and spin down tube content; Carl Roth, catalog number: T464.1)
4. Tweezers ESD-safe (SPI supplies, catalog number: 0CFT07PE-XD)
5. AFM cantilevers for high-speed imaging in air; we used FASTSCAN-A (resonance frequency 1400 kHz, spring constant 18 N/m; Bruker) or AC160TS (200-400 kHz, 26 N/m; Olympus) cantilevers
6. Imaging AFM; we employed a Nanowizard Ultra Speed 2 (Bruker) and a MultiMode 8 (Bruker)

### 4.4 Software

1. Software to plane-correct the raw AFM data (see section “AFM image analysis”)
2. Microsoft Excel
3. Python 3
4. Software toolbox to analyze DNA and nucleosomes in AFM images (previously described<sup>112</sup> and available for download at the [Github repository](#))

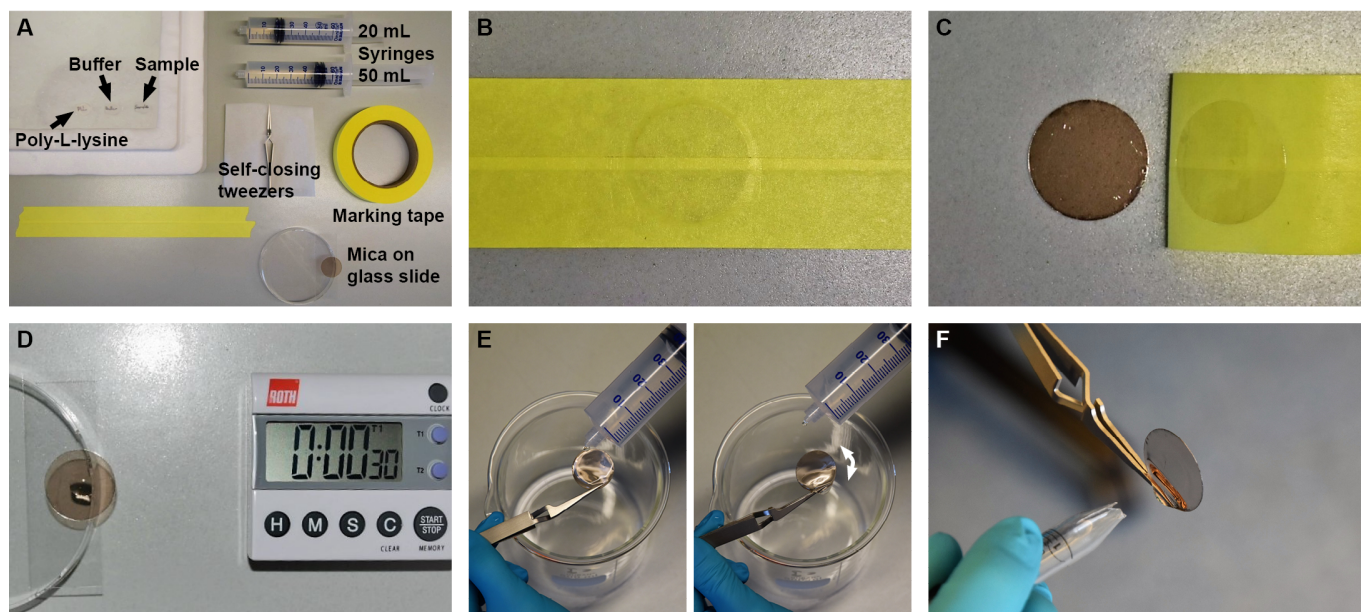


**Figure 4.1: Surface deposition steps.** A, Overview of materials required for the surface deposition of the sample as described in Materials and Reagents. B, A mica disc is placed under marking tape. C, Tearing off the tape removes a layer of the mica plate and leaves behind a flat and clean surface for the subsequent sample deposition. D, Poly-L-lysine and sample solutions are pipetted on the center of the mica plate and incubated for 30 s each, with washing and drying steps E and F directly after each incubation. E, After 30 s of incubation, the surface is rinsed by gently dropping 50/20 ml milli-Q H<sub>2</sub>O of the syringes on the surface and letting it flow off by rotating the mica plate. F, After rinsing, the surface is dried by perpendicularly pointing a nozzle with a gentle stream of N<sub>2</sub> gas onto the surface.

## 4.5 Procedure

### 4.5.1 Surface deposition of the sample

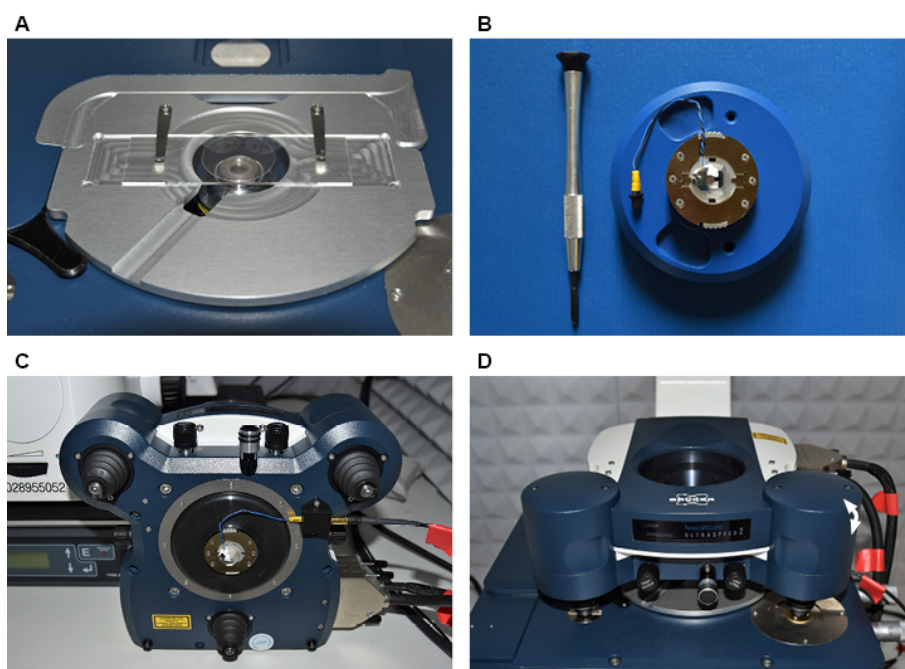
*Note: Contaminations can affect the quality of the imaging surface and thus imaging quality in general. It is therefore important that all instruments are kept clean throughout the process.*

1. Clean the workbench with ethanol and kimwipes thoroughly. Flush the tip of the self-closing tweezers with ethanol and blow-dry the tweezers with N<sub>2</sub> gas. Place the tweezers on a kimwipe such that the tip does not get contaminated and does not touch the bench (Fig. 4.1A).
2. Place two stripes of the marking tape next to each other on the bench with a small overlap (Fig. 4.1A) such that they are wide enough to completely cover the mica disc. Tear off part of the marking tape and put the mica disc underneath. Apply pressure such that the tape fully attaches to the surface of the mica (Fig. 4.1B). Tear off the tape with a quick movement to cleave the mica (Fig. 4.1C). It is important that a full layer of the mica is removed. If only part of a layer was removed or if there are small cracks on the remaining surface, just repeat this step until a whole layer is removed. Store the cleaved mica disc in a petri dish while preparing the next steps.
3. Remove two sterile syringes from their packing and remove the plunger. Make sure that the front of the plunger and the syringe barrel do not make contact anywhere to avoid contamination. Seal the syringe barrels with the clean side

of parafilm and fill with milli-Q water. Place the plunger back in the barrel and press down the plunger such that the parafilm tears and water flows out of the syringes. Remove the parafilm and adjust the plunger such that one syringe holds 50 ml and the other syringe holds 20 ml of milli-Q water. Filling the syringes directly from the storage bottle from the back, as opposed to drawing up fluid with the plunger, helps to avoid contaminations.

4. Prepare a 20  $\mu$ l aliquot of the 0.01 % poly-L-lysine (see Materials and Reagents), shortly vortex it and briefly spin down the content of the Eppendorf tube in a centrifuge (~2 s @ 2000 rpm). Keep the aliquot on ice.
5. Pipette the 20  $\mu$ l poly-L-lysine solution onto the center of the freshly cleaved mica (step 2) and incubate for 30 s (Fig. 4.1D). Make sure not to touch the surface with the pipette. During the 30 s incubation, pick up the mica plate with the self-closing tweezers and pick up the 50 ml syringe and move to a sink or a waste container to be able to start flushing after exactly 30 s. It is important to keep the mica surface horizontal and as still as possible during the movements to ensure a high quality of the surface deposition. Flush the surface by dropping droplets from the syringe on the edge of the mica plate (not in the center where the poly-L-lysine was placed) and periodically tilting the mica plate such that the water flows off (Fig. 4.1E). After flushing with 50 ml, make sure to leave some water on the surface to avoid unintentional drying.
6. With the surface still covered in water, start drying the mica surface with a gentle stream of N<sub>2</sub> gas by quickly tilting the mica surface to a vertical position and targeting the center of the mica with the stream perpendicularly, at about 2 cm distance (Fig. 4.1F). Once the center of the surface is dry, move the stream to the edges until the mica is completely dry.
7. Dilute the sample solution with buffer (in our case 200 mM NaCl + 10 mM Tris) to achieve the desired concentration for surface deposition and incubate on ice for 60 s. Nucleosome samples and buffer are stored at 4 °C and put on ice before starting the surface deposition. A total volume of at least 25  $\mu$ l is required for surface deposition. Diluting 1  $\mu$ l nucleosome/DNA sample solution (containing roughly 30 ng/ $\mu$ l 486 bp DNA and 10 ng/ $\mu$ l histones, corresponding to 120 nM nucleosomes; prepared as described previously<sup>149</sup>) with 40  $\mu$ l buffer solution resulted in a good surface density for AFM imaging (i.e. dense enough to have many molecules in one field of view but not too dense to have too many molecules overlap with each other).
8. After 60 s of incubation on ice, pipette 25  $\mu$ l of the buffered sample solution on the center of the poly-L-lysine coated mica plate and incubate for 30 s. Again, proceed as in steps 5 and 6 rinsing – this time with a 20 ml volume of milli-Q water – and subsequently drying the surface.
9. Store the mica disc in the petri dish at room temperature until starting the AFM measurement. The AFM surface should always be prepared on the measurement day.

**Figure 4.2: Mounting the sample in the AFM.** A, The mica plate with the deposited sample is fixated on a glass slide with three double-sided adhesive discs. The glass side is then placed on the AFM stage. B, The AFM cantilever is mounted onto the glass block that was delivered with the AFM system (Ultra-Speed Glassblock, JPK, catalog number: 22229-E-01). C, Subsequently, the glass block is placed in the designated spot at the bottom of the AFM scanner head. D, To finalize the setup, the scanner head is placed on the AFM stage.



#### 4.5.2 AFM imaging of nucleosomes and DNA

*Note: : The imaging is performed on a Nanowizard Ultraspeed 2 system and the steps presented here will slightly vary for other instruments. The steps to start the measurement are only described briefly since they can be found in the user manual of the respective AFM system in detail. The focus of this section lies on tips and tricks on how to tune AFM imaging and what to look out for to achieve highest image quality for large datasets of DNA and nucleosomes.*

1. To prepare the final imaging surface, place three double-sided adhesive discs on a glass slide while leaving an area in the center free (Fig. 4.2). Place the sample mica plate on the adhesive region such that the central area of the mica aligns with the adhesive free region of the glass slide and apply gentle pressure on the mica above the three adhesive discs, i.e. not in the center where the sample was placed, with the tweezers to fixate the mica more strongly.
2. Install the glass slide with the mica plate on the sample holder of the AFM (Fig. 4.2A).
3. Place the cantilever in the cantilever holder glass block (Fig. 4.2B) and mount the glass block in the AFM scanner head (Fig. 4.2C). Afterwards, place the AFM head on the stage (Fig. 4.2D).
4. Start the JPK SPM Desktop software and select AC Mode Fast Imaging (Fig. 4.3A).
5. Go to the *Setup Experiment* tab and focus the green crosshair on the AFM cantilever tip as seen in the camera view (Fig. 4.3B).
6. Align the laser on the cantilever tip using the screws indicated by the green arrows in Fig. 4.3C to maximize the signal that is collected by the detector. The sum of the collected signal is represented by the blue bar (Fig. 4.3C).

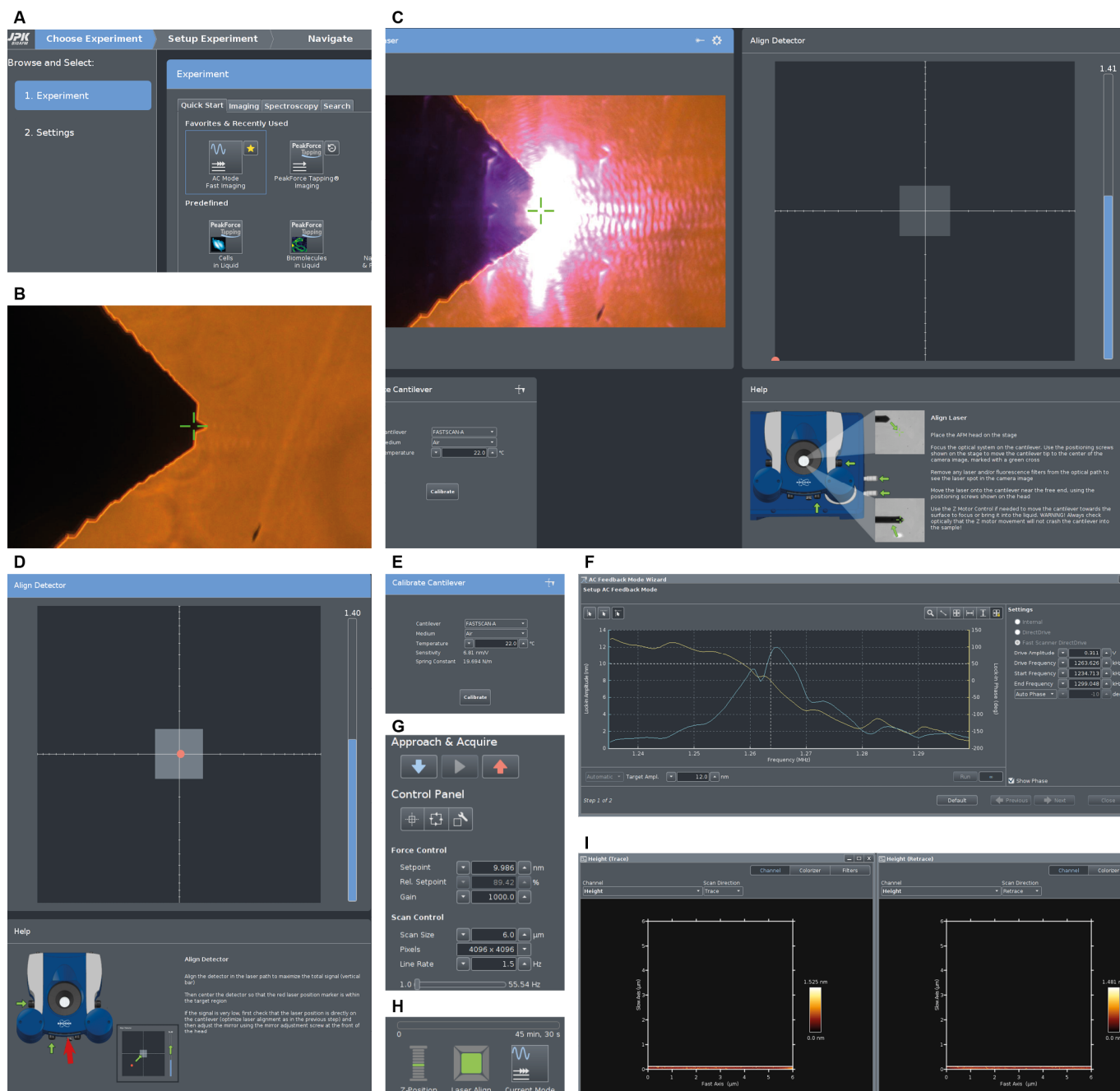


**Figure 4.3: AFM software and settings for imaging.** **A**, The JPK SPM Desktop (7.0.128) software has several imaging modes available. The desired mode for this experiment is AC Mode Fast Imaging. **B**, Via an optical microscope a view of the AFM cantilever allows to place the cantilever centrally within the scanner head (green cross). **C** Laser alignment onto the tip of the cantilever to maximize the amount of signal reflected towards the detector. **D**, Alignment of the detector such that the maximum of the signal is in the center of the quadrant detector. **E**, Cantilever calibration based on the thermal noise spectrum yields an estimated spring constant of 19.7 N/m. **F**, AC Feedback Mode Wizard to select the drive frequency and the drive amplitude of the AFM cantilever. **G**, Typical imaging settings used for our DNA and nucleosome images. **H**, System status after successful approach of the cantilever towards the surface. **I**, Scanning of the first lines of a 6 μm x 6 μm field of view displaying both image trace (left) and retrace (right).

For FASTSCAN-A cantilevers, a sum signal between 1.3 and 1.5 is typical. Other cantilevers yield different sum signals based on the reflection achieved by the back of the cantilever tip.

7. Align the detector such that the maximum of the signal is in the center of the

quadrant detector using the screws marked by the green arrows in Fig. 4.3D. In case that proper alignment of the laser is not possible, adjust the mirror that reflects the laser signal towards the detector first (red arrow Fig. 4.3D), and then do alignment fine tuning with the screws afterwards.

8. To calibrate the cantilever, select the room temperature and press on *calibrate* (Fig. 4.3E). The calibration uses the thermal noise spectrum<sup>150</sup> of the cantilever and determines the spring constant and the inverse lever sensitivity, which is used to convert the measured cantilever deflection from V to nm. The spring constant should lie within the specifications of the cantilevers used (for FASTSCAN-A cantilevers typically between 17-19 N/m but may vary for different batches).
9. Go to the *Acquire data* tab and scan the cantilever for its resonance frequency in the *AC Feedback Mode Wizard* (Fig. 4.3F). For FASTSCAN-A cantilevers it should be around 1.2-1.4 kHz. Select the driving frequency for the measurement by placing the horizontal dashed line (Fig. 4.3F) slightly left of the peak. Place the horizontal dashed line accordingly to reach a setpoint of 85-90 % at a target amplitude of 12 nm.
10. Start approaching the surface by pressing the *Approach* button (Fig. 4.3G). It is recommended to coarse approach the surface with the head internal Z scanner as it covers a larger Z range and switch to the smaller but faster *Fast HG* scanner before starting to scan (this can be done in the Z Scanner Selection menu). Our typical imaging parameters are shown under Force Control and Scan Control (Fig. 4.3G). After the approach succeeded, the z-position and the Laser Align should be in green color (Fig. 4.3H).
11. Once approached to the surface, verify the resonance peak again in the AC Feedback Mode Wizard window, as the cantilever resonance can change under the influence of a nearby surface.
12. Start imaging (Fig. 4.3I).

*Notes: Choose image size, scan speed, and pixels once and keep the settings constant. In our experience, the best results were obtained at a resolution of 1.46 nm/pixel either scanning 2048 x 2048 pixels in a 3 μm x 3 μm field of view or scanning 4096 x 4096 pixels in a 6 μm x 6 μm field of view. Scanning is then performed at 3 or 1.5 lines per second respectively. The image size represents a compromise between the number of molecules imaged and the imaging time required. The field of view should not be smaller than 3 μm x 3 μm, since it is important to have enough molecules (>100 DNA and nucleosomes) for good statistics in the subsequent analysis. Conversely, when scanning even larger areas (e.g. 12 μm x 12 μm), the time required for recording one image at scanning speeds low enough to enable excellent resolution starts to exceed 1 h, such that cantilever wear and drift become problematic. In addition, very large images are computationally cumbersome to process.*

1. Scanning speed matters! When scanning too fast, the molecules will appear less "sharp" and thus image quality will overall be worse. However, scanning too slowly will increase the effect of drift on the image. The scanning

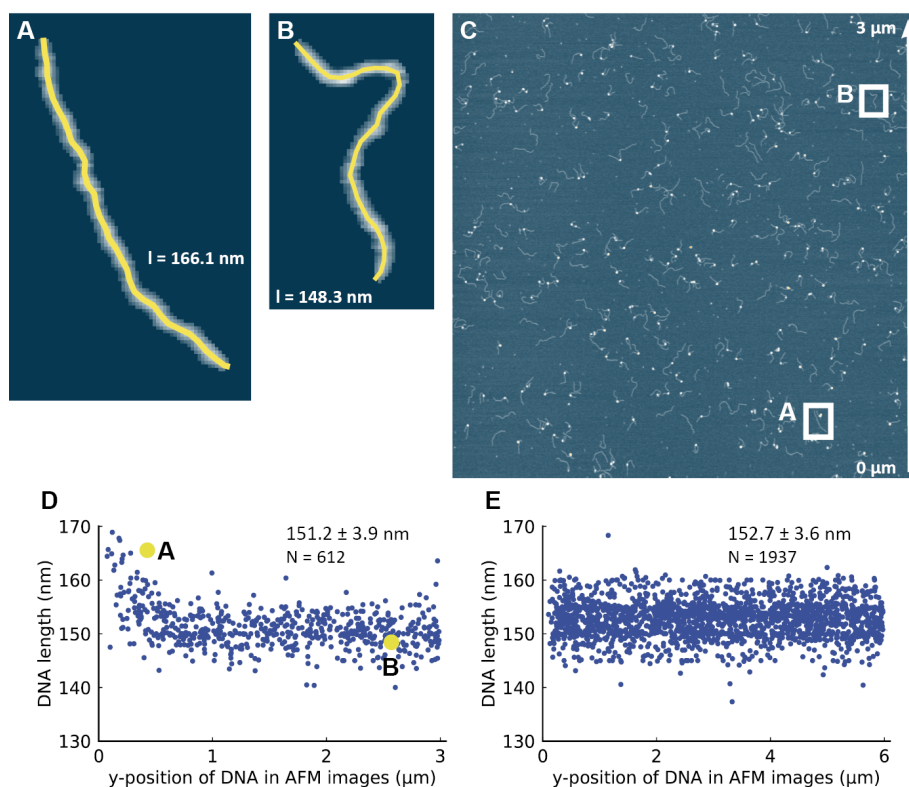


**Figure 4.4:** DNA length as a quality control parameter to detect AFM scanning artifacts. **A**, Example DNA strand at the bottom of an AFM image acquired on a MultiMode 8 AFM system. **B**, Example DNA strand at the top of an AFM image acquired on a MultiMode 8 AFM system. The traced DNA contour is indicated by the yellow line in **A** and **B**. **C**, AFM image with a field of view of  $3\ \mu\text{m} \times 3\ \mu\text{m}$  imaged at  $2048 \times 2048$  pixels acquired on a MultiMode 8 AFM system. The DNA molecules shown in detail in panels **A** and **B** are indicated by the boxes in the image. **D**, Distribution of DNA lengths measured at different y-positions (bottom to top) from a total of 10 AFM images on a MultiMode 8 AFM equipped with a tube scanner. Non-linear effects in the AFM system, likely piezo creep, cause the DNA strands in the bottom of the image to appear to have different lengths than the DNA strands elsewhere in the image. **E**, Distribution of DNA lengths measured at different y-positions (bottom to top) for the JPK Nanowizard Ultraspeed 2. For this instrument, the drift effects due to piezo creep are significantly reduced, likely due to its linearized scanner design.

speed should thus be chosen as high as possible while maintaining the sharp imaging of molecules. For this purpose, we usually measure the diameter of DNA on the surface as it appears in the AFM image. Due to tip convolution, the DNA does not have a visible diameter of 2 nm as expected from its crystal structure. A 6–8 nm DNA apparent full width at half maximum is a good value to target for ongoing AFM imaging making sure that the molecular resolution is high enough for quantitative assessment of the structural parameters. Sometimes, achieving a stable 6–8 nm DNA diameter can be difficult and requires tuning of the imaging parameters (i.e. adapting the drive frequency, the drive amplitude, the setpoint and feedback gain) or exchanging the cantilever.

2. For the large images with hundreds of molecules imaged here, nonlinear behavior and hysteresis of the piezos can cause artifacts and distortions that affect the structural parameters of DNA and nucleosomes. As an example, when imaging  $3\ \mu\text{m} \times 3\ \mu\text{m}$  images on a MultiMode8 AFM (Bruker), DNA molecules appear shorter in the beginning (bottom) of the scan than at the end (top of the image, Fig. 4.4A). This shortening effect is strongest for the first scans, but still occurs at reduced intensity in subsequent scans. In contrast, scanning even larger  $6\ \mu\text{m} \times 6\ \mu\text{m}$  images on the Nanowizard Ultraspeed 2 does not show these nonlinear effects (Fig. 4.4B). Typically, while continuously imaging, these non-linear effects and drift tend to decrease over time once the system stabilizes after warming up.
3. All AFM cantilevers are different, and important properties such as tip radius, resonance frequency, and spring constant can vary significantly between batches. Even cantilevers that are within the specifications of the respective

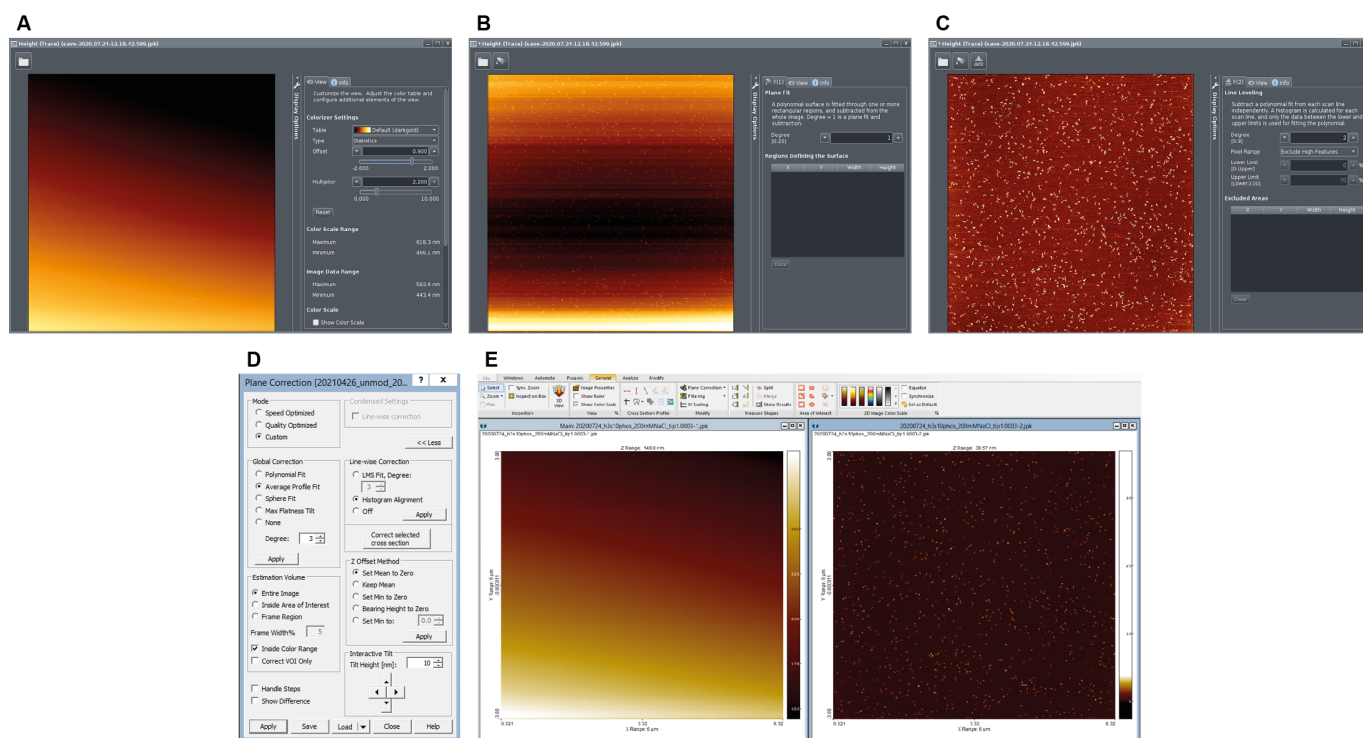


**Figure 4.5:** Plane correction of the raw AFM image. **A**, Raw AFM image displayed in the JPK Data Processing software (version 7.0.128). **B**, AFM image after applying a plane fit of first order. **C**, AFM image after consecutively applying line leveling. **D**, Plane correction parameters best used when plane correcting the raw AFM image using SPIP (Parameters – Mode: Custom, Global Correction: Average Profile Fit, Estimation Volume: Entire Image, Line-wise Correction: Histogram Alignment, Z Offset Method: Set Mean to Zero). **E**, The same raw image as shown in panel A (left) and after applying the plane correction in SPIP (right).

model can show significant variations in obtainable image quality. On the Nanowizard Ultraspeed 2 AFM setup, we had the best imaging results with FASTSCAN-A cantilevers (Bruker). On a MultiMode 8 AFM system that was used in the past, we had the best imaging results using AC160TS cantilevers (Olympus). However, due to the lower resonance frequency of the AC160TS cantilevers compared to FASTSCAN-A cantilevers and due to the smaller maximum image size of the MultiMode 8 ( $2048^2$  pixels), both the scanning speed (1 Hz) and the field of view ( $3\ \mu\text{m} \times 3\ \mu\text{m}$  to keep the pixel size constant) are generally smaller and make the system more prone to drift and limited statistics when analyzing the image. Still, it was possible to take data sets of similar quality – despite the imaging taking longer on the Multi-Mode 8 – on both instruments.

### 4.5.3 AFM image analysis

*Note: We have developed an analysis pipeline written in Python to analyze the AFM images, which has been described in detail previously.<sup>112</sup> A detailed guide on how to set up the Python analysis pipeline can be found on the [Github repository](#). Therefore, the image analysis pipeline is described only briefly here and the focus will lie on tips and tricks on how to test image quality from the structural parameters obtained from the image readout. In addition, we discuss possible further analyses to obtain additional parameters such as DNA persistence length and states of nucleosome wrapping.*

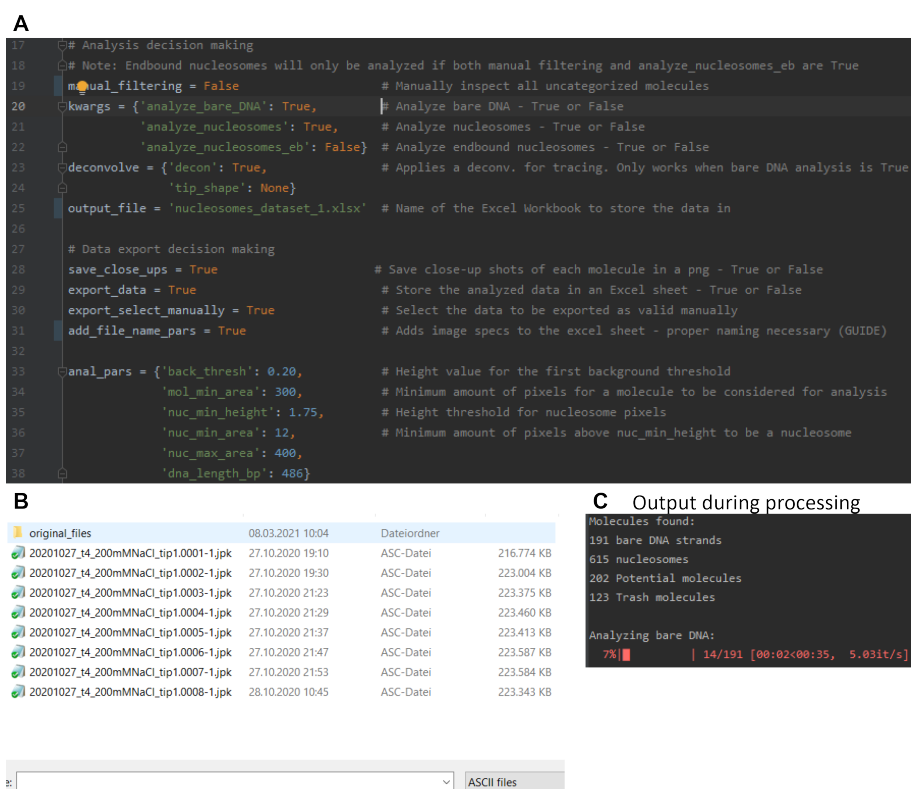


**Figure 4.6:** Image analysis post-processing software. **A**, Example input parameter settings for automated readout of the AFM images. **B**, File dialogue to select the desired AFM image for automated readout. **C**, Output of the analysis software during processing. The number of molecules detected in one example AFM image.

1. To preprocess the raw AFM images, apply either a plane fit or an average profile fit to the surface and subsequently apply a line-wise leveling to remove observable steps between subsequent scan lines due to noise in the scanner system. The plane correction can be performed using either the image analysis software supplied by the AFM manufacturer (JPK Data Processing from JPK in our case, Fig. 4.5 A-C) or using the commercially available software SPIP (Image Metrology, Fig. 4.5 D-E). Save the leveled AFM image as ASCII file for further processing.
2. Open the custom Python code as described in the installation guide<sup>112</sup> and select the desired analysis parameters. See Fig. 4.6A for example analysis parameters used for analyzing the DNA and nucleosomes in our images. Depending on the background noise level, parameter tuning might be needed to maximize molecule detection. If the value of the background threshold is chosen too small, the molecules cannot be separated properly from the background and if the value is chosen too high, the molecules might become fractured. Still, thresholding does not affect the final nucleosome parameters such as volume, opening angle, or height.
3. Run the code and select the image you want to analyze from the file dialogue (Fig. 4.6B). DNA and nucleosomes are then detected and their structural parameters are analyzed automatically (Fig. 4.6C). The results are saved to an Excel worksheet. As described in the user manual, you can also choose to manually help categorizing molecules that cannot be categorized automatically (such as two slightly overlapping DNA strands) by setting the manual filtering parameter (Fig. 4.6 A) to True.

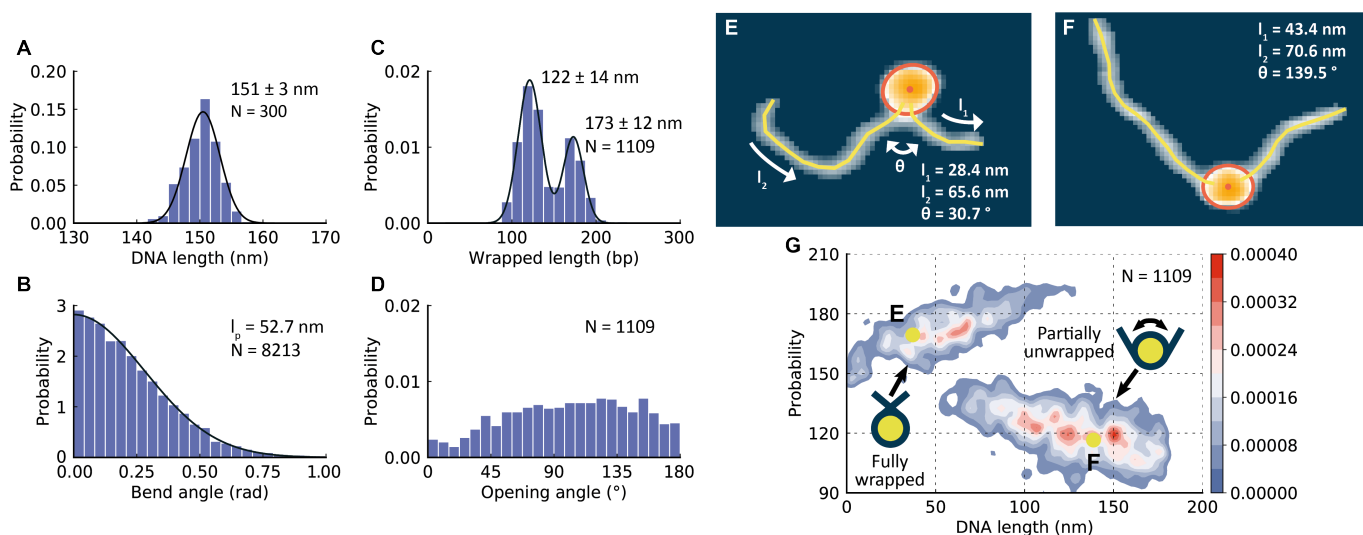


**Figure 4.7: Example analysis of DNA and nucleosome conformations for a dataset obtained with the protocol presented here.** A, Distribution of bare DNA lengths. The solid line is a Gaussian fit centered at  $151 \pm 3$  nm (mean  $\pm$  STD). B, The DNA length is determined by tracing its contour with segments of 5 nm length and the relative orientation of consecutive segments yields DNA bend angles. The solid line is a fit with a folded Gaussian as described previously<sup>151</sup> to obtain the DNA persistence length ( $l_p = 52.7$  nm). C, Distribution of DNA length wrapped around nucleosomes. The solid line is a double Gaussian fit to the data. The peaks are centered at  $120 \pm 14$  bp and  $168 \pm 12$  bp (mean  $\pm$  STD). D, Distribution of nucleosome opening angles. E, Example image and tracing of a fully wrapped nucleosome. F, Example of an analyzed partially unwrapped nucleosome. G, 2D kernel density profile (bandwidth = 2.5, 2.5 bp) of nucleosome opening angles and wrapped lengths. The cartoons in the insets depict the qualitative shape of fully and partially wrapped nucleosomes.

4. Repeat the image analysis for all images of the data set in order to have all DNA and nucleosomes of the imaging run analyzed.
5. The structural parameters stored in the Excel worksheet can be used to gain a broad understanding of the DNA and nucleosomes in the images and serve as an input for further analysis, for example by principle component analyses or clustering. For an example data set of wildtype nucleosomes reconstituted on a DNA segment of 486 bp possible further analysis and plots are shown in Fig. 4.7 A-E.

*Notes:*

1. We typically deposit both bare DNA and nucleosomes on each surface for imaging, since the average length of the bare DNA is used to estimate the amount of wrapped DNA of a nucleosome by subtracting the length of the two arms from the average bare DNA length. Using the DNA length determined from co-deposited molecules is more accurate than using an average DNA length from separate imaging runs since even if the tip geometry does not change while measuring, the bare DNA length might differ slightly between images due to changes in drift.
2. Looking at the average values of structural parameters such as the average length of bare DNA and the average nucleosome volume provides insights about the change in data quality for a specific dataset. As a rule of thumb, for a well-imaged high-quality dataset, the average bare DNA length should not differ by more than 2 nm over multiple images. Similarly, constant average

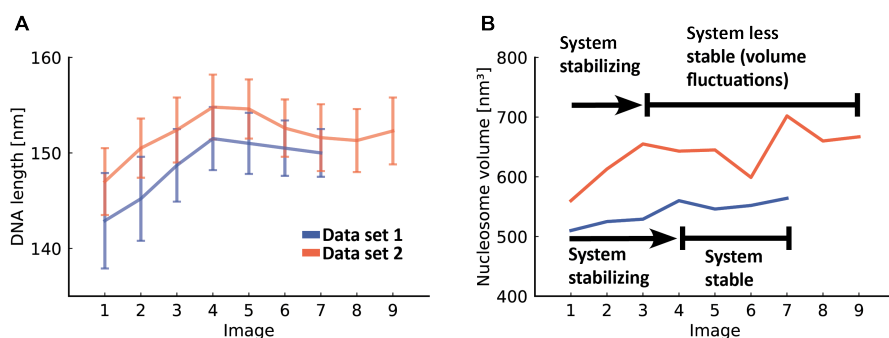


**Figure 4.8:** DNA length and nucleosome volume as quality control parameters for AFM imaging. **A**, Average DNA length in subsequent images (mean and standard deviation over 200 DNA strands per image). **B**, Average nucleosome volumes in subsequent images (mean over ~400 nucleosomes per image). Shown are two data sets obtained on a Nanowizard Ultraspeed 2, each comprising multiple 6 x 6  $\mu\text{m}^2$  images. All images in one data set were obtained using the same AFM tip. Data set 1 consists of 7 AFM images and data set 2 consists of 9 AFM images that were analyzed with respect to DNA and nucleosome structural parameters such as DNA length and nucleosome volume. For data set 1, the system stabilized during the first three images as indicated by almost constant DNA lengths and nucleosome volumes after image 3. In contrast, in data set 2, the volume parameter still shows fluctuations after several hours of imaging (~45 min per image) indicating that the system is less stable. Overall, in data set 2 the DNA lengths and the volumes are larger than for data set 1, indicating that the AFM cantilever has a less sharp tip.

nucleosome volume (exhibiting not more than 5-10 % difference for images of the same dataset) is a good measure for image quality and an increase or, in general, variation of nucleosome volume during a measurement run indicates changes in the tip geometry and will affect the structural parameters in general (Fig. 4.8).

3. A detailed description of how to extract 5 bp unwrapping populations from the data obtained using this protocol can be found in our previous publication.<sup>112</sup>
4. Typically, datasets of ~1000 nucleosomes or more are required to allow for a detailed analysis of the unwrapping landscape.
5. Additional parameters that are stored in the output Excel sheet such as radius of gyration, end-to-end distance or length of the individual nucleosome arms allow for many different analyses. As an example, the 2D distribution of arm lengths and opening angles can be used to test for anti-cooperative unwrapping or the ratio of arm lengths can be used to assess nucleosome positioning along the DNA strand.

## 4.6 Notes

1. While this protocol was developed for imaging and analysis of DNA and nucleosomes, it can be readily adapted to other nucleo-protein complexes.
2. Short chained poly-L-lysine should be used to guarantee a monolayer on the surface.
3. Our surface deposition and imaging protocol is compatible with a broad range of ionic conditions. For example, we obtained high-quality images using 10 mM NaCl, 200 mM NaCl or 2 mM  $\text{MgCl}_2$  (always with 10 mM TRIS, pH 7.6). Importantly, ionic conditions significantly affect DNA and nucleosome geometry.<sup>64;92;112</sup>

## Acknowledgements

We thank Philipp Korber and Felix Müller-Planitz for help with initial nucleosome reconstitutions, Pauline Kolbeck, Tine Brouns, Wout Frederickx, Herlinde De Keersmaecker, Steven De Feyter, and Björn H. Menze for discussions and assistance with AFM imaging, and Thomas Nicolaus for help with sample preparation. This work

was funded by the Deutsche Forschungsgemeinschaft (DFG, German Research Foundation) through SFB863 – Project ID 111166240.

### **Competing interests**

The authors declare no conflict of interest

# 5

## High-throughput AFM analysis reveals unwrapping pathways of H3 and CENP-A nucleosomes

Nucleosomes, the fundamental units of chromatin, regulate readout and expression of eukaryotic genomes. Single-molecule experiments have revealed force-induced nucleosome accessibility, but a high-resolution unwrapping landscape in the absence of external forces is currently lacking. Here, we introduce a high-throughput pipeline for the analysis of nucleosome conformations based on atomic force microscopy and automated, multi-parameter image analysis. Our data set of ~10 000 nucleosomes reveals multiple unwrapping states corresponding to steps of 5 bp DNA. For canonical H3 nucleosomes, we observe that dissociation from one side impedes unwrapping from the other side, but in contrast to force-induced unwrapping, we find only a weak sequence-dependent asymmetry. Notably, centromeric CENP-A nucleosomes do not unwrap anti-cooperatively, in stark contrast to H3 nucleosomes. Finally, our results reconcile previous conflicting findings about the differences in height between H3 and CENP-A nucleosomes. We expect our approach to enable critical insights into epigenetic regulation of nucleosome structure and stability and to facilitate future high-throughput AFM studies that involve heterogeneous nucleoprotein complexes.<sup>1</sup>

### 5.1 Introduction

Nucleosomes are fundamental to the compaction of eukaryotic genomes into chromatin and function as regulators of gene activity.<sup>55;152;153</sup> While a large number of static nucleosome structures has become available in the past two decades,<sup>60;90</sup> the

---

<sup>1</sup>This chapter was reproduced from *Konrad et al.*<sup>112</sup>, with permission from the Royal Society of Chemistry. Author contributions: S.F.K., W.V. and J.L. designed the experiments. S.F.K. performed biochemical experiments and W.F., T.B. and S.D.F. supported AFM measurements. B.M. assisted with data analysis. S.F.K., W.V. and J.L. wrote the paper with input from all authors

dynamic nature of nucleosomes<sup>154</sup> and the role of epigenetic modifications<sup>15</sup> remain unclear. Since dynamic structural changes influence the accessibility of nucleosomal DNA for readout<sup>155</sup> and processing,<sup>156;157</sup> it is critical to understand nucleosomal unwrapping. In the cell, unwrapping of DNA from nucleosomes can be achieved either by active processes involving e.g. RNA polymerase or nucleosome chaperones that exert forces and torques on the nucleosomes,<sup>139;141</sup> or spontaneously by thermal fluctuations.<sup>142</sup> Using single-molecule micromanipulation techniques such as optical tweezers, the energetics of force-induced nucleosome unwrapping have been probed at high resolution.<sup>66;69;144</sup> In contrast, the unwrapping landscapes in the absence of force have thus far been less explored due to a lack of suitable techniques. Nevertheless, such spontaneous access to nucleosomal DNA sequences is fundamental for the binding of proteins involved in gene regulation, recombination, and repair.<sup>67;142;158</sup>

Canonical nucleosome core particles consist of two copies each of the four histones H2A, H2B, H3 and H4 assembled into a histone octamer that is tightly wrapped by 147 bp of DNA.<sup>52;138</sup> The central 121 bp of DNA contact structurally conserved histone-fold domains and the remaining 13 bp of DNA at each end bind to the N-terminal alpha-helix4 ( $\alpha$ N) of histone H3. Electrostatic interactions and hydrogen bonds stably pack the DNA onto the histone octamer, while DNA breathing, sliding, gaping, tightening, and loosening allow for nucleosomal dynamics on millisecond to minute time scales.<sup>16;82;85;159</sup> Partial unwrapping of the nucleosome core particle has been shown to occur anti-cooperatively<sup>16</sup> with unwrapping on one end stabilizing the wrapped DNA on the opposite end in canonical nucleosomes.<sup>68</sup>

Numerous histone variants and post-translational modifications yield nucleosomal structures with varying degrees of stability and DNA wrapping.<sup>15;153;160</sup> In centromeres – the chromosomal domains where both chromatids come together – H3 is replaced by the histone variant CENP-A, which has 64% sequence identity<sup>161–163</sup> with H3. Crystallographic studies<sup>137</sup> have revealed that in CENP-A nucleosomes reconstituted with human  $\alpha$ -satellite DNA, the 13 bp of DNA at each end are more flexible than in H3 nucleosomes due to one missing helical turn of  $\alpha$ N.

Atomic force microscopy (AFM) is a powerful tool to probe nucleosome structure and interactions due to its capability to image molecular complexes at the single molecule level label-free and with sub-nanometer resolution, well suited to visualize the DNA and protein components of nucleosomes.<sup>28;82;83;104;107;140</sup> Nevertheless, the accuracy and precision of measurements of structural parameters by AFM suffer from convolution of the molecular and AFM tip geometry, from the typically small sample sizes, and from inconsistencies associated with manual data analysis.

Here, we present an automated analysis pipeline for DNA and DNA–protein complexes in AFM topographic images that makes possible rapid and highly quantitative assessment of thousands of molecules with single-molecule resolution. Using the capabilities of our multi-parameter analysis, we reveal distinct unwrapping states of canonical H3 and CENP-A nucleosomes. We observe unwrapping of the two DNA ends to be anti-cooperative in H3 nucleosomes, consistent with previous reports. In contrast, no anti-cooperative unwrapping was found for CENP-A nucleosomes. Our results reconcile previous conflicting results on the height of CENP-A nucleosomes and reveal an important role of DNA crossovers in modu-

lating the energy landscape of nucleosome wrapping.

## 5.2 Results

### 5.2.1 Automated AFM image analysis to quantify nucleosome conformations

We assembled nucleosomes by salt gradient dialysis on 486 bp DNA constructs under sub-stoichiometric conditions, such that the final sample contains bare DNA and predominantly mono-nucleosomes. Our DNA construct comprises a W601 nucleosome positioning sequence<sup>70</sup> (147 bp) flanked by a short DNA arm (106 bp) and a long arm (233 bp) (Fig. 5.1a) and was used for both H3 and CENP-A nucleosomes (Methods).

We deposited samples from aqueous buffer on poly-L-lysine coated mica prior to rinsing and drying of the sample.<sup>148;164</sup> High-resolution images of the deposited nucleosome samples were obtained by amplitude modulation AFM in air (Fig. 5.1b). We developed an automated AFM image analysis pipeline to extract structural information of thousands of DNA and nucleosomes (Fig. 5.1c) by multi-parameter analysis. Molecule detection consists of a background subtraction after applying a Gaussian filter and a subsequent skeletonization<sup>165</sup> of both bare DNA (Fig. 5.1d) and nucleosomes (Fig. 5.1e). The skeletonized backbone of the molecules serves as the basis for classification: whereas the skeleton of bare DNA has exactly two endpoints and no branchpoints – points that have more than two neighbors – the skeleton of nucleosomes contains exactly two endpoints and two branchpoints. An adapted version of a previously published algorithm to trace DNA in AFM images<sup>109</sup> is used to measure the length of bare DNA molecules and nucleosome arms. Volume and height of the nucleosome core particles are estimated by fitting half ellipsoids to the measured height data (Fig. 5.1e). The vectors connecting the DNA arm-ellipsoid intersections and the center of the ellipsoid define the nucleosome opening angle (Fig. 5.1e).

Our fully automated image analysis pipeline achieved a detection rate of ~95% (Fig. 5.9), reducing the fraction of undetected molecules at least four-fold compared to the most advanced previous automated analysis framework for DNA–protein complexes.<sup>94</sup> Importantly, the automated analysis makes possible high-throughput analysis of the large data sets generated by state-of-the-art AFM instruments imaging large fields of view by operating at high scan speeds: for example, imaging and automated tracing of a  $12\ \mu\text{m} \times 12\ \mu\text{m}$  field of view yielded structural parameters for 1250 bare DNA strands and 1345 nucleosomes (Methods and Fig. 5.1c).

### 5.2.2 Identifying wrapping intermediates by multi-parameter analysis

To quantify nucleosome wrapping, we first evaluated the average contour length of bare DNA molecules and found  $l_c = 152.9 \pm 6.3$  nm (mean  $\pm$  std from 5651 molecules, Fig. 5.9) corresponding to a length per bp of  $0.314 \pm 0.013$  nm, in excellent agreement with previous measurements by AFM<sup>147;166</sup> and solution X-ray scattering.<sup>167</sup> Similarly, we analyzed the DNA arm lengths of nucleosomes. By subtracting the combined nucleosome arm lengths from the mean contour length of bare DNA molecules, we obtain the wrapped length, *i.e.* the length of DNA con-

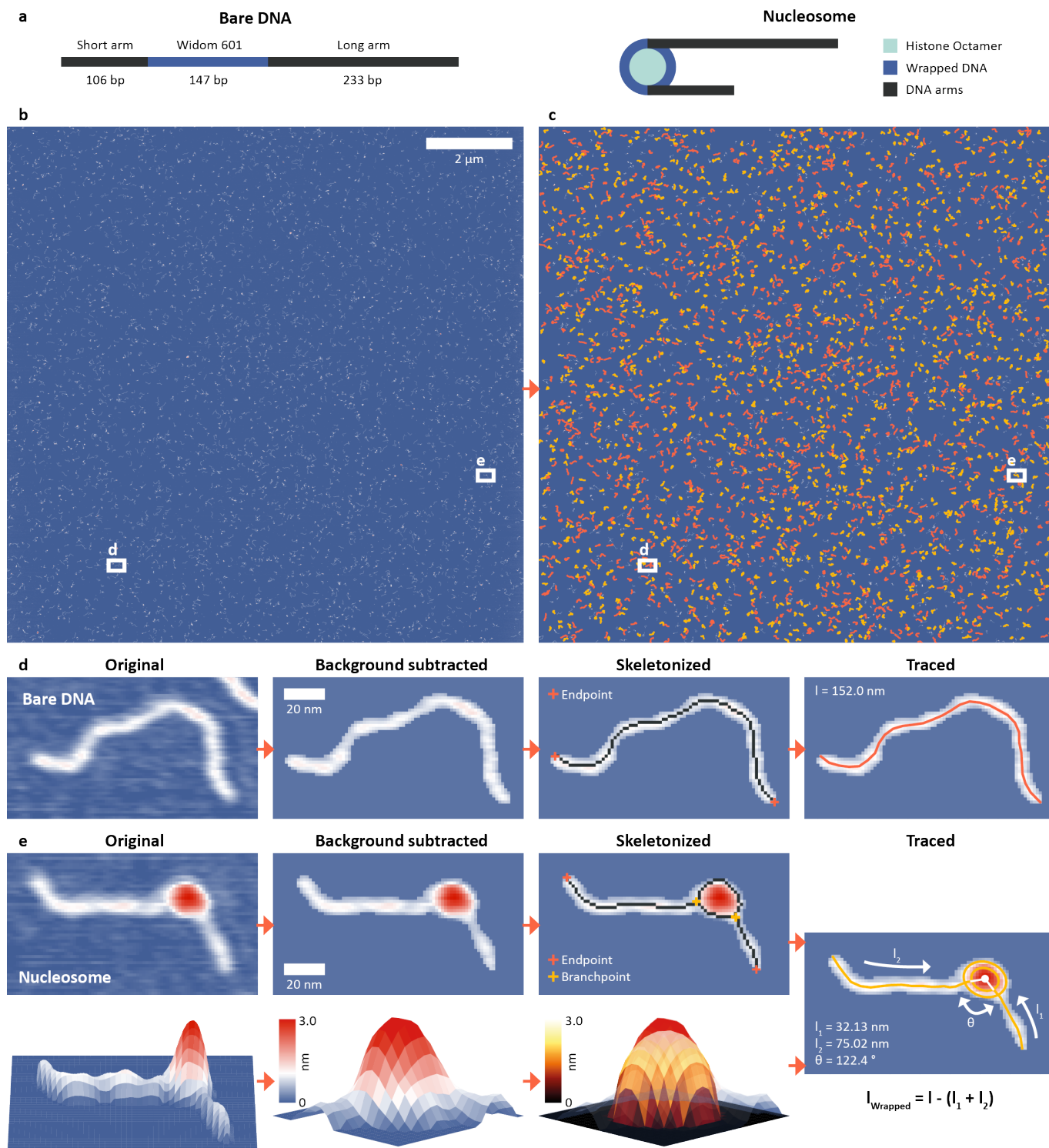


**Figure 5.1: DNA and nucleosome structure parameters by automated AFM image analysis.** a, Scheme of the DNA construct used throughout this work with a total length of 486 bp (106 bp + 147 bp Widom601 sequence + 233 bp) and the histone octamer (two copies each of H2A, H2B, H3 or CENP-A and H4). b, AFM image with a field of view of  $12\ \mu\text{m} \times 12\ \mu\text{m}$  with  $8192^2$  pixels corresponding to a resolution of 1.46 nm per pixel. c, AFM image after tracing 1250 bare DNA strands (orange) and 1345 nucleosomes (yellow) with our automated image analysis pipeline. d, Image of a selected bare DNA strand: raw data, after background subtraction, after skeletonization, and after tracing. e, Image of a selected nucleosome: raw data, after background subtraction, and after skeletonization, together with a 3D surface plot of the nucleosome and the half ellipsoid fitted to the height profile of the core particle resulting in the traced nucleosome.

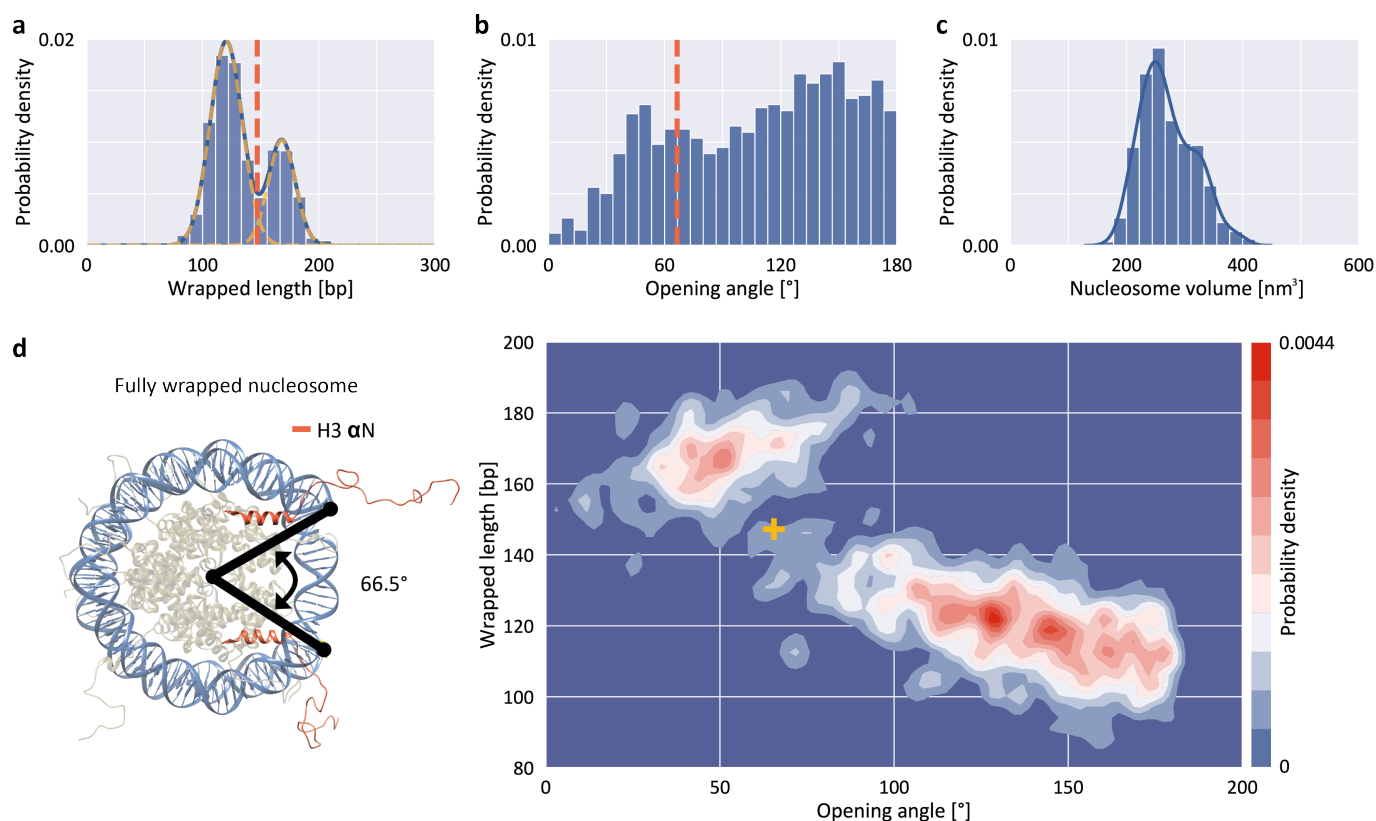


**Figure 5.2: Structure parameters for H3 nucleosomes from AFM imaging.** **a**, Wrapped DNA length distribution fitted using the sum of two Gaussians (centered at  $120 \pm 14$  bp and  $168 \pm 12$  bp). **b**, DNA opening angle distribution. The dashed orange line indicates the expected position of a fully wrapped nucleosome. **c**, Nucleosome core particle volume distribution. The solid line is a kernel density estimate. **d**, 2D kernel density profile (bandwidth =  $2.5^\circ$ , 2.5 bp) of nucleosome opening angle and wrapped length. The expected position of fully wrapped nucleosomes based on the crystal structure (left; rendered from PDB 1KX5) is shown as a yellow cross at an opening angle of  $66.5^\circ$  and a wrapped DNA length of 147 bp. The data set shown includes  $N = 1011$  nucleosomes.

fined in the nucleosome core particle. For a representative data set of H3 nucleosomes in buffer with 200 mM NaCl, we obtain a wrapped length of  $135 \pm 27$  bp (mean  $\pm$  std from 1011 molecules), in good agreement with previously reported values.<sup>94</sup> However, in contrast to previous reports<sup>91;94;106</sup> we observed a bimodal distribution – rather than a single peak – for the wrapping of H3 nucleosomes (Fig. 5.2a). Fitting the wrapped length distribution to the sum of two Gaussians yields populations centered at  $120 \pm 14$  bp and at  $168 \pm 12$  bp. The distributions of opening angles (Fig. 5.2b) and of nucleosome core particle volumes (Fig. 5.2c) similarly suggest at least two different populations. However, the opening angle distribution is relatively flat, indicating that a large range of opening angles is sampled. The distribution of nucleosome heights shows only a single peak (Fig. 5.3a). To obtain a full quantitative view of nucleosome conformations, we exploit the fact that our analysis pipeline measures multiple parameters, namely short arm length, long arm length, opening angle, particle volume and particle height, for each nucleosome to go beyond 1D distributions. Because of the solenoidal winding of nucleosomal DNA, we expect wrapped length and opening angle to be correlated and we indeed find that nucleosomes at wrapped lengths below 150 bp show a negative correlation between opening angle and wrapped length (Fig. 5.2d), suggesting that these nucleosomes populate states of partial unwrapping. The remaining nucleosomes

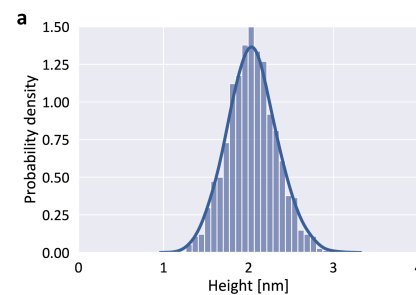


**Figure 5.3: Nucleosome heights.** **a**, Raw nucleosome heights of the H3 nucleosome data set shown in Figure 5.2 ( $N = 1011$ ).

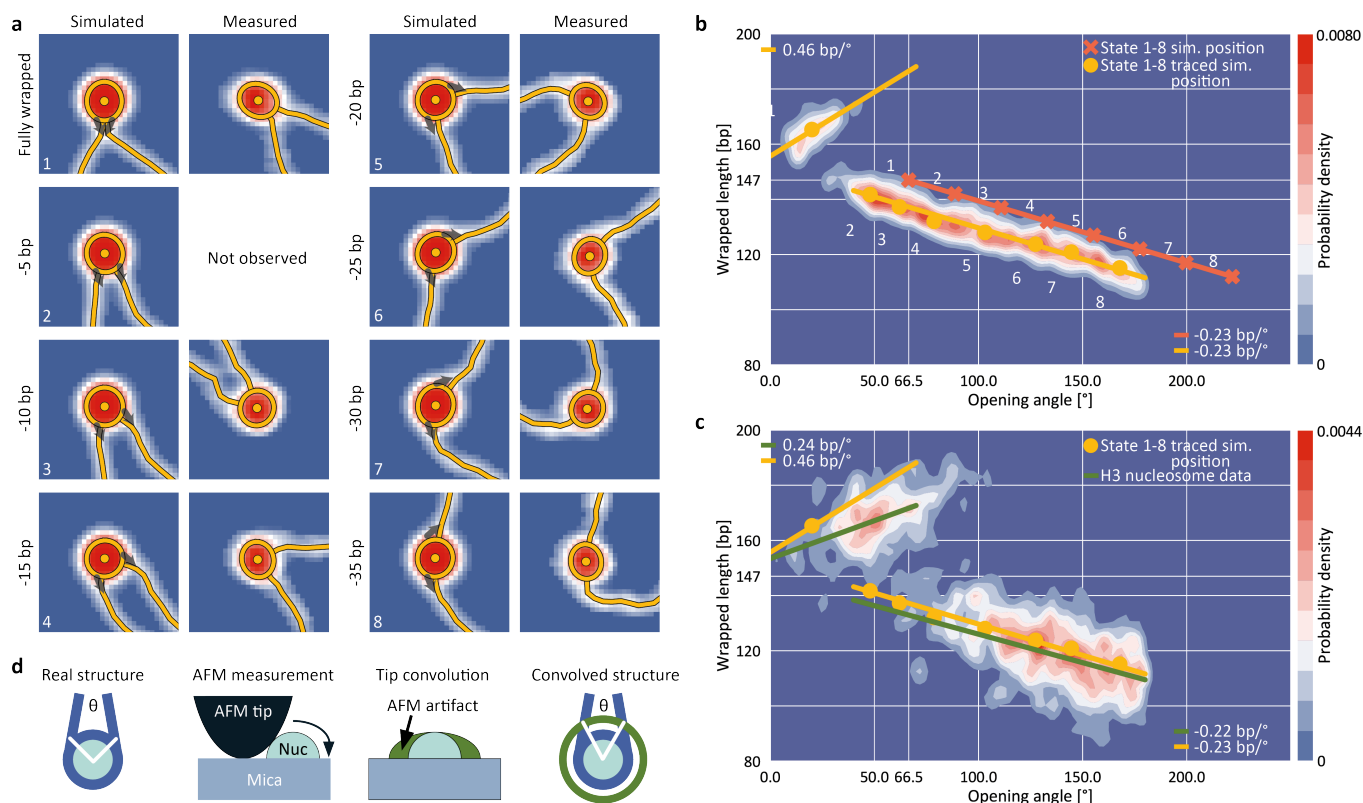


**Figure 5.4: Assigning nucleosome wrapping states by comparison between simulation and experiment.** **a**, Example synthetic nucleosome images of the eight simulated states and AFM imaged and traced nucleosomes with the same opening angle. The grey arrows indicate the starting direction of DNA simulation (Fig. 5.10). For state 2, no measured counterpart was observed. **b**, 2D kernel density profile (bandwidth = 2.5°, 2.5 bp) of opening angle and wrapped DNA length for simulated nucleosome images (N = 1040, Fig. 5.10). The simulations consist of eight states of nucleosome wrapping that differ by 5 bp of unwrapping. Orange crosses indicate the simulated positions based on the 5 bp unwrapping periodicity. Yellow circles indicate the centroids of each state found after analyzing the simulated images with our automated analysis pipeline. On average, the opening angle is shifted  $\sim 50^\circ$  (MSE =  $20^\circ$ ) to lower angles due to the effect of AFM tip convolution. **c**, 2D kernel density profile (bandwidth = 2.5°, 2.5 bp) of opening angle and wrapped DNA length for AFM imaged nucleosomes (N = 1011). Regression lines fit to the experimental data (green) in comparison to the expected correlations (yellow) based on the simulations from (b). The top left population consists of fully wrapped nucleosomes in which the protruding DNA arms overlap in front of the nucleosome core particle whereas the lower population consists of nucleosomes in different states of DNA unwrapping. **d**, Sketch of AFM tip convolution resulting in an underestimation of the opening angle.

at apparent wrapped lengths between 160 bp and 190 bp (Fig. 5.2d) exceed the expected wrapping of the canonical nucleosome by  $\sim 20$  bp.

To quantitatively understand the observed 2D distributions, we simulated AFM images of nucleosomes with different levels of unwrapping. Simulated datasets were generated for eight states of unwrapping between 0 bp (fully wrapped; state 1) and 35 bp (state 8), with 5 bp wrapped length differences (Fig. 5.4a, Fig. 5.10, and Methods), in line with the periodicity of the DNA helix, with results from single molecule DNA force spectroscopy experiments,<sup>168;169</sup> and with cryo-EM observations of nucleosome wrapping states.<sup>68</sup> After generating the ensemble of simulated nucleosome conformations, we applied AFM tip convolution and added experimental noise to create synthetic images that subsequently were analyzed using our automated framework (Fig. 5.4b). The slope of wrapped length vs. opening angle for measured nucleosomes at wrapped lengths below 150 bp (Fig. 5.4c,  $-0.22$  bp/°) agrees well with the slope predicted from simulated data (Fig. 5.4b,  $-0.23$  bp/°), in-

dicating that nucleosomes attach to the surface in a flat geometry with the DNA gyres parallel to the surface. However, we find that the analysis of the synthetic images systematically underestimates the opening angle by  $\sim 50^\circ$  (mean squared error MSE =  $20^\circ$ ) compared to the input configurations. This underestimation is the result of tip convolution in AFM imaging: due to the finite size of the AFM tip, the dimension of molecules is overestimated obscuring the exact entry/exit position of DNA in nucleosomes (Fig. 5.4d).

For the simulated partially unwrapped conformations (Fig. 5.4b, states 2–8; 5–35 unwrapped bp), the wrapped lengths determined from tracing of simulated images agree well with the input configurations (MSE = 4.2 bp). In contrast, the measured wrapped length for the simulated fully wrapped nucleosomes (state 1) exceeds the actual wrapped length of 147 bp by  $\sim 18$  bp. Importantly, the apparent wrapped length of 165 bp is in striking agreement with the measured wrapped length of the second peak of the H3 nucleosome data ( $168 \pm 12$  bp; Fig. 5.2a, d and 5.4c). Thus, our simulations rationalize why the apparent wrapped lengths for fully wrapped nucleosomes exceed the 147 bp expected from the crystal structure: the DNA arms that leave the nucleosome entry/exit site overlap close to the nucleosome core particle due to their initial directionality and the bending stiffness of DNA (Fig. 5.4a). AFM tip convolution obscures the crossing DNA strands and the software routine interprets the DNA crossover as being part of the nucleosome core, which in turn results in the apparent wrapped length values  $>160$  bp. The results from simulated nucleosome structures strongly suggest that the population at  $\sim 165$  bp wrapped length corresponds to fully wrapped nucleosomes (Fig. 5.4c, top left population), with the DNA arms crossing close to the nucleosome core particle.

### 5.2.3 Opposing effects of salt concentration on nucleosome wrapping

While DNA is highly negatively charged, histone octamers carry significant net positive charge. Thus, histone–DNA interactions are sensitively modulated by ionic screening.<sup>64,92</sup> Additionally, crossing of the DNA arms exiting the nucleosome core particle presents an energy barrier that shapes the wrapping landscape.<sup>93</sup> To investigate how ionic screening and DNA crossing at the nucleosome dyad affect nucleosome wrapping, we measured H3 nucleosomes deposited from buffer solutions of different ionic strengths ( $[\text{NaCl}] = 10$  mM, 50 mM, and 200 mM, Fig. 5.5a). Within this range of ionic strengths the DNA contour length, DNA bend angle distribution and nucleosome adsorption geometry are unaffected (Fig. 5.11). To quantify the wrapping landscape of H3 nucleosomes as a function of ionic strengths, we first performed a principal component analysis (PCA) of nucleosome volumes and wrapped DNA lengths (Fig. 5.5a, insets) to separate fully (white datapoints) and partially (black data points) wrapped nucleosomes. We find that the population of the fully wrapped state (31.2%, 24.4% and 13.8% at 200 mM, 50 mM, and 10 mM NaCl, respectively; determined from the thresholds indicated in the insets of Fig. 5.5a) decreases with decreasing ionic strength, in line with increased like-charge repulsion of DNA at the exit/entry region at lower salt concentrations and consistent with observations for end-loops in supercoiled plasmids.<sup>170</sup>

Strikingly, we find that nucleosomes measured at an ionic strength of 50 mM NaCl and 2 mM  $\text{MgCl}_2$  populate the fully wrapped state with a probability of 58% (Fig. 5.6), much more frequently than nucleosomes measured in the monovalent

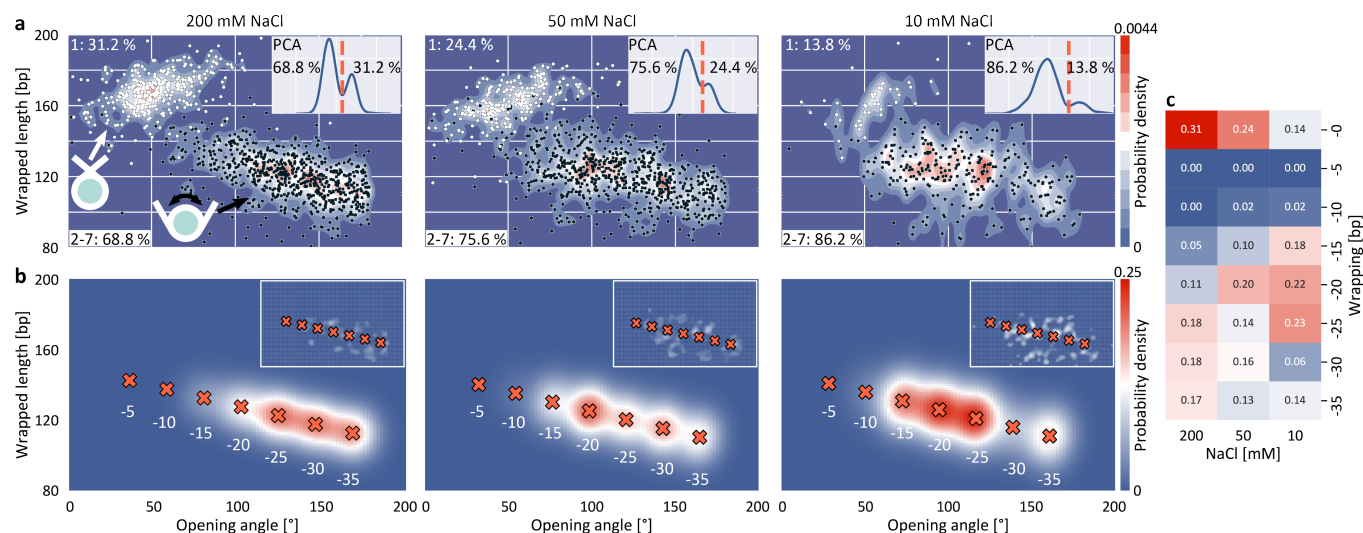


**Figure 5.5: Effect of salt concentration on H3 nucleosome wrapping.** **a**, 2D kernel density estimate profiles of wrapped length versus opening angle. Black and white dots indicate individual nucleosomes. The PCA of wrapped length and volume yields the basis for separating the two major populations as shown in the inset. The data sets include  $N = 1011$  nucleosomes for 200 mM NaCl,  $N = 934$  at 50 mM NaCl, and  $N = 325$  at 10 mM NaCl. **b**, 2D Gaussian fits to the partially unwrapped nucleosomes. The Gaussian amplitudes yield the populations of the individual states of unwrapping and the insets show the fit residuals. 2D Gaussian fits to the partially unwrapped nucleosomes at 50 mM NaCl and 10 mM NaCl show the trend towards more compact wrapping for lower salt concentrations. All nucleosomes presented in this plot are from the same nucleosome reconstitution and were imaged with the same cantilever. **c**, Heat map of the populations of the individual wrapping states for NaCl concentrations of 200 mM, 50 mM and 10 mM.

salt conditions. The significant decrease in unwrapping upon adding  $Mg^{2+}$  is in line with previous work on the effect of salt concentration on nucleosome wrapping<sup>91;93</sup> and with the preferential association of  $Mg^{2+}$  ions with nucleosomes observed by ion counting.<sup>64</sup>

To quantify how changing the ionic strength affects the distribution of the partially unwrapped states, we fitted seven 2D Gaussians located at fixed distances corresponding to the 5 bp periodicity and corrected for tip convolution based on the simulations. The amplitudes of the Gaussians represent the occupancies of the individual states of unwrapping and demonstrate a clear trend towards increased wrapping at reduced ionic strength, in line with increasing opposite-charge attraction that governs histone–DNA interactions and with previous work using FRET.<sup>171;172</sup> To test the influence of electrostatic interactions with the surface on nucleosome conformations,<sup>173</sup> we performed control measurements varying the poly-L-lysine concentration used for surface preparation tenfold and found no significant differences (Fig. 5.12).

#### 5.2.4 Histone H3 nucleosomes unwrap anti-cooperatively

Building on the ability to precisely quantify nucleosome wrapping, we next investigated the cooperativity in unwrapping behavior of H3 nucleosomes. The two sides of DNA exiting the nucleosome are distinguishable in our assay since the W601 sequence is placed asymmetrically, giving rise to a longer and a shorter DNA arm (Fig. 5.1a). The 2D distribution of short nucleosome arm length versus opening angle reveals a population at opening angles  $<80^\circ$  and a bimodal distribution of short arm lengths for opening angles  $>80^\circ$  (Fig. 5.7a). The population at opening an-

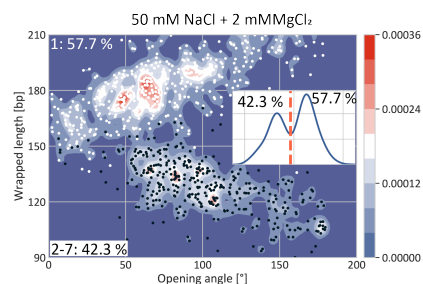


**Figure 5.6: Nucleosomes deposited from magnesium buffer.** 2D kernel density estimate profile of wrapped length versus opening angle measured at a salt concentration of 50 mM NaCl and 2 mM  $MgCl_2$ . The data set contains  $N = 870$  nucleosomes.

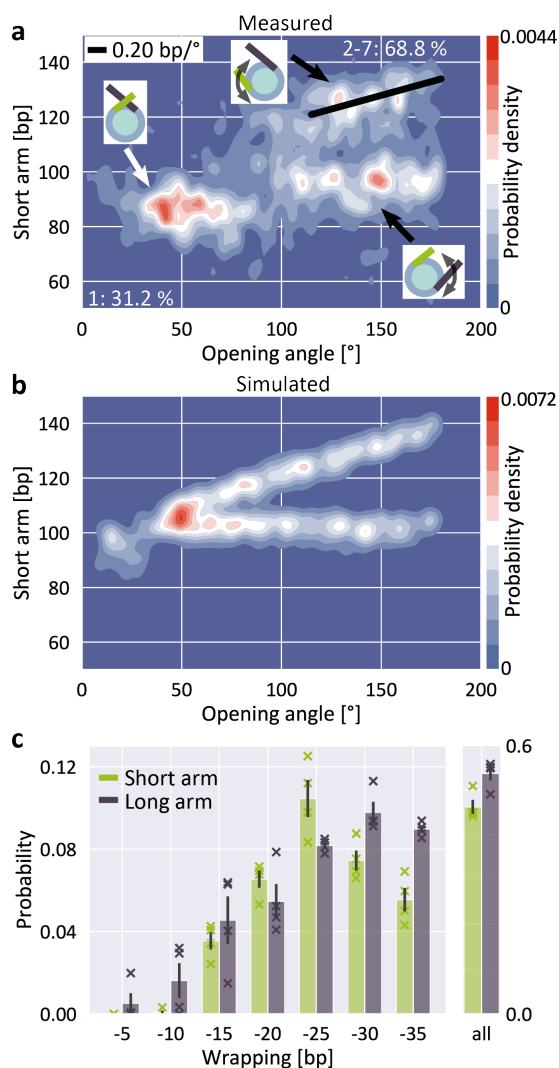


**Figure 5.7: Anti-cooperative unwrapping of H3 nucleosomes.** **a**, 2D kernel density profile (bandwidth = 2.5°, 2.5 bp) of short arm length and opening angle for H3 nucleosomes at 200 mM NaCl. A bimodal distribution for opening angles  $>80^\circ$  is apparent, consistent with anti-cooperative unwrapping of the nucleosome core particle ( $N = 1011$ ). **b**, 2D kernel density profile (bandwidth = 2.5°, 2.5 bp) of short arm length and opening angle for simulated nucleosomes ( $N = 1950$ ). Unwrapping was simulated to occur either exclusively at the short arm or exclusively at the long arm, leading to a bimodal unwrapping behavior. **c**, 2D Gaussian fits to the density distribution of partially unwrapped nucleosomes (Fig. 5.13) yield the populations of individual states of unwrapping. Unwrapping occurs significantly more likely (two-sample t-test  $p = 0.015$ ) via the long arm ( $53.7 \pm 1.6\%$ ) than via the short arm ( $46.3 \pm 1.6\%$ ; mean  $\pm$  SEM from four independent repeats) of the nucleosomes respectively. Data sets ( $N = 1011, 1524, 1480$  and  $815$ ) comprise nucleosomes reconstituted in three independent nucleosome reconstitutions and imaged on two different AFM setups. Crosses indicate values from the individual data sets.

gles  $<80^\circ$  features short arm lengths of 75–95 bp, *i.e.*  $\sim 20$  bp shorter than expected from the design of our DNA construct (106 bp), but consistent with the apparent length reduction due to the overlap of DNA at the dyad for fully wrapped nucleosomes, and can thus be assigned to the fully wrapped state. For opening angles  $>80^\circ$ , *i.e.* the regime of partially unwrapped nucleosomes, the population splits into two branches, indicating that unwrapping can follow two distinct pathways. In the first pathway, the length of the short arm remains constant while the opening angle increases, suggesting exclusive unwrapping of the long arm. In the second pathway, the length of the short arm correlates positively with the opening angle (slope 0.20 bp/°) consistent with exclusive unwrapping of the short arm. The clearly separated pathways imply that unwrapping is anti-cooperative, *i.e.* that dissociation at one end suppresses unwrapping at the other. Consistently, the 2D distribution of long arm length versus opening angle shows the same behavior (Fig. 5.13). Our observation of anti-cooperative unwrapping is in agreement with previous reports based on single-molecule manipulation and FRET<sup>69</sup> and on cryo-EM,<sup>68</sup> which revealed that unwrapping at one exit site stabilizes binding at the second exit site. Interestingly, a recent study modeling DNA caliper data found better agreement with a model where both arms can unwrap independently as compared to a model that includes

anticooperativity,<sup>174</sup> in contrast to the clear anti-cooperativity visible in our and other previous data.<sup>68;69</sup>

To quantify the propensity to unwrap via the distinct pathways, we simulated AFM images of nucleosomes featuring different levels of anti-cooperative unwrapping (Fig. 5.7b). Again, we fitted a linear combination of 2D Gaussians to the experimental density distribution of the partially unwrapped H3 nucleosomes using the expected positions based on the simulations to obtain population sizes along the different unwrapping pathways (Fig. 5.7c and Fig. 5.13). We observed a small but significant (two-sample t-test  $p = 0.015$ ) preference for long arm opening over short arm opening with probabilities of  $(53.7 \pm 1.6)\%$  and  $(46.3 \pm 1.6)\%$  respectively (mean  $\pm$  SEM from four biological repeats). This preference for long arm opening reflects the non-palindromic nature of the W601 nucleosome positioning sequence: the DNA flanking the nucleosome dyad is less flexible on the long arm side compared to the short arm side (Fig. 5.14) leading to the energetically more favorable unwrapping from the stiffer side. Control measurements with an inverted W601 sequence showed again preferential opening from the less flexible side, which is now the short arm side (Fig. 5.14). Our findings are in line with previous force-induced experimental<sup>69</sup> and computational<sup>175</sup> unwrapping studies. However, in these studies nucleosomes almost exclusively unwrapped from the stiffer side, in contrast to the 54% to 46% partitioning that we observe. The difference might be caused by the experimental configurations: force-induced nucleosome unwrapping with constrained DNA arms requires a nucleosome flip of  $180^\circ$  during unspooling and thus induces strong deformations in the DNA.<sup>175</sup> In contrast, thermal fluctuations and electrostatic interactions of the free DNA arms that drive nucleosome unwrapping in our study might be less influenced by DNA flexibility. Quantifying the 5 bp unwrapping substates, we observe small, but significant differences in the unwrapping profiles for the two sides: unwrapping from the short arm side tends to occur by 20–25 bp, while the long arm side favors unwrapping by 30–35 bp (Fig. 5.7c). These differences are in line with the free energy profile of W601 nucleosome unwrapping from a previous force-induced unzipping study.<sup>66;174</sup>

### 5.2.5 CENP-A nucleosomes do not follow distinct unwrapping pathways

Previous Cryo-EM,<sup>163</sup> H/DX mass spectrometry<sup>176</sup> and AFM studies<sup>105</sup> suggest that centromeric CENP-A nucleosomes exhibit enhanced structural dynamics and plasticity that deviates from canonical H3 nucleosomes. In contrast, magnetic tweezers measurements indicate that force-induced unwrapping and intrinsic stability of CENP-A and H3 nucleosomes are very similar.<sup>177</sup> Previous studies have shown that CENP-A nucleosomes populate more open conformations, *i.e.* conformations with less DNA wrapped, approximately 120 bp compared to 147 bp for H3 nucleosomes.<sup>178;179</sup> The increased unwrapping of CENP-A nucleosomes is more pronounced for nucleosomes reconstituted on  $\alpha$ -satellite DNA compared to nucleosomes reconstituted on the W601 sequence.<sup>180</sup> To test CENP-A stability and unwrapping dynamics, we applied our AFM imaging and analysis pipeline to CENP-A nucleosomes.

The distribution of wrapped length and opening angle for CENP-A nucleo-

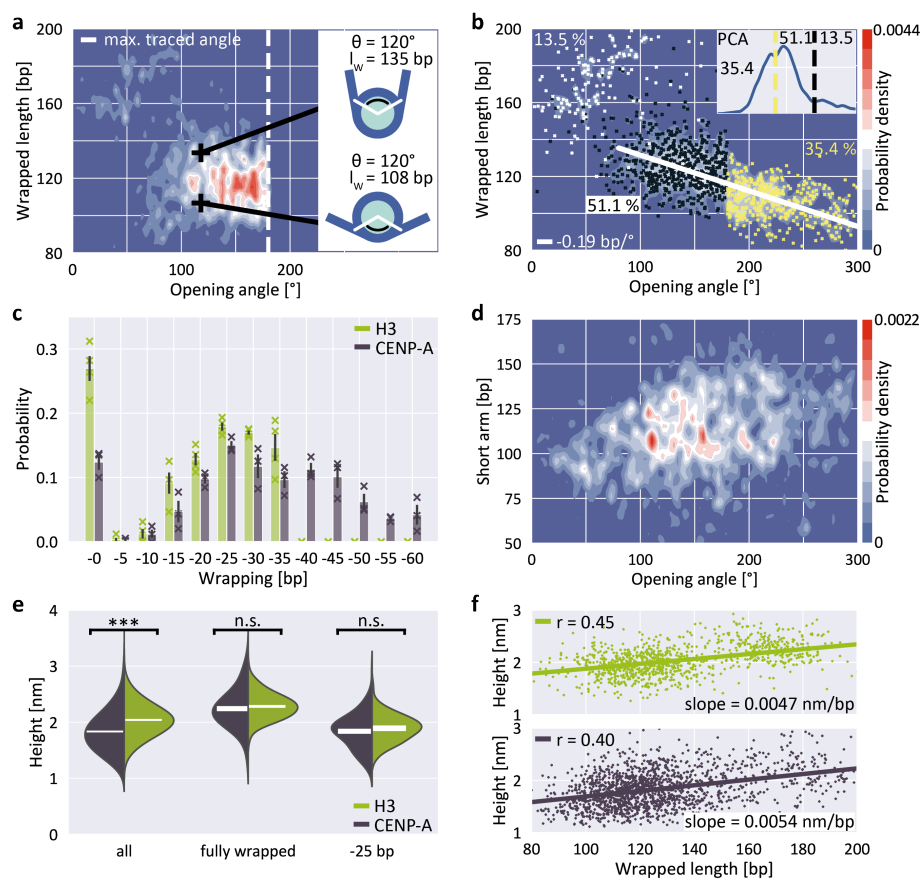


**Figure 5.8: Unwrapping and heights of CENP-A nucleosomes.** **a**, 2D kernel density profile (bandwidth = 2.5°, 2.5 bp) of wrapped length and opening angle for CENP-A nucleosomes (N = 1178, 200 mM NaCl). **b**, 2D kernel density profile (bandwidth = 2.5°, 2.5 bp) of wrapped length and opening angle for CENP-A nucleosomes after correcting the opening angles for folding back at 180°, based on the PCA of volume and wrapped length (inset). **c**, 2D Gaussian fits to the partially unwrapped CENP-A nucleosomes yield the populations of individual states of unwrapping (Fig. 5.13). H3 populations are mean values obtained from four datasets (N = 1011, 1524, 1480 and 815) of nucleosomes from three biological repeats and imaged on two different AFM setups. CENP-A populations are mean values obtained from three datasets (N = 1178, 484 and 467) of nucleosomes from two biological repeats and imaged on two different AFM setups. **d**, 2D kernel density profile (bandwidth = 2.5°, 2.5 bp) of short arm length and opening angle for CENP-A nucleosomes indicating stochastic unwrapping of CENP-A nucleosomes in contrast to the anti-cooperative unwrapping of H3 nucleosomes. **e**, Violin plots of CENP-A and H3 nucleosome heights for the whole ensemble, for fully wrapped nucleosomes and for nucleosomes that wrap ~120 bp DNA. White bars are centered at the mean values of each distribution and thickness represents SEM. The height difference between CENP-A and H3 is highly significant for all nucleosomes combined (two-sample t-test  $p = 1.6 \times 10^{-60}$ ) but not significant when only comparing fully wrapped nucleosomes ( $p = 0.11$ ) or nucleosomes that wrap 120 bp ( $p = 0.12$ ). **f**, Correlation between wrapped length and nucleosome height for H3 (top) and CENP-A nucleosomes (bottom).

somes clearly differs from H3 nucleosomes under the same conditions (200 mM NaCl; compare Fig. 5.8a with Fig. 5.2d). First, only a small fraction of CENP-A nucleosomes populates the fully wrapped state with overlapping DNA arms ( $12.4 \pm 1.7\%$  for CENP-A *vs.*  $27.0 \pm 3.3\%$  for H3, Fig. 5.8 b and c). Second, CENP-A nucleosomes exhibit a shift of the partially unwrapped population towards more unwrapped states compared to H3 nucleosomes. Surprisingly, the clear negative correlation of wrapped length and opening angle for H3 nucleosomes is not apparent for CENP-A nucleosomes (Fig. 5.8a). We note that in our analysis, opening angles  $>180^\circ$  are "folded back" and appear at smaller values (Fig. 5.8a, inset). Correcting the opening angles of nucleosomes separated by the first local minimum of a PCA of volume and wrapped length (Fig. 5.8b, inset) led to the expected negative correlation of opening angle and wrapped length (Fig. 5.8b;  $-0.19$  bp/°). Fitting the populations of unwrapping states by 5 bp steps in the CENP-A nucleosome data (Fig. 5.8c and Fig. 5.13), we find that the most frequented states of CENP-A nucleosomes lie between 25 bp and 35 bp unwrapping (*i.e.* ~120 bp wrapped, in agreement with previous findings<sup>181</sup>), in contrast to H3 nucleosomes where the fully wrapped state is most populated. Further, in contrast to H3 nucleosomes, CENP-A nucleosomes also significantly populate unwrapping states between 40 bp to 60 bp ( $35.4 \pm 4.6\%$  of the total population) unlike H3 nucleosomes and in line with previous work on CENP-A nucleosomes.<sup>181</sup>

Third, in addition to the overall shift to less wrapped states, our CENP-A nucleosome data reveal a striking difference to H3 nucleosomes in wrapping pathways: while the H3 nucleosome data feature a clearly bimodal distribution of short arm

length *vs.* opening angle for angles  $>80^\circ$  (Fig. 5.7a), indicative of anti-cooperative unwrapping, the CENP-A data exhibit no such branching and feature a broad distribution of short arm lengths instead (Fig. 5.8d), suggesting that unwrapping of the two arms is not anti-cooperative for CENP-A nucleosomes.

Recent Cryo-EM work<sup>68</sup> has suggested that DNA unwrapping on one side triggers a conformational change of the adjacent H3  $\alpha$ N, which in turn leads to rearrangement of H3  $\alpha$ N on the opposite side, resulting in stabilization of the DNA contact on the wrapped side. Together, these allosteric changes constitute a latch mechanism that likely contributes to the anti-cooperative unwrapping of H3 nucleosomes. In CENP-A nucleosomes the  $\alpha$ N helix is shortened<sup>163</sup> compared to H3. The lack of anti-cooperative unwrapping revealed by our data suggest that the reduced  $\alpha$ N helix in CENP-A nucleosomes is insufficient for the latch mechanism, leading to stochastic unwrapping of DNA from CENP-A nucleosomes from both sides, in line with a recent molecular dynamics study.<sup>182</sup> Interestingly, we observe that the most unwrapped configurations (Fig. 5.8d, opening angles  $>200^\circ$ , corresponding to  $>40$  bp unwrapped) consistently involve unwrapping of both DNA arms, giving rise to intermediate short arm lengths. This is consistent with the observation that unwrapping of  $>40$  bp, *i.e.* opening angles  $>200^\circ$ , from one side leads to disruption of the overall nucleosome structure<sup>68</sup> and, therefore, nucleosomes with unwrapping of  $>40$  bp exhibit concurrent unwrapping on both sides.

### 5.2.6 Differences in DNA wrapping reconcile conflicting results on CENP-A nucleosomes

Previous AFM studies have revealed significant changes in nucleosome height depending on the incorporation of canonical H3 versus CENP-A histones. In a landmark paper, Dalal and co-workers proposed that the reduced height of CENP-A nucleosomes follows from the transition between tetrameric and octameric states in different phases of the cell cycle.<sup>99;183;184</sup> This interpretation was challenged in a later study, which attributed these differences in height to physical differences between CENP-A and H3 nucleosomes.<sup>100</sup> However, significant height differences for CENP-A and H3 octameric nucleosomes could not be reproduced by other groups, and the issue remains controversial.<sup>98;101–103;185</sup>

In our measurements we find that overall, *i.e.* averaging over all wrapping states, H3 nucleosomes are significantly higher than CENP-A nucleosomes (two sample t-test  $p = 1.6 \times 10^{-60}$ ; Fig. 5.8e), with mean heights of  $(2.04 \pm 0.01)$  nm for H3 (mean  $\pm$  SEM from  $N = 1011$  molecules) and  $(1.83 \pm 0.01)$  nm for CENP-A nucleosomes ( $N = 1645$  molecules). Our results are in agreement with previous work, both in terms of the significant height difference between H3 and CENP-A nucleosomes and in terms of the absolute height values with the study that reported the height differences.<sup>100</sup> However, we observe a significant correlation between wrapped length and measured height (Fig. 5.8f; Pearson's  $R = 0.45$  and  $p = 7.1 \times 10^{-52}$  for H3 nucleosomes and  $R = 0.40$  and  $p = 2.4 \times 10^{-65}$  for CENP-A nucleosomes). Since CENP-A nucleosomes are on average less wrapped (Fig. 5.8c), the correlation between wrapping and height implies that differences in wrapping might account for the reduced height of CENP-A nucleosomes. Comparing only fully wrapped H3 and CENP-A nucleosomes (classified based on the PCA results, see Fig. 5.5a and

Fig. 5.8b), we indeed find mean heights of  $(2.28 \pm 0.01)$  nm ( $N = 315$  molecules) and  $(2.24 \pm 0.02)$  nm ( $N = 205$  molecules), respectively, corresponding to no significant difference in the mean heights (two-sample t-test  $p = 0.11$ ). Similarly, comparing only conformations corresponding to  $\sim 25$  bp unwrapping (119–124 bp), we find mean heights of  $(1.89 \pm 0.03)$  nm ( $N = 80$  molecules) and  $(1.83 \pm 0.02)$  nm ( $N = 167$  molecules), respectively, corresponding to no significant difference in the mean heights (two-sample t-test  $p = 0.12$ ; Fig. 5.8e).

In summary, we find that if we average over all wrapping states, CENP-A nucleosomes are lower than H3 nucleosomes, in agreement with an initial report of nucleosome height difference in AFM.<sup>100</sup> However, if we only consider fully wrapped nucleosomes or only conformations where 120 bp are wrapped, we do not detect a significant difference, similar to follow up work motivated by the initial study.<sup>101;102</sup> While other factors (like differences in mechanical compliance<sup>98</sup> or stability of the histone core<sup>186</sup>) might contribute, our data suggest that the apparent differences in height between H3 and CENP-A nucleosomes can be accounted for by differences in wrapping under our conditions. The apparently conflicting findings might be explained by differences in imaging conditions, for example the different salt conditions used (10 mM NaCl and 1 mM EDTA vs. 150 mM NaCl + 2 mM MgCl<sub>2</sub> vs. 1 mM EDTA only),<sup>100–102</sup> which can significantly alter unwrapping (Fig. 5.5).

### 5.3 Discussion

Quantitative assessment of nucleosome conformations is a key to understanding regulation of DNA accessibility due to the role of nucleosomes in the formation of higher-order chromatin structure,<sup>55;187;188</sup> the recruitment of proteins and complexes with specific enzymatic activities<sup>152</sup> and the effect of nucleosomes on DNA mechanisms such as repair<sup>189</sup> and replication.<sup>190</sup> In this work, we introduce an automated framework that enables high-throughput analysis of AFM images of nucleo-protein complexes and applied it to canonical H3 and centromeric CENP-A nucleosomes. By exploiting correlations between different structural parameters of  $\sim 10\,000$  nucleosomes, we map molecular ensembles along different degrees of freedom, which in turn allows us to extract detailed nucleosome wrapping landscapes. We use simulations of AFM images to understand how tip-convolution in AFM imaging affects the observed structure parameters and to quantify the occupancy of different states of wrapping from our experiments. While the fully wrapped state is the most populated configuration, we observe partial unwrapping of  $\sim 70\%$  of the canonical H3 nucleosomes at close to physiological monovalent salt concentrations ( $[\text{NaCl}] = 200$  mM) and still  $\sim 40\%$  partial unwrapping in the presence of 2 mM MgCl<sub>2</sub> and 50 mM NaCl, in agreement with previous electron microscopy,<sup>93</sup> AFM,<sup>91</sup> and solution SAXS<sup>191</sup> studies of nucleosomes. In fully wrapped nucleosomes, the DNA arms overlap in close proximity to the DNA entry/exit region of the nucleosome core particle. DNA crossover at the exit region presents a significant energy barrier that might regulate nucleosomal DNA readout either by binding of histone H1 to form repressive chromatosomes or by granting access to RNA polymerases<sup>155</sup> and other molecular machines that process the genetic code.

Our data demonstrate pronounced anti-cooperative unwrapping of H3 nucleosomes and preferential unwrapping from the stiffer side of the non-palindromic

W601 sequence in agreement with previous single-molecule and cryo-EM studies.<sup>66;68;69</sup> However, our data show only a slight preference for unwrapping from the stiffer side in contrast to previous studies that have seen it almost exclusively. While our methodology captures a molecular ensemble in thermal equilibrium, previous results were obtained via force-induced unwrapping or for constructs containing only 147 bp of DNA,<sup>68;191</sup> which might account for the differences. Both experimental approaches are of physiological relevance since nucleosomes can be invaded either passively due to spontaneous fluctuations<sup>142</sup> or actively by forces generated by polymerases and chromatin remodelers.<sup>139;141</sup> We speculate that our approach samples the clearly distinct nucleosomal unwrapping landscape for passive invasion of nucleosomes with linker DNA in contrast to previous force-induced unwrapping assays.

In contrast to their canonical H3 counterparts, we find centromeric CENP-A nucleosomes to be substantially less wrapped, with the most populated state corresponding to ~120 bp wrapped DNA. This result is in agreement with previous high-resolution structural studies by X-ray crystallography<sup>137</sup> and cryo-EM<sup>163</sup> that assigned the shortened N-terminal  $\alpha$ -helix of histone H3 to weakened interaction with DNA at the exit points of the nucleosome. More than 30% of the population of CENP-A nucleosomes unwraps >35 bp. Unwrapping >40 bp requires partial opening of both arms, which is suppressed in H3 nucleosomes. Our data are in line with results from force-induced unzipping of nucleosomal DNA: peak-forces associated with the strong barrier between superhelical locations 3.5 and 6.5, *i.e.* up to 40 bp unwrapping, were significantly reduced in yeast centromeric versus H3 nucleosomes.<sup>168</sup> However, DNA–histone interactions closer to the dyad were equally strong for yeast centromeric and H3 nucleosomes preventing unwrapping of more than 40 bp from one side.

Our data show no anti-cooperativity in the unwrapping of CENP-A nucleosomes, in contrast to H3 nucleosomes. We propose that the stabilizing latch mechanism that contributes to anti-cooperativity<sup>68</sup> in H3 nucleosome unwrapping is missing in CENP-A nucleosomes due to the shortened  $\alpha$ N helix. Since CENP-A is a key epigenetic mark to maintain structural integrity of the centromere, we speculate that both stochastic unwrapping and overall decreased DNA wrapping of CENP-A nucleosomes might facilitate binding of proteins to specific DNA sequences in the centromere. For example, the centromere-DNA binding protein complex CBF3 is essential for chromosome segregation and binds selectively to the highly conserved CDEIII DNA sequence found in centromeres.<sup>192</sup> Similarly, CENP-B facilitates centromere formation in humans by recognizing and binding a 17 bp DNA sequence – the CENP-B box – in the centromeric  $\alpha$ -satellite DNA.<sup>193</sup>

## 5.4 Conclusion

In summary, we have developed a high-throughput automated analysis platform and used it to uncover thermally activated pathways of H3 and CENP-A nucleosome wrapping in unprecedented detail, going beyond a single dominant population by providing a full view of the conformational space. Our methodology will facilitate future high-throughput AFM studies that involve structure and interactions of nucleoprotein complexes by either using fast imaging of large molecular ensembles or by time-lapsed imaging of molecular dynamics at the single molecule

level.<sup>83</sup>

Finally, our work demonstrates strong correlations of nucleosomal wrapped length with the entry-exit angle and particle height. This implies that by measuring "local" parameters one can accurately deduce nucleosome wrapping in the context of nucleosome arrays, which opens up exciting opportunities to quantify reconstituted or purified higher order chromatin assemblies.

## 5.5 Methods

### DNA purification and nucleosome reconstitution

DNA was PCR amplified from a GeneArt High-Q String DNA fragment (Thermo Fisher Scientific, Waltham, Massachusetts) containing the Widom 601 positioning sequence. The DNA was purified using a QIAquick PCR purification kit (Qiagen, Hilden, Germany) and subsequently eluted to a volume of 30  $\mu\text{L}$  with ddH<sub>2</sub>O. Histone proteins were purchased from EpiCypher (Durham, North Carolina). While the H3 histones were available as part of recombinant human histone octamers, CENP-A histones were purchased as CENP-A/H4 tetramers and added to the dialysis chamber together with an equimolar ratio of H2A/H2B tetramers. Nucleosome reconstitution was performed via salt gradient dialysis.<sup>149</sup> The dialysis chamber contained 0.65  $\mu\text{g}$  of the histone octamers and 3  $\mu\text{g}$  of the 486 bp DNA at 2 M NaCl and was placed in one liter of high-salt buffer at 2 M NaCl. Over a course of 15 hours, three liters of low-salt buffer at 50 mM NaCl were transferred to the high-salt buffer at 4 °C. Finally, the dialysis chambers were moved to one liter of low-salt buffer for three hours. The resulting nucleosomes are well positioned on the DNA construct by the Widom 601 positioning sequence (Fig. 5.15).

### AFM sample preparation and imaging

The sample containing bare DNA and reconstituted nucleosomes – usually 30% to 50% of the DNA strands do not bind to histones – was incubated at the desired salt concentration (10 mM NaCl/50 mM NaCl/200 mM NaCl and 10 mM Tris-HCl, pH 7.6, for all measurements) for 1 min on ice. The sample ( $V = 25 \mu\text{L}$ ) was then deposited on a freshly cleaved poly-L-lysine (0.01% w/v) coated muscovite mica for 30 seconds and subsequently rinsed with 20 mL of milliQ water before drying with a gentle stream of filtered N<sub>2</sub> gas.

We used two different commercial AFM instruments for imaging. All AFM images were acquired in tapping mode at room temperature. One set of images was acquired on a Multimode VIII AFM (Bruker, Billerica, Massachusetts) using silicon tips (AC160TS, drive frequency of 300–350 kHz, tip radius 7 nm, Olympus, Tokyo, Japan). Images were scanned over a field of view of 3  $\mu\text{m} \times 3 \mu\text{m}$  at 2048  $\times$  2048 pixels with a line scanning speed of 1 Hz. Independent measurement repeats were performed on a Nanowizard Ultraspeed 2 (JPK, Berlin, Germany) with reflex gold coated tips (USC-F5-k30, drive frequency 5000 kHz, tip radius <10 nm, Nanoworld, Neuchâtel, Switzerland). Here, images were scanned over a field of view of 6  $\mu\text{m} \times 6 \mu\text{m}$  at 4096  $\times$  4096 pixels with a line scanning speed of 3 Hz or over a field of view of 12  $\mu\text{m} \times 12 \mu\text{m}$  at 8192  $\times$  8192 pixels at 3 Hz line scanning speed (Fig. 5.1b). For H3 nucleosomes, four data sets were acquired at 200 mM

NaCl and 10 mM Tris over three separate nucleosome reconstitutions. For CENP-A nucleosomes, three data sets were acquired at 200 mM NaCl and 10 mM Tris over two separate nucleosome reconstitutions.

### AFM image analysis

We developed an automated image analysis pipeline to analyze the flattened AFM images, which defines zero height as the average level of the mica surface. For the AFM data analyzed in this work, a background height threshold of 0.16 nm and 0.25 nm was applied for images taken by the Bruker and the JPK instrument respectively. The background height threshold affects the detection rate of DNA and nucleosomes, but does not alter the measured structure parameters such as nucleosome volume or height as the threshold is only used for detection and not in the further analysis of the molecular images.

Bare DNA strands were traced with 5 nm segments<sup>109</sup> from both sides separately and the mean value was used as contour length. Over 95% of the viable molecules in the images were detected automatically. Here, viable molecules are defined as molecules that do not have overlaps with other molecules and can be analyzed by manual tracing. To achieve an even higher detection rate, manual input allowed the separation of unclassified objects (for example for two DNA arms that slightly overlap and thus prevent automated detection). This way, 98% of all viable nucleosomes of the example image were detected (Fig. 5.9). Even with manual help for detecting and classifying individual molecules, all measured and presented structure parameters were obtained by the structure analysis routine of the toolbox. The four H3 data sets at 200 mM NaCl consist of 1011, 1524, 1480 and 815 analyzed nucleosomes. The three CENP-A datasets consist of 1178, 484 and 467 analyzed nucleosomes.

### AFM image simulations

Fully wrapped nucleosome images were simulated by creating a disk with a diameter of 11 nm and uniform height and simulating 2D worm-like chains with lengths of 233 bp and 106 bp that protrude the disk at an opening angle of 66.5°. The direction of the DNA chains was deduced from the crystal structure of the canonical nucleosome (PDB 1KX5, Fig. 5.2, Fig. 5.10). Consecutively, the DNA was dilated to its expected width of 2 nm and random noise in combination with a Gaussian filter ( $\sigma = 2$  nm) was applied to mimic the effect of tip convolution. Partially unwrapped nucleosomes were simulated by adding base pairs to one end of the simulated chains in 5 bp steps, increasing the opening angle by 4.45° per base pair of unwrapping (based on 147 bp wrapped over a total of 654° in the crystal structure) and adjusting the direction of the protruding DNA arms. Similarly, synthetic images of bare DNA were simulated with a 2D worm-like chain of 486 bp and the same steps of dilation and tip convolution. The synthetic bare DNA images were analyzed for their average DNA contour length that is needed to calculate the wrapped length in nucleosomes in our automated readout pipeline. The simulated images were analyzed with the same automated readout software as the experimental images.

## Acknowledgements

We thank Philipp Korber and Felix Müller-Planitz for help with initial nucleosome reconstitutions, Herlinde De Keersmaecker for assistance with AFM imaging, and Thomas Nicolaus for help with sample preparation. This work was funded by the Deutsche Forschungsgemeinschaft (DFG, German Research Foundation) through SFB863 – project ID 111166240. W. F., T. B., and S. D. F. acknowledge KU Leuven – internal funds (IDO) and Fund for Scientific Research (FWO).

## 5.6 Supplementary Information

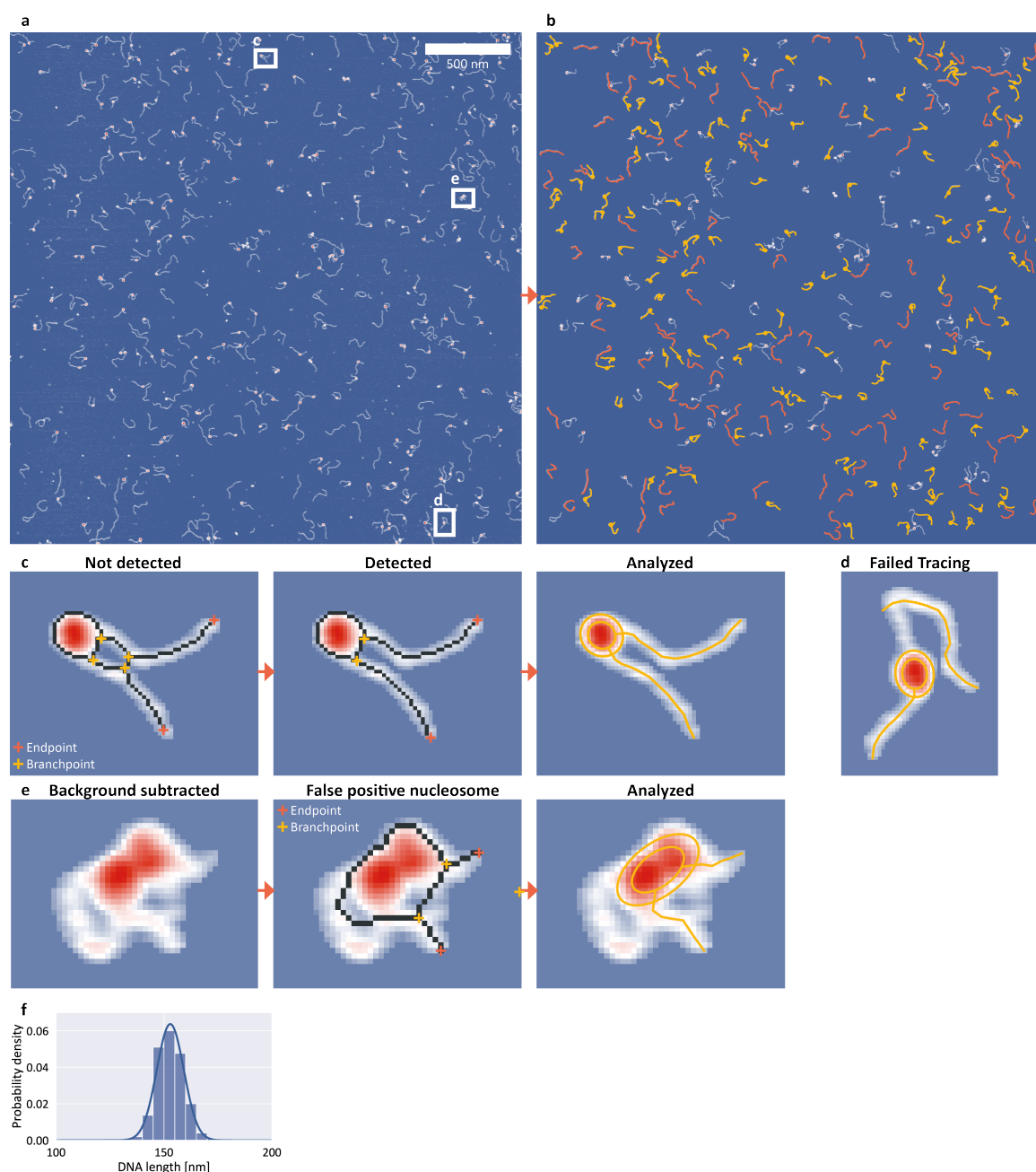


**Figure 5.9: Detection efficiency, manual molecule classification, and DNA length.** **a**, AFM topographic image of bare DNA and nucleosomes to assess the detection rate of the automated tracing. The total field of view is  $3 \mu\text{m} \times 3 \mu\text{m}$  and was recorded with  $1.46 \text{ nm/pixel}$ . **b**, Analysis of the topographic image from panel **a**. 112 bare DNA strands (orange) and 131 nucleosomes (yellow) were detected and analyzed automatically with manual detection help as described in **c**. To quantify the detection rate and to assess imaged molecules that were not classified as either DNA or nucleosome in the first fully automated step, the image was inspected visually. The fully automated classification and tracing routine detected 95% of all manually analyzable DNA and nucleosomes in the field of view that did not show overlaps with other molecules. **c**, Example how manual intervention can improve classification of molecules not assigned to bare DNA or nucleosome molecules in the first automatic classification step. In the case depicted here, too many branchpoints (four instead of two) are detected and thus the nucleosome was not automatically classified. After manually removing the overlapping pixels of the DNA arms, the nucleosome is properly classified and the automated analysis framework traces the structure parameters. Overall, such manual classification help for unclassified molecules enabled tracing of up to 98% of manually analyzable molecules. **d**, Example of a false negative, *i.e.* a molecule that by visual inspection appears to constitute a valid nucleosome or DNA, but is not traced properly. The tracing fails due to the strong bending of the long arm. Overall, 2% of molecules that we identified as valid by visual inspection fall into this category. **e**, Example of a false positive, *i.e.* a molecule that is classified as a valid nucleosome or DNA by our algorithm, but excluded by visual inspection. In the image shown in **a**, a total of 9 false positive molecules were traced by the automated toolbox. For this work, false positives were removed for further analysis. The example molecule contains two branchpoints and two endpoints and is thus classified as a nucleosome. **f**, Histogram of bare DNA lengths of all data sets measured in 200 mM NaCl presented in this work. We find a contour length of  $l_c = 152.9 \pm 6.3 \text{ nm}$  (mean  $\pm$  std from 5651 molecules).

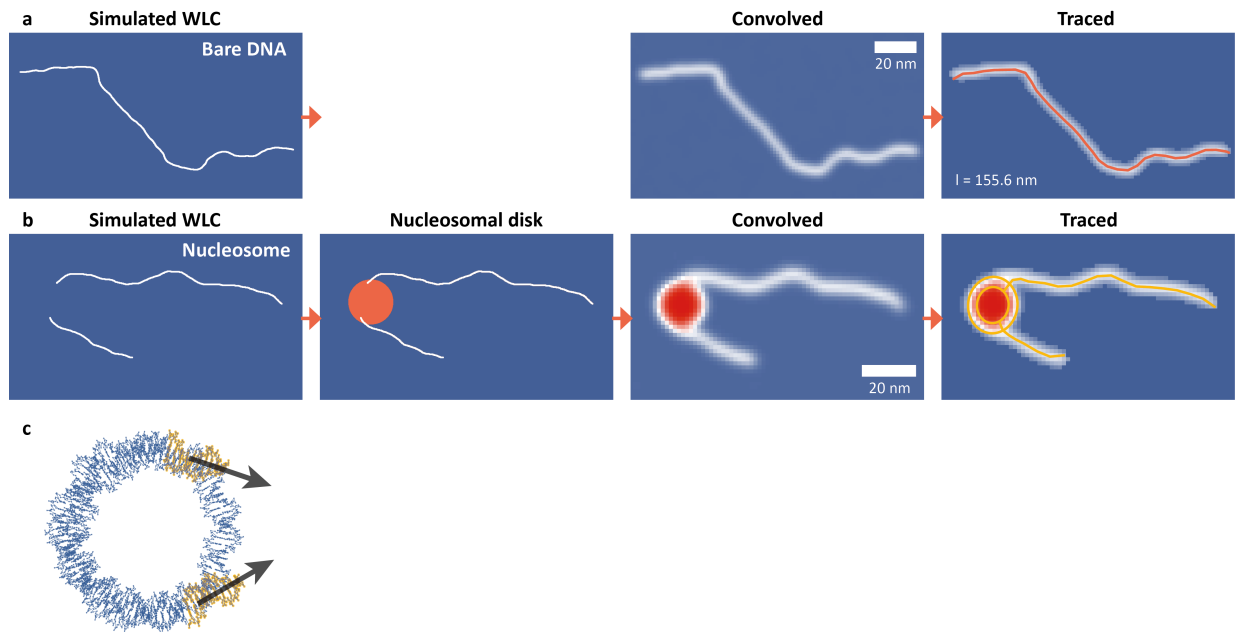


**Figure 5.10: DNA and nucleosome simulations to quantify the effect of AFM tip convolution.** **a**, 486 bp DNA were simulated using the worm-like chain polymer model with a persistence length of 40 nm and a rise per base pair of 0.33 nm/bp. The simulated DNA backbone was dilated to a width of 2 nm and convolved with a Gaussian filter after applying random noise to mimic the effect of AFM tip convolution. The simulated DNA strands were then traced with our automated analysis pipeline using the same settings as used for experimental data. See Methods for details. **b**, Simulation of nucleosomes consisted of generating two DNA arms (106 bp and 233 bp for the fully wrapped nucleosome) based on the worm-like chain model that protrude from the nucleosomal disk. The orientation of the protruding DNA arms was deduced from the crystal structure (panel **c**), for details see the section "AFM image simulations" in Methods. The nucleosome depicted here is unwrapped by 35 bp from the long arm side. **c**, The crystal structure of the nucleosome core particle yields the orientation of the DNA arms and the nucleosomal opening angle of  $66.5^\circ$  for fully wrapped nucleosomes. Rendered from PDB 1KX5. For partially unwrapped nucleosomes the DNA orientation and opening angle are adjusted accordingly (Methods).

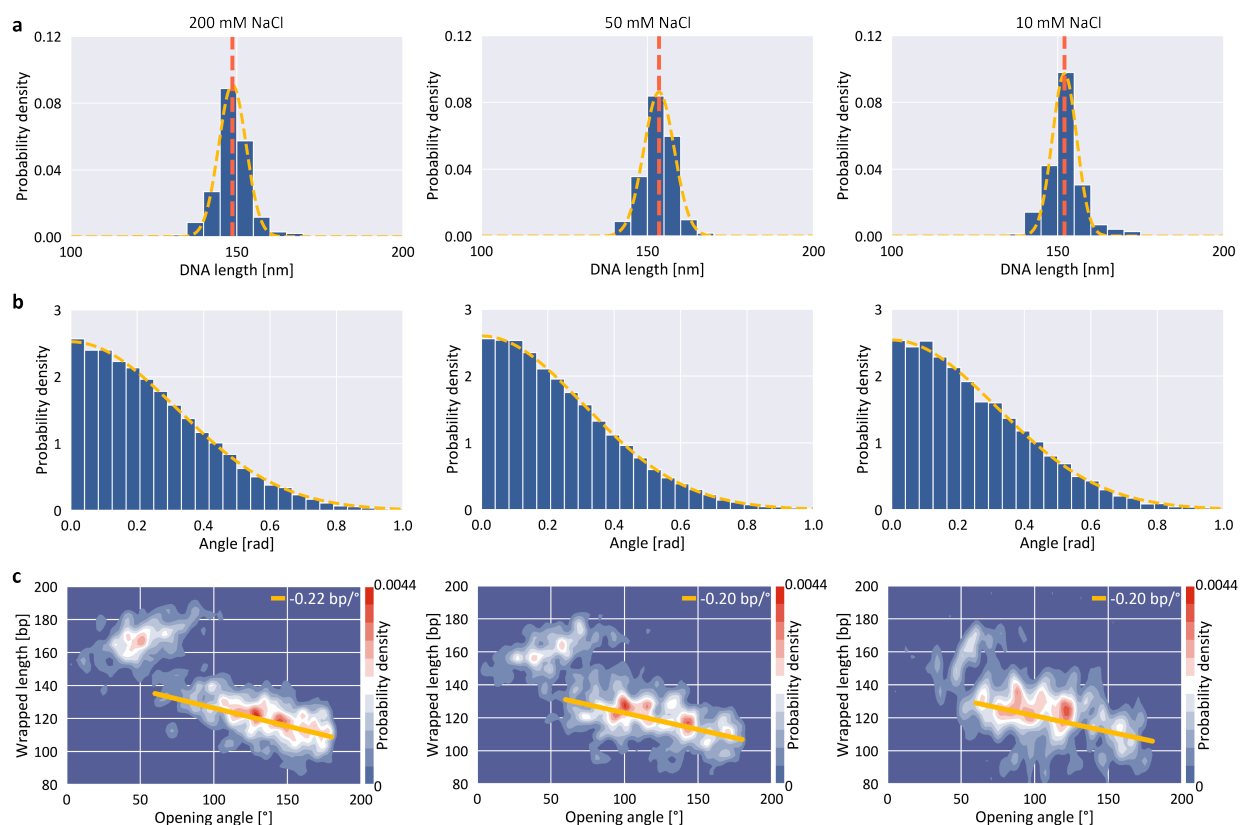


**Figure 5.11: Effect of salt concentration on DNA contour and persistence length.** **a**, Bare DNA lengths of the data presented in Figure 5.5 for different salt concentrations. The Gaussian fits yield contour lengths of  $148.7 \pm 4.1$  nm,  $153.4 \pm 4.6$  nm and  $152 \pm 3.7$  nm for NaCl concentrations of 200 mM, 50 mM and 10 mM respectively ( $N = 888, 797,$  and  $294$ ). **b**, The DNA length is determined by tracing its contour with segments of 5 nm length. The distribution of angles  $\alpha$  between consecutive 5 nm segments can be used to determine the persistence length by fitting ADD FORMULA with  $z = l_{segment} / l_{persistence}$ . The fits yield persistence lengths of 49.5 nm, 53.0 nm and 50.3 nm for NaCl concentrations of 200 mM, 50 mM and 10 mM respectively ( $N = 24077, 22338,$  and  $9995$ ). **c**, The slopes of wrapped length vs. opening angle for partially unwrapped nucleosomes are  $-0.22$  bp/°,  $-0.20$  bp/° and  $-0.20$  bp/° for NaCl concentrations of 200 mM, 50 mM and 10 mM respectively. The slopes agree well with the slope predicted from simulated data (Figure 5.4,  $-0.23$  bp/°) indicating that nucleosomes attach to the surface in a flat geometry with the DNA gyres parallel to the surface for a broad range of ionic conditions.

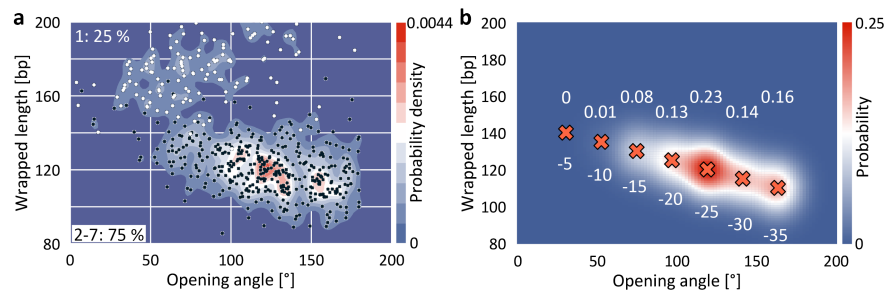


**Figure 5.12: Surface functionalization control.** **a**, 2D kernel density profile of nucleosome opening angle and wrapped length at 200 mM NaCl and 10 mM Tris (N = 558). The surface was functionalized using 0.001% w/v poly-L-lysine in contrast to the 0.01% w/v poly-L-lysine concentration used for the data presented in this work. **b**, 2D Gaussian fits to the partially unwrapped nucleosomes. Numbers indicate the unwrapping in base pairs and the population sizes. The wrapping states for H3 nucleosomes measured at 200 mM NaCl agree for both poly-L-lysine concentrations (see H3 nucleosome population sizes measured at 0.01% poly-L-lysine in Figure 5.7c).

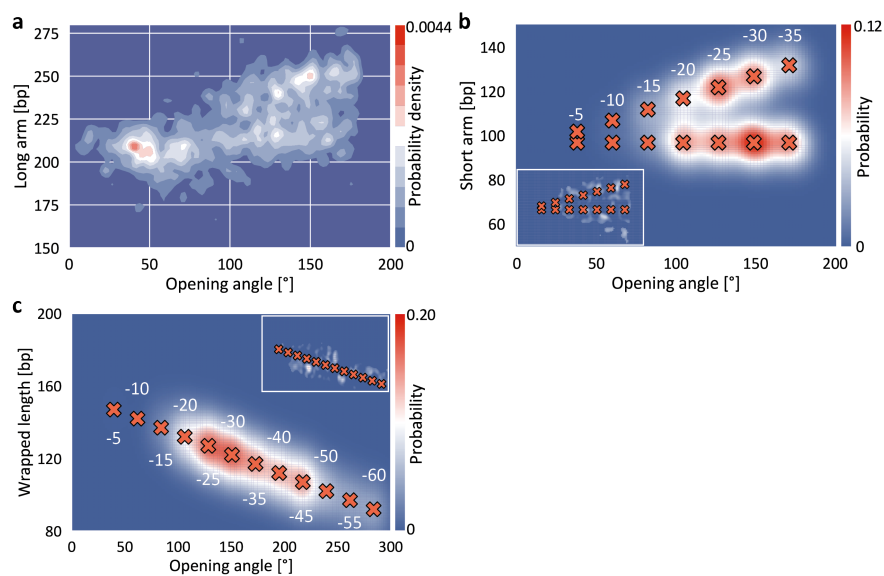


**Figure 5.13: Determination of the occupancies of different wrapping states.** a, 2D kernel density profile (bandwidth =  $2.5^\circ$ , 2.5 bp) of long arm length and opening angle for the H3 nucleosome data set at 200 mM NaCl presented in Figure 5.7. The data for long arm length vs. angle are overall noisier than the data for the short arm length (Figure 5.7a) as expected from the broadening of the contour length distribution for a longer length. b, Fit of 14 2D Gaussians to the density distribution of short arm length and opening angle for the partially unwrapped H3 nucleosomes (Figure 5.7a) measured at 200 mM NaCl ( $N = 696$ ). The inset represents the difference between the measured and the fitted 2D density profile, *i.e.* the residuals of the fit. The occupancies determined from the fits are shown in Figure 5.7c. c, Fit of 12 2D Gaussians to the density distribution of wrapped length and opening angle for the partially unwrapped CENP-A nucleosomes (Figure 5b) measured at 200 mM NaCl ( $N = 1019$ ). The inset represents the difference between the measured and the fitted 2D density profile, *i.e.* the residuals of the fit. The occupancies determined from the fits are shown in Figure 5.8c.

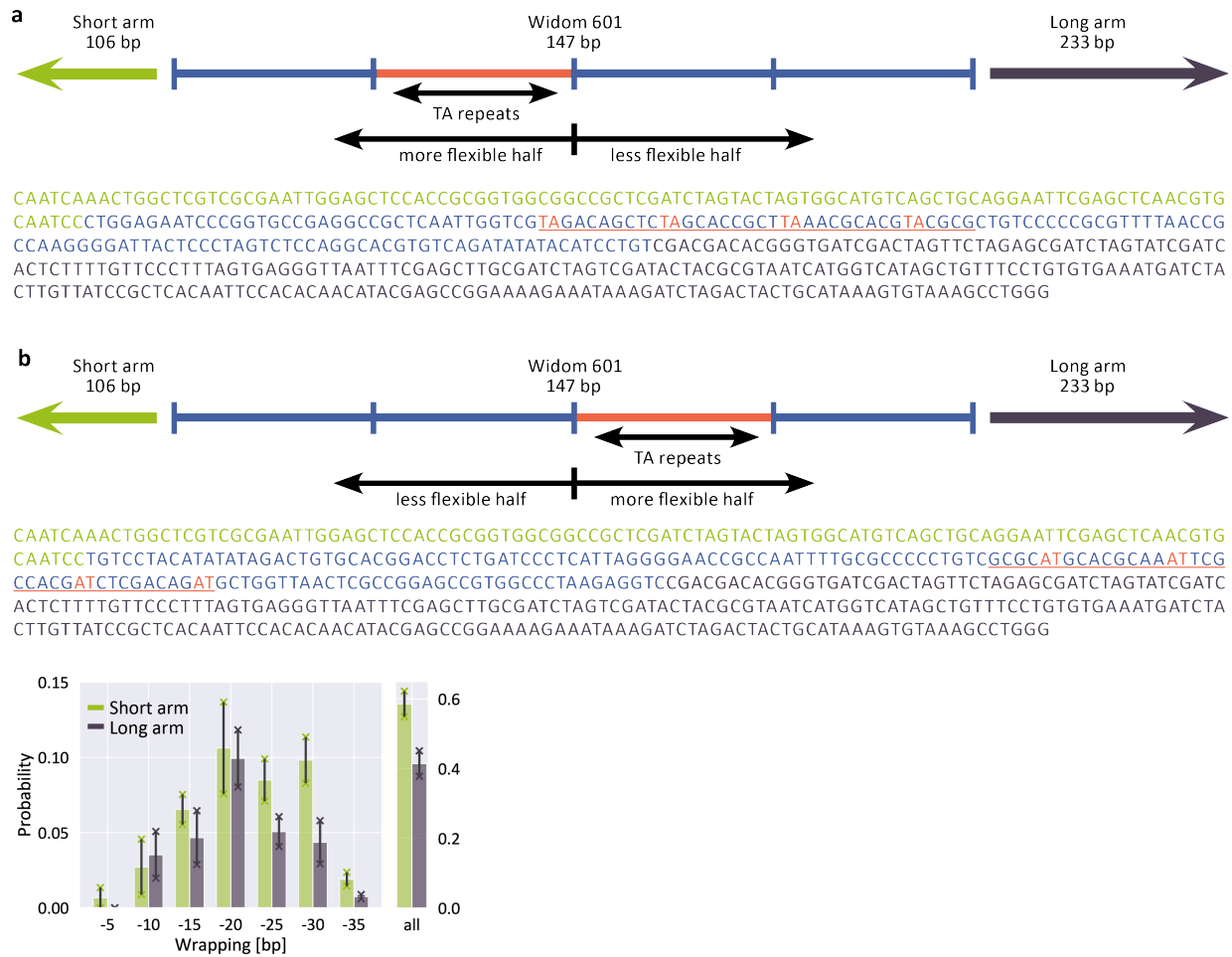


**Figure 5.14: Non-palindromic nature of the W601 positioning sequence.** **a**, The 486 bp DNA construct contains the W601 nucleosome positioning sequence (147 bp) flanked by a short arm (106 bp) and a long arm (233 bp). Four TA repeats with a 10 bp periodicity on the short arm half of the W601 sequence induce the higher flexibility of the half of the W601 sequence on the short arm side<sup>17</sup>. **b**, As a control measurement the W601 sequence was flipped such that the more flexible half of the W601 sequence lies on the opposite side – the long arm side – compared to the data presented in Figure 5.7. Analysis of the unwrapping pathways of the partially unwrapped nucleosomes (69% of all nucleosomes) yields a preference for short arm opening over long arm opening with probabilities of  $(58.6 \pm 3.7) \%$  and  $(41.4 \pm 3.7) \%$  respectively (mean  $\pm$  SEM from two data sets,  $N = 598$  and  $559$ ).

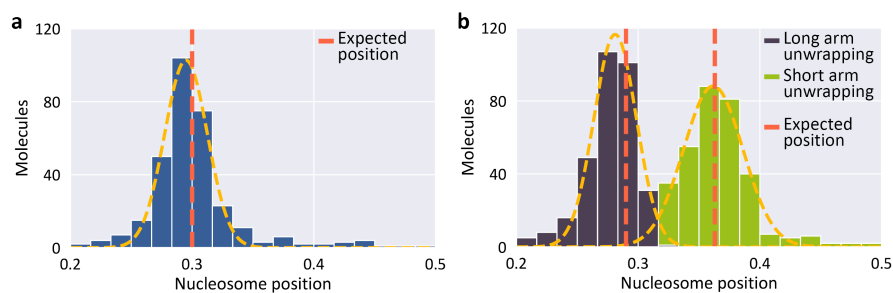


**Figure 5.15: W601 nucleosome positioning.** **a**, Positioning of the fully wrapped nucleosomes along the DNA for the H3 nucleosome dataset presented in Figure 5.7. Yellow dashed line is a Gaussian fit (centered at  $0.29 \pm 0.02$ ). The nucleosome position is calculated by dividing the short arm length by the sum of short arm and long arm length. From the DNA construct, the arms of a fully wrapped nucleosome are expected to be 106 bp and 233 bp (Figure 5.1). However, since for fully wrapped nucleosomes the exiting DNA arms overlap, the length of the arms is underestimated by 10 bp each as described in Figs. 5.2 and 5.4. Thus, the expected nucleosome position of fully wrapped nucleosomes is  $(106 \text{ bp} - 10 \text{ bp}) / (106 \text{ bp} - 10 \text{ bp} + 233 \text{ bp} - 10 \text{ bp}) = 0.30$ . **b**, Positioning of the partially unwrapped nucleosomes along the DNA for the dataset presented in Figure 5.7a. The anti-cooperative unwrapping of H3 nucleosomes leads to different expected positions for nucleosomes that partially unwrap via the short arm or via the long arm. The distribution of partially unwrapped nucleosomes peaks at 120 bp of wrapping (Figure 5.2a) implying that one of the two arms has to unwrap 27 bp compared to canonical nucleosomes with 147 bp wrapped. Thus, the expected position for nucleosomes unwrapping via the long arm or via the short arm is  $(106 \text{ bp}) / (106 \text{ bp} + 233 \text{ bp} + 27 \text{ bp}) = 0.29$  and  $(106 \text{ bp} + 27 \text{ bp}) / (106 \text{ bp} + 27 \text{ bp} + 233 \text{ bp}) = 0.36$  respectively. The fitted Gaussians center at  $0.28 \pm 0.02$  and  $0.36 \pm 0.02$  for the distributions unwrapping via the long arm and via the short arm respectively.

# 6

## Quantifying epigenetic modulation of nucleosome breathing by high-throughput AFM imaging

Nucleosomes are the basic units of chromatin and critical to the storage and expression of eukaryotic genomes. Chromatin accessibility and gene readout are heavily regulated by epigenetic marks of which post-translational modifications of histones play a key role. However, the mode of action and the structural implications on the single-molecule level of nucleosomes is often still poorly understood. Here, we apply a high-throughput AFM imaging and analysis pipeline to investigate the conformational landscape of the nucleosome variants H3K36me3, H3S10phos and H4K5/8/12/16ac. Our data set of >25,000 nucleosomes reveals nucleosomal unwrapping steps corresponding to 5 bp DNA. We find that H3K36me3 nucleosomes unwrap significantly more than wild type nucleosomes and additionally unwrap stochastically from both sides similar to CENP-A nucleosomes and in contrast to the highly anti-cooperative unwrapping of wild type nucleosomes. Nucleosomes with H3S10phos or H4K5/8/12/16ac modifications show unwrapping populations similar to wild type nucleosomes and also retain the same level of anti-cooperativity. Our findings help putting the mode of action of these modifications into context: While H3K36me3 likely partially acts by directly affecting nucleosome structure on the single-molecule level, H3S10phos and H4K5/8/12/16ac must predominantly act through higher-order processes. Our analysis pipeline is readily applicable to other nucleosome variants and will facilitate future high-resolution studies of the conformational landscape of nucleo-protein complexes.<sup>1</sup>

---

<sup>1</sup>This chapter was reproduced from *Konrad et al., 2021*, published on bioRxiv and under review at Biophysical Journal. Author contributions: All authors designed research. S.F.K. performed research, analyzed data, and wrote the manuscript with input from all authors.

## 6.1 Background

Nucleosomes are the fundamental units of compaction of eukaryotic DNA into chromatin and function as regulators of gene readout and activity<sup>15;55;117</sup>. Canonical nucleosome core particles consist of two copies each of the four histones H2A, H2B, H3 and H4 assembled into a histone octamer that is wrapped by ~147 bp of DNA<sup>60;138</sup>. Electrostatic interactions and specific molecular contacts stably pack the DNA onto the histone octamer, yet DNA breathing, sliding, gaping, and loosening allow for nucleosomal dynamics on millisecond to minute time scales<sup>16;82;85</sup>.

Post-translational modifications (PTMs) of histones play a key role in the formation of higher order chromatin structure<sup>55;187;188;194–196</sup>, the recruitment of proteins and complexes with specific enzymatic activities<sup>152</sup>, and the maintenance of DNA repair<sup>189</sup> and replication<sup>190</sup>. Numerous histone variants and PTMs alter histone-histone and histone-DNA interactions<sup>118;197;198</sup> to yield nucleosomal structures with varying degrees of stability and DNA wrapping. Specifically, PTMs at the N-terminal tails of histones H3 and H4 located next to the DNA entry-exit sites can affect DNA opening dynamics by introducing additional charge, by neutralizing existing charge, or by adding steric constraints<sup>15;124</sup>. Among the astonishing number of PTMs<sup>199;200</sup>, the most frequent PTMs at the histone-DNA interface are methylations, acetylations and phosphorylations<sup>15;152</sup>. Acetylation neutralizes the positive charge of lysine and phosphorylation introduces negative charge. Methylation does not alter the charge of the histone protein but, similar to acetylation and phosphorylation, adds steric bulk to the system.

While many studies have investigated post-translational modifications (PTMs) with respect to their effects on nucleosomal structural dynamics<sup>153;201</sup> and on the interaction with nucleosome- or DNA-binding proteins<sup>202–204</sup>, a detailed investigation of the effect of distinct PTMs on nucleosome wrapping is currently lacking. It is critical to understand the direct effects of PTMs on nucleosome conformations, as they can influence the accessibility of nucleosomal DNA for readout and processing and can modulate the conformational landscape that underlies interactions with additional binding partners.

Here, we use a high-throughput pipeline based on atomic force microscopy (AFM) imaging to investigate the conformational landscape of nucleosome variants with several key post-translational N-terminal tail modifications on histones H3 and H4: H3K36me<sub>3</sub>, H3S10phos and H4K5/8/12/16ac (Fig. 1a). These specific modifications are selected for several reasons: First, our goal is to investigate a range of different nucleosome modifications and, therefore, cover trimethylation, acetylation and phosphorylation. Second, we aim for modifications at different positions in the histones. While H3K36me<sub>3</sub> and H4K5/8/12/16ac lie close to the DNA entry/exit region of histones H3 and H4 respectively, H3S10phos is located more distal towards the start of the N-terminal tail of histone H3. Third, for H3K36me<sub>3</sub><sup>205;206</sup> and H4K5/8/12/16ac<sup>207</sup>, previous measurements of the nucleosome structure found no direct effect of the modifications. Yet, due to the close proximity of both modifications to the DNA entry/exit site, we hypothesized that these PTMs could have an effect on the nucleosome wrapping landscape and aimed to detect it with our sensitive assay. Likewise, H3S10phos is an interesting modification as it is involved in both transcriptional activation and chromatin compaction<sup>208</sup>, two structurally op-

posed processes, therefore raising the question whether H3S10phos has structural implications on the nucleosome itself or merely acts as a protein binding platform.

AFM imaging is a powerful tool to probe DNA and nucleosome structure<sup>83;94;112;140;155;209;210</sup> and we have recently developed a multi-parameter image analysis pipeline to quantify the wrapping of nucleosomes with nanometer resolution, label-free, and at the single-molecule level<sup>112</sup>. Here, we have improved the resolution of our assay by adding a deconvolution step to allow for more accurate parameter tracing, enabling the direct observation of the nucleosomal unwrapping periodicity of 5bp from nucleosomal opening angles. We find nucleosomes with the H3K36me3 modification to occur significantly less likely in the fully wrapped state compared to canonical nucleosomes and to exhibit stochastic instead of anti-cooperative unwrapping. In contrast, H4K5/8/12/16ac and H3S10phos do not show significant changes in both unwrapping and anti-cooperativity compared to canonical nucleosomes. We discuss these results in the context of biological function and epigenetic regulation of genome organization.

## 6.2 Results

### 6.2.1 Quantifying nucleosome conformations *via* automated AFM image analysis with deconvolution

We assembled nucleosomes by salt gradient dialysis under sub-stoichiometric conditions, such that the final sample contains bare DNA and predominantly mono-nucleosomes. We use a 486 bp DNA construct that features a W601 nucleosome positioning sequence<sup>70</sup> (147 bp) flanked by a short DNA arm (106 bp) and a long arm (233 bp) (Fig. 1b and Methods). We deposited samples from aqueous buffer on poly-L-lysine coated mica prior to rinsing and drying of the sample. High-resolution images of the deposited nucleosome samples were obtained by amplitude modulation AFM in air (Fig. 6.1).

To quantify nucleosome conformations from the AFM images, we build on our previously published AFM image analysis pipeline to trace bare DNA and nucleosomes in the AFM images by multi-parameter analysis<sup>112</sup> and extend it by adding an additional deconvolution step that allows for more accurate tracing. The tracing consists of two steps: First, bare DNA and nucleosomes are detected and classified by subtracting the background and consecutively utilizing the topology of the one pixel wide backbone – the skeleton – of the molecules (Supplementary Fig. 6.5). Second, structural parameters of the classified molecules are extracted by automatically tracing the molecules with the custom analysis software. The extracted parameters comprise contour length and bend angles for bare DNA and core particle height and volume, arm lengths, and opening angle for nucleosomes (Fig. 6.1e-h). The vectors connecting the ends of the arm entry/exit region of the core particle and the center of the core particle define the nucleosome opening angle. In particular, the combined information of free DNA contour length and opening angle enables to identify the unwrapping state of each nucleosome, *i.e.* to classify how the DNA wraps around the histone core.

To further increase the accuracy of our assay compared to previous applications of AFM imaging to nucleosome conformations, we implemented an image deconvolution step. In general, the dimensions of molecules are overestimated in AFM

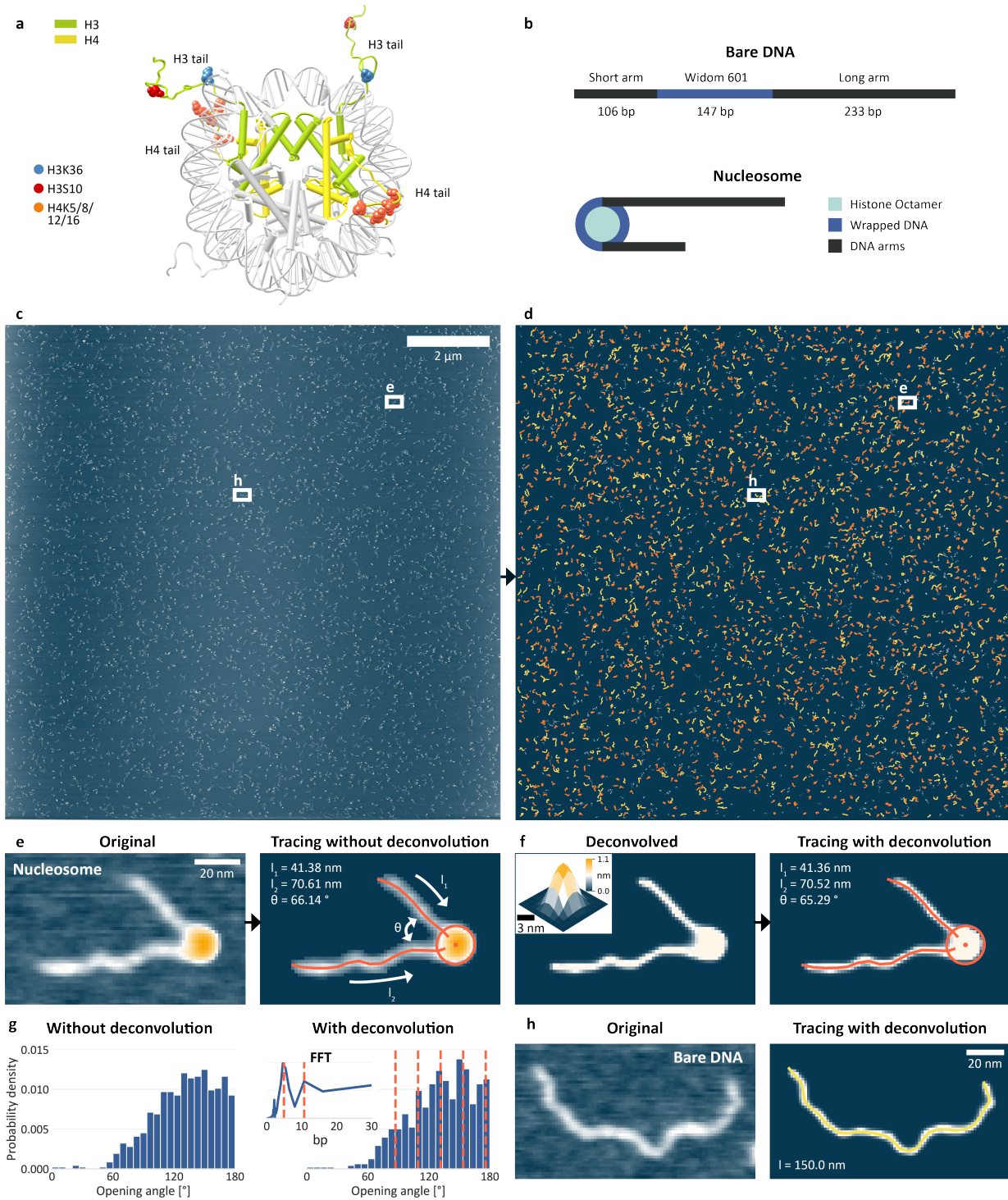


**Figure 6.1: DNA and nucleosome structure parameters from automated AFM image analysis.** **a**, Crystal structure of a canonical nucleosome (PDB 1KX5). Colored spheres represent the positions of the modified amino acids in the histone tail considered in this work. Among the three histone tail modifications investigated are H3K36me3 (three additional methyl groups at lysine 36 of histone H3 – blue spheres), H3S10phos (phosphorylation of H3 histones at serine 10 – red spheres) and H4K5/8/12/16ac (acetylation of H4 histones at lysines 5, 8, 12 and 16 – orange spheres). **b**, Schematic of the construct used throughout this work. The 486 bp DNA consists of a 147 bp W601 nucleosome positioning sequence that is flanked by a short and a long arm of 106 bp and 233 bp, respectively. Histone octamers contain two copies each of H2A, H2B, H3 and H4. **c**, AFM image of bare DNA and nucleosomes with a field of view of 12  $\mu\text{m}$   $\times$  12  $\mu\text{m}$  at a resolution of 1.46 nm/pixel (8192<sup>2</sup> pixels). **d**, Traces of 901 bare DNA strands (orange) and 1624 nucleosomes (yellow) obtained by the automated image analysis pipeline from the image shown in **c**. **e**, Zoom of a nucleosome image before and after tracing. The zoom area is indicated in panels **c** and **d**. **f**, Same nucleosome image as panel **e** after Richardson-Lucy deconvolution. The inset displays the shape of the AFM tip deduced from the bare DNA molecules in the same AFM image and used for deconvolution. **g**, Opening angle distribution for the same data set analyzed without and with deconvolution. The deconvolved data shows the 20° (5 bp) unwrapping periodicity of nucleosomes (N=716, only partially unwrapped nucleosomes shown). **h**, Bare DNA before and after tracing.

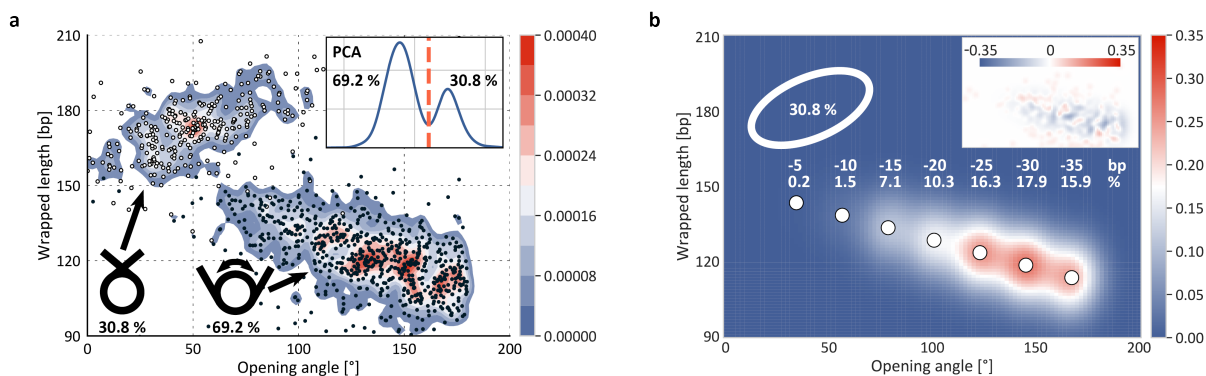


**Figure 6.2: Estimating nucleosome wrapping populations.** a, Wrapped length versus opening angle distribution for canonical nucleosomes. White and black circles represent individual nucleosomes ( $N = 1035$ ), the colored contours are the 2D kernel density estimate. The inset shows a principal component analysis (PCA) of wrapped length and volume that is used to separate the two nucleosome populations (fully vs. partially wrapped). b, 2D Gaussians fit to the density distribution of the partially unwrapped nucleosomes. The Gaussian amplitudes represent the populations of the 5 bp unwrapping substates; the inset shows the residuals of the fit.

imaging due to the finite size of the AFM tip<sup>47;112</sup>. In particular, we find that tip convolution obscures the exact entry/exit position of DNA in the nucleosome images. We estimate the shape of the AFM cantilever tip (Fig. 6.1f inset, Supplementary Fig. 6.6 and Methods) from the bare DNA in our images and typically find tip shapes with an end radius of 5-6 nm (Fig. 6.1f inset) in line with the size as specified by the manufacturer (see Methods). We use this tip shape estimate for subsequent image deconvolution based on the Richardson-Lucy algorithm<sup>211;212</sup> (see Methods). Applying the tip deconvolution leads to sharper images, in particular evident from the DNA paths (Fig. 6.1f, h).

Comparing the opening angles measured with and without image deconvolution, demonstrates the considerable impact of this approach (Fig. 6.1g). While the angle distribution of nucleosomes traced without deconvolution gives a broad and relatively featureless distribution of opening angles, the distribution of opening angles traced after applying the deconvolution clearly indicates a periodicity in the opening angle distribution of  $\sim 20^\circ$ , *i.e.* 5 bp of unwrapping (Fig. 6.1g, inset – a fully wrapped nucleosome wraps 147 bp in  $\sim 1.7$  turns). This 5 bp unwrapping periodicity ultimately stems from the periodicity of the DNA helix and is in line with results from single-molecule DNA force spectroscopy experiments<sup>168;169</sup> and with cryo-EM observations of nucleosome wrapping states<sup>68</sup>.

### 6.2.2 Quantifying nucleosome wrapping populations by multi-parameter analysis.

To quantify the length of DNA wrapped in the nucleosomes from AFM data, we evaluated the average contour length of the bare DNA molecules in each image (Supplementary Fig. 6.7) and similarly measured the nucleosome arm lengths. By subtracting the combined arm lengths of individual nucleosomes from the mean contour length of bare DNA molecules, we obtain the wrapped length, *i.e.* the length of DNA confined in the nucleosome core particle. Simultaneously, we obtain the opening angle between the DNA segments entering the nucleosome particle for each nucleosome. The 2D distribution of nucleosome opening angles and nucleosome wrapping provides a quantitative view of the nucleosome wrapping

landscape<sup>112</sup> (Fig. 6.2). For a representative data set of canonical nucleosomes, the 2D kernel density distribution reveals two major populations (Fig. 6.2a): One that features wrapped lengths >150 bp and opening angles <100° and one that features wrapped lengths <150 bp and opening angles >70°. We have previously identified<sup>112</sup> the population of nucleosomes with wrapped lengths <150 bp as partially unwrapped. This population features a negative correlation between opening angle and wrapped length, since the opening angle increases by further unwrapping of the DNA arms. Similarly, we have previously assigned the remaining population with wrapping of >150 bp of DNA to fully wrapped nucleosomes. Previous simulations of nucleosomes in AFM imaging<sup>112</sup> rationalize why the apparent wrapped lengths for fully wrapped nucleosomes exceed the 147 bp expected from the crystal structure: the DNA arms that leave the nucleosome entry/exit site overlap close to the nucleosome core particle. In the images, the crossing DNA strands lead to an underestimation of the length of the DNA arms, resulting in longer apparent wrapped lengths for fully wrapped nucleosomes. Utilizing the local minimum seen in the principal component analysis (PCA) of nucleosome core volumes and opening angles (Fig. 6.2a, inset), we separated fully wrapped and partially unwrapped nucleosomes (white and black dots respectively) and find that in this particular data set of unmodified nucleosomes, 31% of the nucleosomes are fully wrapped and 69% of the nucleosomes are partially unwrapped.

To quantitatively investigate nucleosome unwrapping, we fitted the distribution of partially unwrapped nucleosomes with seven 2D Gaussians –one Gaussian per 5 bp unwrapping step up to an unwrapping of 35 bp– located at fixed distances and corresponding to the 5 bp unwrapping periodicity (Fig. 6.2b). The amplitudes of the Gaussians represent the occupancies of the individual states of unwrapping and show that for unmodified nucleosomes most of the partially unwrapped nucleosomes unwrap 25 to 35 bp of DNA. To quantify how reproducibly our analysis pipeline can determine the wrapping populations, we performed independent repeat measurements –all from independent nucleosome reconstitutions and two protein batches– and applied the same analysis pipeline to the separate data sets to obtain mean wrapping distributions and errors. Each repeat comprises >1000 individual nucleosome molecules. Our method is highly reproducible and yields very precise estimates of the individual wrapping populations: the average absolute SEM for the populations is ~1%. Therefore, our analysis pipeline provides a highly accurate and quantitative assay to investigate the effect of epigenetic modifications on nucleosome structure.

### 6.2.3 Post-translational modifications alter wrapping of H3K36me3 nucleosomes.

To study how post-translational histone tail modifications affect nucleosome wrapping on the single-molecule level, we applied our analysis pipeline to two nucleosome constructs that have PTMs close to the DNA entry/exit region, H3K36me3 and H4K5/8/12/16ac, and one nucleosome construct that has a PTM further outside of the nucleosome core particle at the end of the histone H3 tails: H3S10phos (Fig. 6.3). As for the unmodified nucleosomes, we performed 4-5 independent repeat measurements from independent nucleosome reconstitutions and two protein

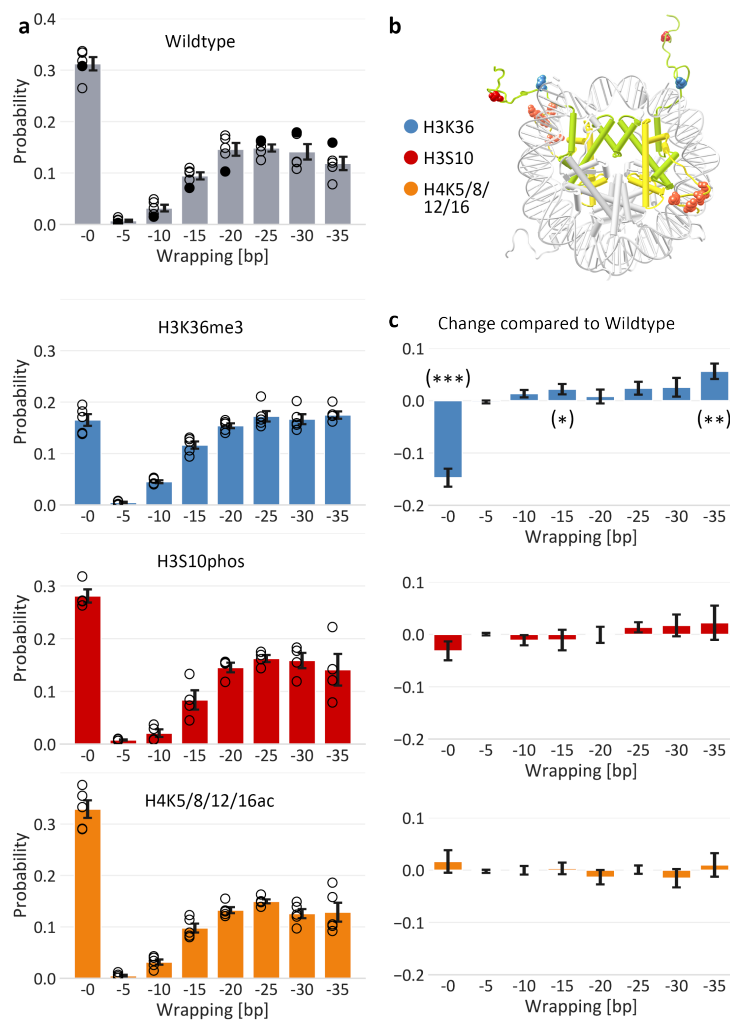


**Figure 6.3: DNA wrapping populations of post-translationally modified nucleosomes.** **a**, Populations of DNA wrapping conformations for unmodified nucleosomes and the three modified nucleosome constructs containing either three methylations at histone H3 lysine 36, a phosphorylation at histone H3 serine 10 or acetylations at histone H4 lysines 5, 8, 12 and 16. The populations were determined from high-throughput analysis of AFM images as shown in Fig. 6.2; the filled black circles in panel **a** are from the data set in Fig. 6.2. For each histone variant four to five independent measurement repeats were obtained; circles indicate the populations of the individual data sets; bars and error bars are the mean and SEM from the independent repeats. **b**, Crystal structure of the canonical nucleosome (PDB 1KX5). Colored spheres represent the positions of the modified histone tail amino acids. **c**, Differences between the wrapping populations of the modified nucleosomes and the unmodified nucleosomes. Significant differences –as determined from two-sample t-tests– are indicated by stars.

batches all measured on different days for each nucleosome variant.

For H3K36me3 nucleosomes, i.e. nucleosomes with three methyl moieties on the epsilon amino group of lysine residue 36 of the histone H3 tails, we find that only a small fraction populates the fully wrapped state ( $16.5\% \pm 1.1\%$ ; mean + SEM from five biological repeats compared to  $31.2\% \pm 1.3\%$  for canonical nucleosomes, Fig. 6.3a) and the vast majority of nucleosomes populates states of partial unwrapping ( $83.5\% \pm 1.1\%$ ). H3K36me3 nucleosomes are almost two fold less likely to occupy the fully wrapped state compared to canonical nucleosomes and are significantly more likely ( $p = 0.005$  from a two-sample t-test) to populate states of higher unwrapping at  $-35\text{bp}$  (Fig. 6.3c). Thus, trimethylation at H3K36 alters nucleosome structure towards increased unwrapping. Previous FRET studies did not find a measurable difference in nucleosome unwrapping between H3K36me3 and canonical nucleosomes<sup>205;206</sup>. However, these studies rely on the binding of the repressor protein LexA to the partially unwrapped nucleosomes between base pairs 8 and 27 and thus require a change in the states of unwrapping  $>25\text{bp}$  to detect differences between H3K36me3 and canonical nucleosomes. Our data show that only part of the additionally unwrapped H3K36me3 nucleosomes populate these states of higher unwrapping and thus the overall increased unwrapping might not be detected by the FRET/LexA methodology at the same level of detail as in our assay.

For H3S10phos nucleosomes, *i.e.* nucleosomes with phosphorylated histone tails at serine residue 10, we find no significant differences in partial unwrapping compared to canonical nucleosomes (two-sample t-test  $p = 0.13$ ).  $28.1\% \pm 1.3\%$  of the phosphorylated nucleosomes are fully wrapped and  $71.9\% \pm 1.3\%$  are partially unwrapped. Phosphorylation introduces negative charge to the serine and thus affects the electrostatic potential of the N-terminal histone tail. However, the modified serine lies on the outer end of the histone tail (Fig. 6.3b) and therefore H3S10phos appears to have only a small effect on the intrinsic nucleosome structure, in line with a previous study that suggested that H3S10phos does not merely act by creating an open chromatin configuration in which DNA is more accessible to the transcriptional machinery<sup>213;214</sup>.

For H4K5/8/12/16ac nucleosomes, *i.e.* nucleosomes with acetylated histone H4 tails at lysine residues 5, 8, 12 and 16, we find  $32.9\% \pm 1.7\%$  of the nucleosomes to occupy the fully wrapped state.  $67.1\% \pm 1.7\%$  occupy states of partial unwrapping with most of them unwrapping 20 to 35 bp of DNA (Fig. 3a), corresponding to no significant differences in wrapping between the tetraacetylated and canonical nucleosomes ( $p = 0.46$ ; Fig. 6.3c). Histone tail acetylations neutralize the positive charge of the modified lysines and thus reduce electrostatic interactions between the histone tails and the negatively charged DNA. Our observation for H4K5/8/12/16ac nucleosomes is in agreement with a recent single-molecule study that found no increased unwrapping for nucleosomes that contained 12 – so three-fold more than in our construct – H4 tail lysine acetylation mimics<sup>207</sup>. Similarly, a FRET study found no effect of H4 acetylations on DNA entry/exit site geometry at ionic conditions same as ours<sup>215</sup>. We speculate that hydrogen bonding and hydrophobic forces outweigh electrostatic interactions in the binding between histone H4 tail lysines 5, 8, 12 and 16 and DNA as proposed for H4K16 in a previous simulation study on the effect of H4K16ac on the histone-DNA binding affinity<sup>216</sup>.

#### 6.2.4 Post-translational modifications can affect nucleosome unwrapping pathways.

Previous studies based on single-molecule manipulation, FRET<sup>69</sup>, and cryo-EM<sup>68</sup> revealed that unwrapping at one exit site stabilizes binding at the second exit site, leading the anti-cooperative unwrapping of DNA from nucleosomes. We have recently shown that by analyzing the distribution of short arm lengths vs. opening angles, our high-throughput AFM image analysis approach is sensitive enough to detect this anti-cooperative unwrapping of canonical nucleosomes<sup>112</sup>. In our data, the anti-cooperative opening of nucleosomes becomes apparent for the nucleosomes at opening angles  $>80^\circ$ , *i.e.* in the regime of partially unwrapped nucleosomes (Fig. 6.4a). The distribution of partially unwrapped nucleosomes splits into two branches reflecting the anti-cooperative nature of the unwrapping process<sup>112</sup>.

To investigate the effect of epigenetic modifications on the cooperativity of nucleosome unwrapping, we calculate the probability of a certain nucleosome type to unwrap anti-cooperatively (Supplementary Fig. 6.8). For this purpose, we define an area in the 2D opening angle vs. short arm length density distribution (Fig. a6.4 and Supplementary Fig. 6.8) in which the nucleosomes are expected to lie in the case of anti-cooperative unwrapping and compare the population size to the fraction of nu-

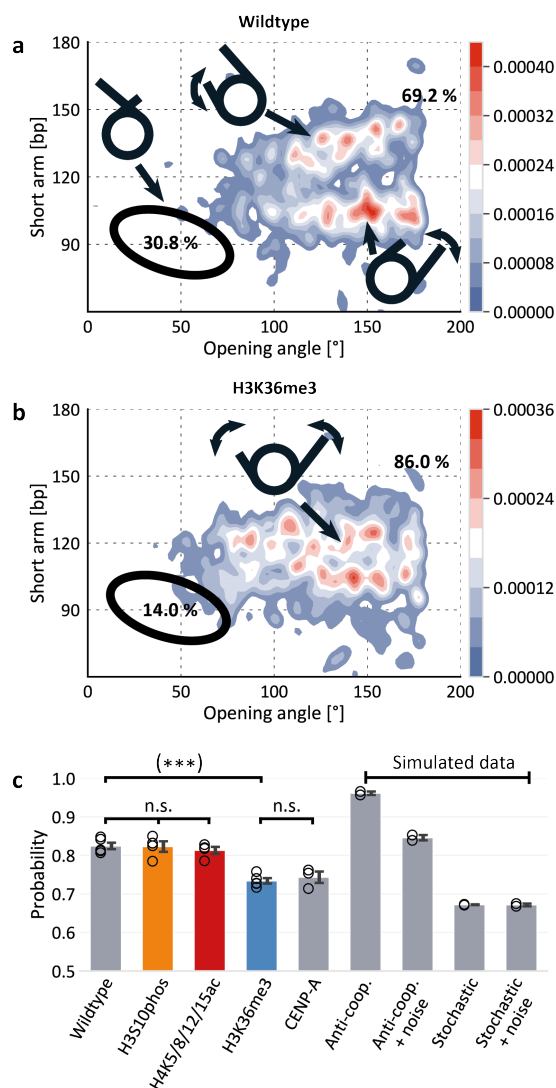


**Figure 6.4:** Unwrapping pathways of post-translationally modified nucleosomes. **a**, 2D kernel density profile (bandwidth = 2.5°, 2.5 bp) of short arm length and opening angle for H3 nucleosomes. A bimodal distribution for opening angles  $>80^\circ$  is apparent, consistent with anti-cooperative unwrapping of the nucleosome core particle ( $N = 1035$ ). The distribution of fully wrapped nucleosomes (30.8 % of all nucleosomes, indicated by the black ellipse) was omitted from the plot for clarity. **b**, 2D kernel density profile (bandwidth = 2.5°, 2.5 bp) of short arm length and opening angle for H3K36me3 nucleosomes ( $N = 1155$ ). **c**, Quantification of the tendency of the different epigenetically modified nucleosomes to unwrap anti-cooperatively or not (Supplementary Fig. 6.8). Unmodified, H3S10phos, and H4K5/8/12/15ac nucleosomes show similar high levels of anti-cooperative unwrapping; in contrast, H3K36me3 and CENP-A nucleosomes unwrap less anti-cooperatively.

cleosomes outside that area. For the canonical nucleosomes,  $82.5\% \pm 0.8\%$  (mean + SEM from five biological repeats) are in the anti-cooperative unwrapping regime. Similarly, the H3S10phos and the H4K5/8/12/16ac nucleosomes occupy the anti-cooperative unwrapping regime at  $82.3\% \pm 1.4\%$  and at  $81.3\% \pm 0.9\%$  respectively (Fig. 6.4c), indicating that these modifications do not affect the anti-cooperativity in nucleosome unwrapping.

In contrast, we find a significant reduction in anti-cooperativity for the unwrapping of H3K36me3 ( $73.4\% \pm 0.7\%$ ) compared to the canonical nucleosomes (two-sample t-test  $p = 3.5 \times 10^{-5}$ ), implying that a substantial part of H3K36me3 unwraps stochastically from both sides. Previously, we have observed a similar effect<sup>112</sup> for nucleosomes that contained the histone H3 variant CENP-A (Fig. 6.4c). We have speculated that the shortened N-terminal alpha helix ( $\alpha N$ ) of CENP-A nucleosomes –compared to the larger H3  $\alpha N$  of canonical nucleosomes– might cause the loss of anti-cooperativity, in line with a previous cryo-EM study that has suggested that allosteric changes involving H3  $\alpha N$  might invoke anti-cooperative unwrapping in canonical nucleosomes<sup>68</sup>. Comparing our findings for H3K36me3 nucleosomes to the CENP-A data from the previous study shows similar reduction of anti-cooperativity (Fig. 6.4b) for both nucleosome types. Both exchange

of H3 with CENP-A and trimethylation at H3K36 introduce changes to the histone octamer at the entry/exit region of the DNA and a reduced fraction of fully wrapped nucleosomes. Our finding of reduced anti-cooperativity in the unwrapping of H3K36me3 nucleosomes indicates that already subtle changes at the DNA entry/exit site of nucleosomes can strongly affect nucleosomal dynamics and opening pathways. To check whether differences in nucleosome positioning along the W601 sequence between unmodified and H3K36me3 nucleosomes plays a role in the different density distribution of H3K36me3 nucleosomes, we compared the positioning of both unmodified and trimethylated nucleosomes but found no differences (Supplementary Fig. 6.9).

To further understand the nature and extent of anti-cooperative unwrapping, we simulated synthetic AFM images of nucleosomes that explored two extreme scenarios: either exhibiting only anti-cooperative unwrapping or completely stochastic unwrapping (Supplementary Fig. 6.10). In short, we placed a disk, representing the nucleosome core particle, on a surface and simulated protruding DNA arms with different lengths at opening angles as deduced from the unwrapping state and the nucleosome crystal structure. The populations of unwrapping simulated are based on the experimentally determined unwrapping populations for unmodified nucleosomes (see Methods and Supplementary Fig. 6.10 for more detail).

Applying our analysis pipeline to simulated nucleosome images that exhibit completely anti-cooperative unwrapping and contain no added noise, we find very high scores for anti-cooperative unwrapping, >95%, as expected. This value is higher than what we observe for any of the experimental conditions. However, if we add Gaussian noise with a width of 5 bp, corresponding to approximately one pixel in our AFM images and representative of our imaging noise, to the short arm length, we find anti-cooperativity values of  $84\% \pm 0.7\%$ , which are still slightly higher, but close to the experimentally observed values for canonical, H3S10phos and H4K5/8/12/16ac nucleosomes, suggesting that our data are consistent with these types of nucleosomes exhibiting almost perfectly anti-cooperative unwrapping. Conversely, if we simulate nucleosomes that unwrap randomly from either site, we find anti-cooperativity scores of  $67\% \pm 0.3\%$ , essentially independent of whether noise is added to the images or not due to the already stochastic nature of the distribution (Supplementary Fig. 6.10). The anti-cooperativity scores for the randomly unwrapping simulations are lower than any of the experimentally determined values, but relatively close to values determined for H3K36me3 and CENP-A nucleosome, suggesting that while H3K36me3 and CENP-A unwrap mostly random, they appear to retain some anti-cooperativity.

### 6.3 Discussion

Quantitative assessment of conformations of post-translationally modified nucleosomes is a key to understanding the mode of operation of the histone code. PTMs can have manifold effects on chromatin structure such as entry site unwrapping, nucleosome destabilization, chromatin fiber destabilization, and histone-histone destabilization<sup>15;197;200</sup>. In this work, we utilized a high-throughput image analysis pipeline to study the effect of the post-translational modifications H3S10phos, H3-K36me3 and H4K5/8/12/16 on nucleosome structure and dynamics. From a

multi-parameter analysis of >25,000 nucleosomes, we obtain a comprehensive and quantitative view of the molecular ensembles, which in turn allows us to extract detailed information about nucleosome wrapping with as little as 1 % uncertainty (SEM) for the populations of the individual unwrapping states.

The H3K36me3 modification exhibited the strongest effect on nucleosome wrapping probably due to its location at the DNA entry/exit site of the nucleosome. While we observe partial unwrapping of ~70 % of the canonical nucleosomes ~85 % of H3K36me3 nucleosomes occupied states of partial unwrapping. Strikingly, in stark contrast to the anti-cooperative unwrapping of canonical nucleosomes where unwrapping from one side inhibits unwrapping from the other, H3K36me3 nucleosomes tend to unwrap stochastically from both sides. H3K36me3 acts via recruiting a number of histone PTM binding domains<sup>204</sup> and is associated with DNA repair, alternative splicing, and transcription<sup>15;217</sup>. Work in drosophila suggests that H3K36me3 is enriched in gene bodies, in particular, in the region of transcribed genes distal to the transcription start site<sup>218;219</sup>. The increased proneness of H3K36me3 nucleosomes to partially unwrap suggests that H3K36me3 can directly affect higher order chromatin structure by increasing the heterogeneity of nucleosome-nucleosome contacts as well as the effective nucleosome valency<sup>196</sup>.

On the macromolecular level, histone tails play a key role in the formation of higher-order chromatin structures<sup>55</sup>. Acetylation of the histone tails inhibits the folding of the nucleosome array *in vitro*<sup>187</sup> and elevated histone acetylations increase chromatin accessibility<sup>220</sup> and reduce the clustering of nucleosomes<sup>221</sup> *in vivo*. Additionally, H4 acetylation blocks the interaction between the H4 tail and the acidic patch of adjacent nucleosomes and thus decreases inter-nucleosomal interactions<sup>126</sup>. Yet, on the single-molecule level, we found no significant changes in nucleosome accessibility due to the H4K5/8/12/16ac modification.

Similarly, while we did not see significant changes in nucleosome wrapping for H3S10phos nucleosomes compared to canonical nucleosomes, it has previously been shown that, in principle, phosphorylation can have significant effects on nucleosome dynamics<sup>129</sup>. However, in these studies the phosphorylation occurred closer to the nucleosome dyad as compared to the phosphorylation investigated in our study that lies towards the end of the histone H3 tails. We speculate that H3S10phos predominantly acts by binding proteins such as certain members of the 14-3-3 family with H3S10phos specificity<sup>222;223</sup> and also via cross-talk with other PTMs such as blocking of H3K9ac<sup>224;225</sup> or promotion of H3K14ac<sup>226</sup>.

Our results highlight how different PTMs involved in transcriptionally active chromatin act through a range of mechanisms. We show that our high-throughput, high-resolution pipeline can reveal the effects of subtle chemical modifications on nucleosome conformations. More broadly, our approach is readily applicable to other nucleosome modifications and variants as well as their interactions with binding partners.

### Author contributions

All authors designed research. S.F.K. performed research, analyzed data, and wrote the manuscript with input from all authors.

### **Acknowledgement**

We thank Philipp Korber and Felix Müller-Planitz for help with initial nucleosome reconstitutions, Pauline Kolbeck, Tine Brouns, Wout Frederickx, Herlinde De Keersmaecker, Steven De Feyter, and Björn H. Menze for discussions and assistance with AFM imaging, and Thomas Nicolaus for help with sample preparation. This work was funded by the Deutsche Forschungsgemeinschaft (DFG, German Research Foundation) through SFB863 – Project ID 111166240 (A11).

## 6.4 Methods

**DNA purification and nucleosome reconstitution.** DNA was PCR amplified from a GeneArt High-Q String DNA fragment (Thermo Fisher Scientific, Waltham, Massachusetts) containing the Widom 601 positioning sequence. The DNA was purified using a QIAquick PCR purification kit (Qiagen, Hilden, Germany) and subsequently eluted to a volume of 30  $\mu$ L in milliQ water. Unmodified and modified histone proteins were purchased from EpiCypher (Durham, North Carolina). Nucleosome reconstitutions were performed by salt gradient dialysis<sup>149</sup>. The dialysis chambers contained 0.65  $\mu$ g of the histone octamers and 3  $\mu$ g of the 486 bp DNA at 2 M NaCl and were placed in one liter of high-salt buffer (2 M NaCl, 10 mM Tris, 1 mM EDTA). Over the course of 15 hours, three liters of low-salt buffer (50 mM NaCl, 10 mM Tris, 1 mM EDTA) were transferred to the high-salt buffer at 4°C. Finally, the dialysis chambers were moved to one liter of low-salt buffer for three hours.

**AFM sample preparation and imaging.** Poly-L-lysine coated mica was prepared by depositing 20  $\mu$ L poly-L-lysine (0.01 % w/v) on freshly cleaved muscovite mica for 30 seconds and subsequently rinsing the surface with 50 mL of milliQ water before drying with a gentle stream of filtered N<sub>2</sub> gas. A sample mix containing bare DNA and reconstituted nucleosomes – usually 30 % to 50 % of the DNA strands do not bind to histones – was incubated at 200 mM NaCl and 10 mM Tris-HCl, pH 7.6, for all measurements for 1 min on ice. The sample mix is then deposited on the poly-L-lysine coated muscovite mica for 30 seconds and subsequently rinsed with 20 mL milliQ water before drying with a gentle stream of filtered N<sub>2</sub> gas.

We used two different commercial AFM instruments for imaging. All AFM images were acquired in tapping mode at room temperature. One set of images was acquired on a Multimode VIII AFM (Bruker) using silicon tips (AC160TS, drive frequency of 300-350 kHz, tip radius 7 nm, Olympus, Tokyo, Japan). Images were scanned over a field of view of 3  $\mu$ m x 3  $\mu$ m at 2048 x 2048 pixels with a scanning speed of 1 Hz. Independent measurement repeats were performed on a Nanowizard Ultraspeed 2 (JPK, Berlin, Germany) with silicon tips (FASTSCAN-A, drive frequency 1400 kHz, tip radius 5 nm, Bruker, Billerica, Massachusetts). Here, images were scanned over a field of view of 6  $\mu$ m x 6  $\mu$ m at 4096 x 4096 pixels with a scanning speed of 1.5 Hz or over a field of view of 12  $\mu$ m x 12  $\mu$ m at 8192 x 8192 pixels at 1.5 Hz (Fig. 6.1b). For each nucleosome type, four independent data sets were recorded with samples from separate nucleosome reconstitutions deposited on new muscovite mica.

**AFM image analysis.** To analyze the flattened AFM images we used an analysis pipeline based in parts on the previously published, open source automated image analysis pipeline<sup>112</sup>. In short, image analysis consists of three steps. First, molecules are detected and classified. For molecule detection, a Gaussian filter and a background subtraction are applied to the flattened AFM images and subsequently a skeletonization<sup>165</sup> – an algorithm that narrows down the objects to a one pixel wide backbone – is performed (Supplementary Fig. 6.5). The skeleton of the molecules is used for classification: Bare DNA has exactly two endpoints in its skeleton and nucleosomes have exactly two endpoints and two branchpoints – points with more

than two neighbors (Supplementary Fig. 6.5). Second, a deconvolution is applied (see below). Third, the classified molecules are analyzed with respect to the structure parameters arm length, volume and opening angle for nucleosomes and length for bare DNA (Supplementary Fig. 6.5). Our AFM analysis code including a detailed installation guide and an example image is available on GITHUB.

**Image deconvolution.** An image deconvolution is applied to the AFM images to trace nucleosomal opening angles and DNA length more accurately (see Fig. 6.5). Before deconvolution can be performed, the tip shape must be estimated. The estimation is done for each AFM image individually since tip shape can vary significantly even for tips of the same batch and it can change while measuring one data set over the course of several hours. To estimate the tip shape, bare DNA strands are traced without deconvolution to obtain an initial trace. Based on this initial trace a grid of 10 pixels ( $\sim 15$  nm) in size is filled by the height values surrounding the initial trace of the DNA strand (Supplementary Fig. 6.6). After repeating this process for all DNA strands in the image and averaging the intensities in the grid, a good estimate of the tip shape is available to apply the deconvolution algorithm. Here, we make use of the Richardson-Lucy deconvolution algorithm<sup>211;212</sup>, an iterative procedure for recovering an underlying image blurred by a known point spread function, *i.e.* the tip shape.

**AFM image simulations.** To simulate nucleosome images with different levels of anti-cooperative unwrapping, an 11 nm diameter disk of uniform height together with protruding DNA arms based on the worm-like chain model at opening angles deduced from the nucleosome crystal structure (PDB 1KX5) was placed on a flat surface. The fully wrapped lengths of the short and long arm comprise 106 bp and 233 bp, respectively, and lengths were increased in 5 bp steps to simulate the individual unwrapping steps up to 35 bp. The simulated populations for each unwrapping state were chosen based on the experimentally determined populations. For simulation of anti-cooperative unwrapping, the length of only one arm was increased while keeping the length of the other arm constant. For simulation of stochastic unwrapping, the arms were randomly unwrapped in 5 bp steps up to the total amount of unwrapping simulated for each state. For example, when simulating a state of 10 bp unwrapped, possible lengths for the short arm are [106, 111, 116] bp and [233, 238, 243] bp for the long arm and were assigned randomly for each simulated nucleosome while keeping the total of 10 bp unwrapped between the two arms constant. Consecutively, the DNA arms were dilated to their expected width of 2 nm and random noise in combination with a Gaussian filter ( $\sigma = 2$  nm) were applied to mimic the effect of tip convolution.

## 6.5 Supplementary information

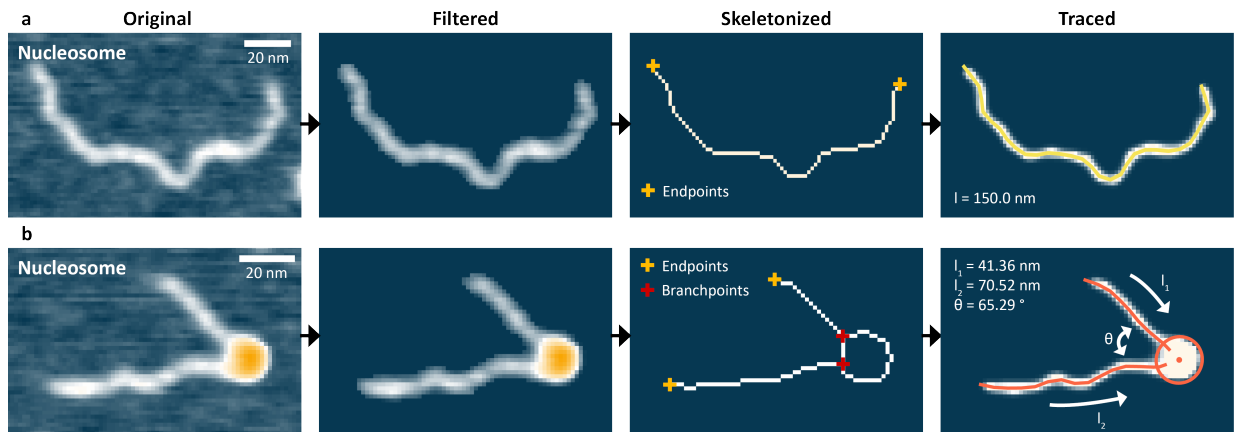


**Figure 6.5: Tracing of bare DNA and nucleosomes.** **a**, AFM topographic image of a bare DNA strand with the different tracing steps visualized. At first, the original image is filtered by applying a Gaussian filter and removing the background with a fixed threshold value. Subsequently, the filtered image is skeletonized. The skeletonized backbone of the molecules serves as the basis for classification: whereas the skeleton of bare DNA has exactly two endpoints and no branchpoints – points that have more than two neighbors – the skeleton of nucleosomes contains exactly two endpoints and two branchpoints. Finally, the bare DNA molecule is traced with regards to its length after applying a deconvolution. **b**, AFM topographic image of a nucleosome with the different tracing steps involved. After initial filtering, the molecule is skeletonized for classification. Finally, the nucleosome is traced with regards to the arm lengths, the opening angle and the volume.

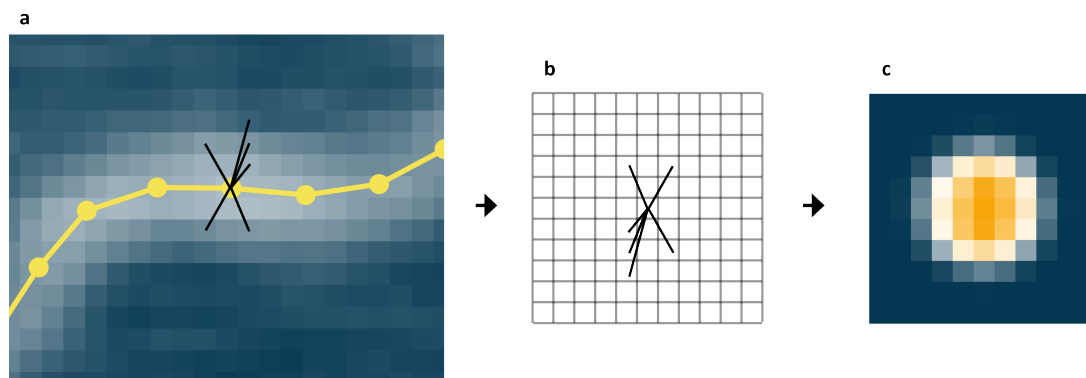


**Figure 6.6: Tip shape estimation.** **a**, Tip shape estimation is based on analysis of the bare DNA images present in each AFM field of view. In the first step of tip shape estimation, the vectors between the pixel centers and the nearest trace point are computed. The trace points are obtained by first tracing the DNA strand without deconvolution to get an estimate of the trace. After obtaining the tip shape and applying deconvolution, the DNA strands are traced again. All pixels that are within a maximum range of 6 nm towards the next trace point are taken into account. The amount of initial trace points was reduced for clarity in the graph. During application, the trace is approximated by a spline interpolation to provide more trace points and thus reduce error in estimating the tip shape due to a too coarse grained trace. **b**, The vectors are then brought into an empty 2D grid and the measured height values of the pixels the vectors were obtained from in panel **a** are added to the grid. Repeating the process for multiple DNA strands (typically 100-200 DNA strands per image) will result in tens of thousands height values of vectors to fill the 2D grid with. **c**, After adding up all height values of the vectors in the grid, the grid pixels are normalized based on the number of values added per grid pixel. The resulting distribution is an approximation of the tip shape that was used in imaging the respective image.

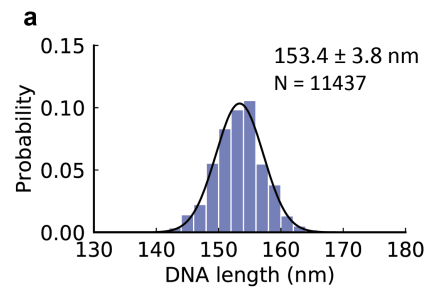


**Figure 6.7: Bare DNA lengths.** a, Histogram of bare DNA lengths combined for all data sets used in this work. We find a contour length of  $l_c = 153.4 \pm 3.9$  nm (mean  $\pm$  std from 11437 molecules) corresponding to a length per bp of  $0.316 \pm 0.008$  nm, in agreement with previous measurements by AFM<sup>166;210</sup> and solution X-ray scattering<sup>167</sup>.

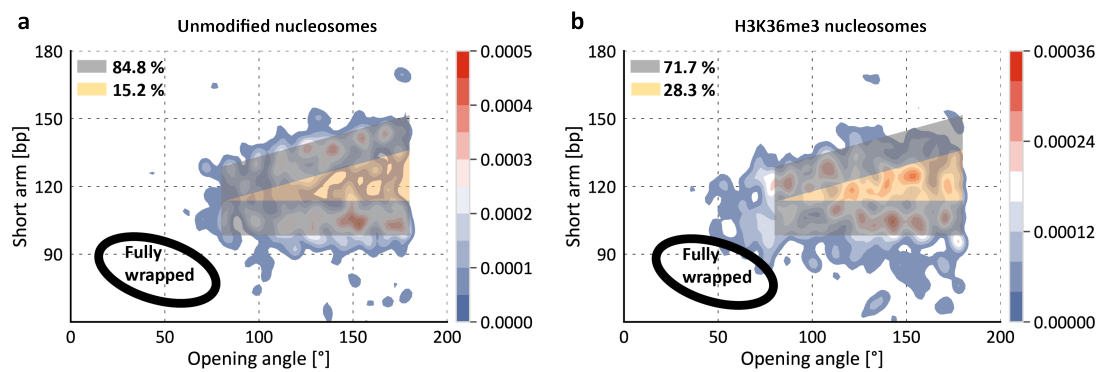


**Figure 6.8: Quantification of anti-cooperative unwrapping.** **a**, 2D kernel density profile (bandwidth =  $2.5^\circ$ , 2.5 bp) of short arm length and opening angle for partially unwrapped canonical nucleosomes ( $N = 1035$ ). Nucleosomes that unwrap anti-cooperatively, i.e. with either the long arm or the short arm unwrapping, are expected in the dark area. Nucleosomes that unwrap from both sides simultaneously are expected in the yellow area. For this particular data set of canonical nucleosomes, 84.8 % of the nucleosomes are in the regime of anti-cooperative unwrapping and 15.2 % in the regime of stochastic unwrapping. The values obtained in this analysis serve as basis for the quantification of anti-cooperativity in Fig. 4c of the main text. Per definition, the dark area makes up 75 % of the total area and the yellow area makes up 25 % of the total area. The black ellipse indicates the position of fully wrapped nucleosomes that are omitted for clarity. **b**, 2D kernel density profile (bandwidth =  $2.5^\circ$ , 2.5 bp) of short arm length and opening angle for partially unwrapped H3K36me3 nucleosomes ( $N = 1155$ ). 71.7 % of the nucleosomes are in the regime of anti-cooperative unwrapping and 28.3 % in the regime of stochastic unwrapping.

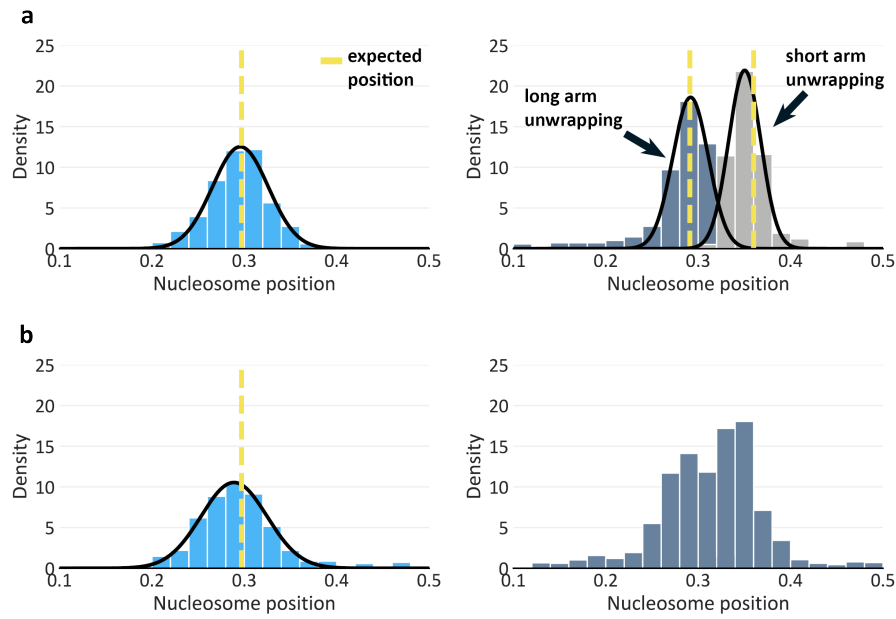


**Figure 6.9: Nucleosome positioning.** **a**, Nucleosome positioning for a sample data set of unmodified nucleosomes ( $N = 1300$ ). The nucleosome position is calculated by dividing the short arm length by the sum of short arm and long arm length. The plots show that both fully wrapped and partially unwrapped nucleosomes are positioned well at the Widom positioning sequence. **b**, Nucleosome positioning for a sample data set of H3K36me3 nucleosomes ( $N = 1732$ ). Similarly to the unmodified nucleosomes, the H3K36me3 nucleosomes are positioned well. Due to the stochastic unwrapping of H3K36me3 nucleosomes it is not possible to separate the partially unwrapped nucleosomes (right histogram) into nucleosomes that solely unwrap from the short arm and those that unwrap solely from the long arm.

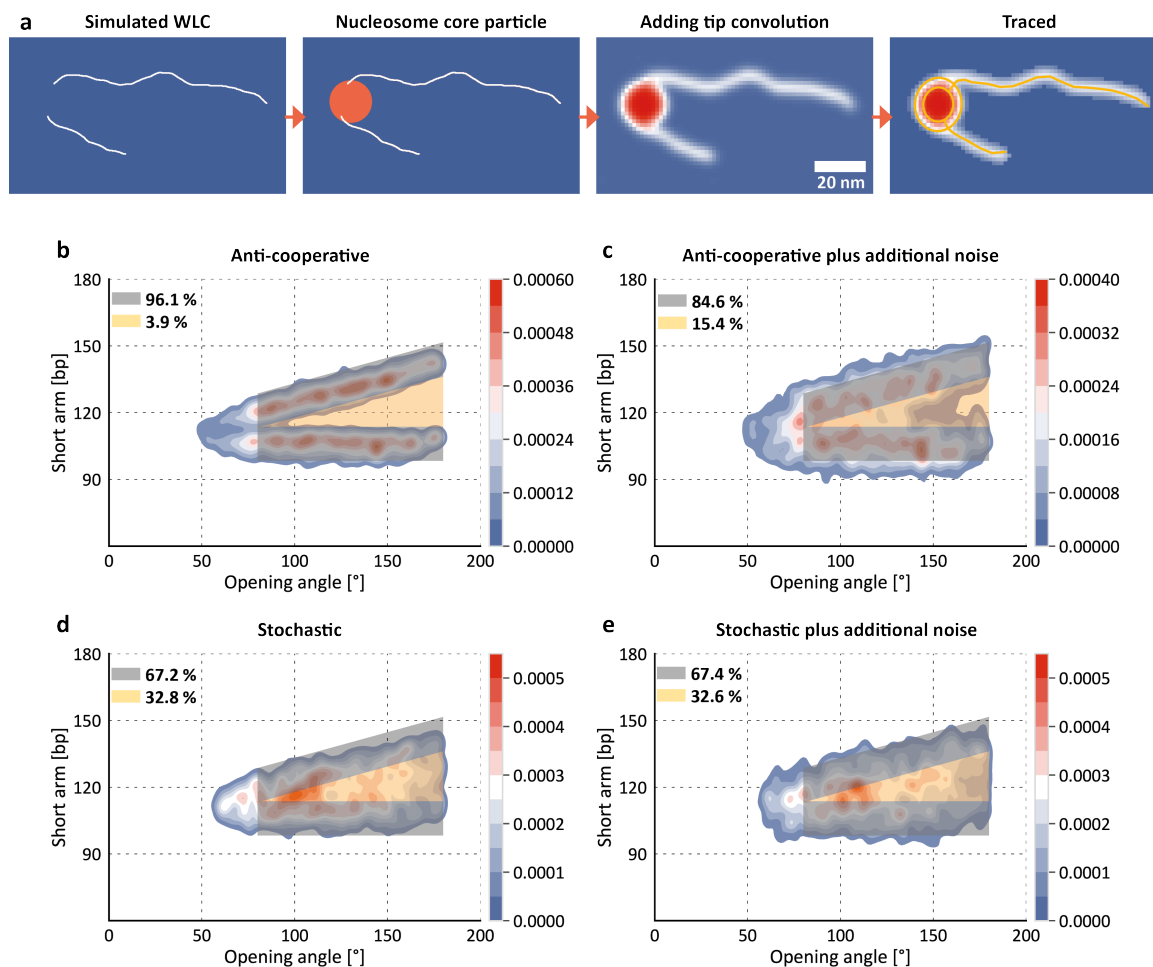


**Figure 6.10: Simulation of anti-cooperative and stochastic unwrapping.** **a**, Simulation of nucleosomes consisted of placing a nucleosomal disk and simulating protruding DNA arms. The position and initial directionality of the protruding DNA arms was deduced from the nucleosome crystal structure (PDB 1KX5). The lengths of the DNA arms are 106 bp for the short arm and 233 bp for the long arm initially and are varied based on the state of unwrapping that is simulated (see Methods). Consecutively, the DNA was diluted to its expected width of 2 nm and a Gaussian filter was applied to mimic the effect of tip convolution. Finally, the synthetic AFM image is traced with our automated image analysis pipeline. **b**, 2D Kernel density plot for simulated nucleosomes ( $N = 2072$ ). To simulate anti-cooperative unwrapping, the length of either the short or the long arm was always kept constant (106 bp or 233 bp for the short and the long arm respectively) and the length of the other arm was increased in 5 bp steps up to a maximum unwrapping of 35 bp. Unwrapping is simulated to occur from each arm in 50 % of the cases and the sizes of the individual unwrapping populations are based on the probability for each population as experimentally measured for unmodified nucleosomes (Figure 6.3a). **c**, 2D Kernel density plot for simulated nucleosomes ( $N = 2072$ ). The plot comprises the same nucleosomes as shown in **b**. However, additional Gaussian distributed noise with  $\sigma = 5$  bp was added to the short arm length to better capture expected imaging errors that might occur during experiments. **d**, 2D Kernel density plot for simulated nucleosomes ( $N = 1469$ ). Compared to the anti-cooperative unwrapping of plots **b** and **c**, this plot shows nucleosomes that unwrap stochastically. To simulate stochastic unwrapping, the length of both arms was randomly increased in 5 bp steps for the individual unwrapping steps. For example, for simulation of states of partial unwrapping of 10 bp in total, the length of the short and long arm was randomly either increased by [+0, +10], [+5, +5] or [+10, +0] respectively. This procedure was again repeated up to a maximum unwrapping of 35 bp in total. **e**, 2D Kernel density plot for simulated nucleosomes ( $N = 1469$ ). The plot comprises the same nucleosomes as shown in **d**. Similar to **c**, additional Gaussian noise with  $\sigma = 5$  bp was added to the short arm length to better capture imaging errors that might occur during experiments.

# 7

## Conclusion

Over the past few decades, manifold techniques have been developed that allow for exceptionally detailed and highly resolved studies of DNA and nucleo-protein complexes. The initial goal of this thesis was the development of a robust and high-throughput analysis pipeline to take AFM studies of nucleo-protein complexes and of nucleosomes in particular to the next level. With the development of an AFM image analysis pipeline, I was able to establish a framework that allows for readily reproducible studies of DNA and nucleosomes, hereby mostly removing the user bias of manual data analysis and enabling the analysis of larger data sets as compared to what is commonly worked with in AFM imaging studies up to date. The validity of the pipeline was then proven by achieving insights into the unwrapping landscape of wild type nucleosomes - such as the anti-cooperativity of partial nucleosome opening - in unprecedented detail compared to previous AFM studies and in line with previous work on nucleosomes.

Having established and validated this valuable analytical tool, we were then able to gain additional insights into the unwrapping dynamics of wild type nucleosomes, hereby discovering the slightly preferential unwrapping from the stiffer DNA side without force as compared to previous force-induced observations that saw highly preferential opening from the stiffer side. Along that work, we also found significant differences in wrapping between CENP-A and wild type nucleosomes, and later, for nucleosomes containing subtle epigenetic modifications with the main result being the altered unwrapping dynamics of CENP-A and H3K36me3 nucleosomes: In stark contrast to wild type nucleosomes that unwrap anti-cooperatively from only one side at the same time, we observed that CENP-A and H3K36me3 nucleosomes can unwrap from both sides simultaneously. Understanding these subtle dynamic differences for a multitude of nucleosome variants will help in understanding the mode of action and the role in regulating gene activity and silencing of the respective modifications.

## Perspectives

While I was able to tackle and answer a lot of the initial open questions of this work, as so often in research, even more questions popped up along the way. The establishment of the automated analysis pipeline will allow for manifold detailed studies of nucleo-protein and nucleosome systems that have not been investigated at this level of detail on the single-molecule level yet. For example, almost all single-molecule studies of mono-nucleosomes utilize the Widom 601 positioning sequence to reliably reconstitute and position the histone octamer along the DNA construct. However, the W601 positioning sequence is an artificial sequence that does not resemble the landscape of DNA sequences present in the genome. Studying the wrapping landscape and the positioning of mono-nucleosomes on other DNA sequences such as different nucleosome positioning sequences, highly repetitive alpha-satellite DNA or on random DNA sequences might provide interesting insights into the role of DNA wrapping for transcriptional activation and can be easily achieved with the workflow and method developed in this thesis.

Similarly, the analysis framework could be expanded to poly-nucleosomes and larger nucleosome constructs to better understand the interplay between consecutive nucleosomes along a DNA strand. Does the wrapping/unwrapping of one nucleosome affect the wrapping of consecutive nucleosomes in a significant manner? What role does the crosstalk between epigenetic modifications of the individual nucleosomes in nucleosome arrays play and how does it affect the nucleosomal unwrapping pathways? Especially for poly-nucleosomes, these questions have not really been tackled by any technique so far and the framework presented here would provide a powerful tool to study these systems of interest.

Certainly, when working on these and other questions in future work, even more problems and open questions will arise and hopefully some day be answered by resourceful researchers, expanding our knowledge bit by bit within the ocean of what we do not know or understand yet.

## Bibliography

- [1] Ronald C. Kessler and Evelyn J. Bromet. The epidemiology of depression across cultures. *Annual Review of Public Health*, 34:119–138, 2013. ISSN 01637525. doi: [10.1146/annurev-publhealth-031912-114409](https://doi.org/10.1146/annurev-publhealth-031912-114409).
- [2] WHO. WHO report on cancer: setting priorities, investing wisely and providing care for all, 2020.
- [3] 2020 Alzheimer’s disease facts and figures. *Alzheimer’s and Dementia*, 16(3):391–460, 2020. ISSN 15525279. doi: [10.1002/alz.12068](https://doi.org/10.1002/alz.12068).
- [4] Huda Y. Zoghbi and Arthur L. Beaudet. Epigenetics and human disease. *Cold Spring Harbor Perspectives in Biology*, 8(2):1–28, 2016. ISSN 19430264. doi: [10.1101/cshperspect.a019497](https://doi.org/10.1101/cshperspect.a019497).
- [5] Giacomo Cavalli and Edith Heard. Advances in epigenetics link genetics to the environment and disease. *Nature*, 571(7766):489–499, 2019. ISSN 14764687. doi: [10.1038/s41586-019-1411-0](https://doi.org/10.1038/s41586-019-1411-0).
- [6] Victoria S. Dalton, Erik Kolshus, and Declan M. McLoughlin. Epigenetics and depression: Return of the repressed. *Journal of Affective Disorders*, 155(1):1–12, 2014. ISSN 01650327. doi: [10.1016/j.jad.2013.10.028](https://doi.org/10.1016/j.jad.2013.10.028).
- [7] Adrian Bird. Perceptions of epigenetics. *Nature*, 447(7143):396–398, 2007. ISSN 14764687. doi: [10.1038/nature05913](https://doi.org/10.1038/nature05913).
- [8] Herbert E. Covington, Ian Maze, Quincey C. LaPlant, Vincent F. Vialou, Yoshinori N. Ohnishi, Olivier Berton, Dan M. Fass, William Renthal, Augustus J. Rush, Emma Y. Wu, Subroto Ghose, Vaishnav Krishnan, Scott J. Russo, Carol Tamminga, Stephen J. Haggarty, and Eric J. Nestler. Antidepressant actions of histone deacetylase inhibitors. *Journal of Neuroscience*, 29(37):11451–11460, 2009. ISSN 02706474. doi: [10.1523/JNEUROSCI.1758-09.2009](https://doi.org/10.1523/JNEUROSCI.1758-09.2009).
- [9] Gerda Egger, Gangning Liang, Ana Aparicio, and Jones Peter A. Epigenetics in human disease and prospects for epigenetic therapy. *Nature*, 429(May):246–247, 2004. doi: [10.1038/nature02625](https://doi.org/10.1038/nature02625).
- [10] Aaron D. Goldberg, C. David Allis, and Emily Bernstein. Epigenetics: A Landscape Takes Shape. *Cell*, 128(4):635–638, 2007. ISSN 00928674. doi: [10.1016/j.cell.2007.02.006](https://doi.org/10.1016/j.cell.2007.02.006).
- [11] Andrew P. Feinberg. The Key Role of Epigenetics in Human Disease Prevention and Mitigation. *New England Journal of Medicine*, 378(14):1323–1334, 2018. ISSN 0028-4793. doi: [10.1056/nejmra1402513](https://doi.org/10.1056/nejmra1402513).
- [12] María Berdasco and Manel Esteller. Clinical epigenetics: seizing opportunities for translation. *Nature Reviews Genetics*, 20(2):109–127, 2019. ISSN 14710064. doi: [10.1038/s41576-018-0074-2](https://doi.org/10.1038/s41576-018-0074-2).
- [13] Peter A. Jones, Hitoshi Ohtani, Ankur Chakravarthy, and Daniel D. De Carvalho. Epigenetic therapy in immune-oncology. *Nature Reviews Cancer*, 19(3):151–161, 2019. ISSN 14741768. doi: [10.1038/s41568-019-0109-9](https://doi.org/10.1038/s41568-019-0109-9).
- [14] Nita Ahuja, Anup R. Sharma, and Stephen B. Baylin. Epigenetic therapeutics: A new weapon in the war against cancer. *Annual Review of Medicine*, 67:73–89, 2016. ISSN 1545326X. doi: [10.1146/annurev-med-111314-035900](https://doi.org/10.1146/annurev-med-111314-035900).
- [15] Gregory D. Bowman and Michael G. Poirier. Post-translational modifications of histones that influence nucleosome dynamics. *Chemical Reviews*, 115(6):2274–2295, 2015. ISSN 15206890. doi: [10.1021/cr500350x](https://doi.org/10.1021/cr500350x).

- [16] Beat Fierz and Michael G. Poirier. Biophysics of Chromatin Dynamics. *Annual Review of Biophysics*, 48(1):321–345, 2019. ISSN 1936-122X. doi: [10.1146/annurev-biophys-070317-032847](https://doi.org/10.1146/annurev-biophys-070317-032847).
- [17] G Binnig, H Rohrer, Christoph Gerber, and E Weibel. Surface Studies by Scanning Tunneling Microscopy. *Physical Review Letters*, 49(1):57–60, 1982.
- [18] G Binnig and C F Quate. Atomic Force Microscope. *Physical Review Letters*, 56(9):930–933, apr 1986.
- [19] A. L. Weisenhorn, P. Maivald, H. J. Butt, and P. K. Hansma. Measuring adhesion, attraction, and repulsion between surfaces in liquids with an atomic-force microscope. *Physical Review B*, 45(19):11226–11232, 1992. ISSN 01631829. doi: [10.1103/PhysRevB.45.11226](https://doi.org/10.1103/PhysRevB.45.11226).
- [20] Hang Zhang, Junxiang Huang, Yongwei Wang, Rui Liu, Xiulan Huai, Jingjing Jiang, and Chantelle Anuso. Atomic force microscopy for two-dimensional materials: A tutorial review. *Optics Communications*, 406(March):3–17, 2018. ISSN 00304018. doi: [10.1016/j.optcom.2017.05.015](https://doi.org/10.1016/j.optcom.2017.05.015).
- [21] Helen G. Hansma, Robert L. Sinsheimer, Jay Groppe, Thomas C. Bruice, Virgil Elings, Gus Gurlley, Magdalena Bezanilla, Iris A. Mastrangelo, Paul V.C. Hough, and Paul K. Hansma. Recent advances in atomic force microscopy of DNA. *Scanning*, 15(5):296–299, 1993. ISSN 19328745. doi: [10.1002/sca.4950150509](https://doi.org/10.1002/sca.4950150509).
- [22] Kavit H S Main, James I Provan, Philip J Haynes, Geoffrey Wells, John A Hartley, and Alice L B Pyne. Atomic force microscopy — A tool for structural and translational DNA research Atomic force microscopy — A tool for structural and translational DNA research. *APL Bioengineering*, 5(July), 2021. doi: [10.1063/5.0054294](https://doi.org/10.1063/5.0054294).
- [23] Johannes Schwenk, Sungmin Kim, Julian Berwanger, Fereshte Ghahari, Daniel Walkup, Marlou R. Slot, Son T. Le, William G. Cullen, Steven R. Blankenship, Sasa Vranjkovic, Hans J. Hug, Young Kuk, Franz J. Giessibl, and Joseph A. Stroscio. Achieving  $\mu\text{eV}$  tunneling resolution in an in-operando scanning tunneling microscopy, atomic force microscopy, and magnetotransport system for quantum materials research. *Review of Scientific Instruments*, 91(7), 2020. ISSN 10897623. doi: [10.1063/5.0005320](https://doi.org/10.1063/5.0005320).
- [24] Elena T. Herruzo, Alma P. Perrino, and Ricardo Garcia. Fast nanomechanical spectroscopy of soft matter. *Nature Communications*, 5, 2014. ISSN 20411723. doi: [10.1038/ncomms4126](https://doi.org/10.1038/ncomms4126).
- [25] Bede Pittenger, Natalia Erina, and Chanmin Su. Quantitative Mechanical Property Mapping at the Nanoscale with PeakForce QNM. *Bruker Application Note AN128*, (January), 2010. doi: [10.13140/RG.2.1.4463.8246](https://doi.org/10.13140/RG.2.1.4463.8246).
- [26] Stefan Kaemmer. Introduction to Bruker’s ScanAsyst and PeakForce Tapping AFM Technology. *Bruker Application Note #133*, pages 1–12, 2011.
- [27] Alice Pyne, Agnes Noy, Kavit Main, Victor Velasco-Berrelleza, Michael Piperakis, Lesley Mitchenall, Fiorella Cugliandolo, Joseph Beton, Clare Stevenson, Bart Hoogenboom, Andrew Bates, Anthony Maxwell, and Sarah Harris. Base-pair resolution analysis of the effect of supercoiling on DNA flexibility and major groove recognition by triplex-forming oligonucleotides. *Nature Communications*, pages 1–12, 2019. ISSN 2041-1723. doi: [10.1101/863423](https://doi.org/10.1101/863423).
- [28] Yuri L. Lyubchenko and Luda S. Shlyakhtenko. Imaging of DNA and protein–DNA complexes with atomic force microscopy. *Critical Reviews in Eukaryotic Gene Expression*, 26(1):63–96, 2016. ISSN 10454403. doi: [10.1615/CritRevEukaryotGeneExpr.v26.i1.70](https://doi.org/10.1615/CritRevEukaryotGeneExpr.v26.i1.70).
- [29] F. Zenhausern, M. Adrian, B. Ten Heggeler-Bordier, L. M. Eng, and P. Descouts. DNA and RNA polymerase/DNA complex imaged by scanning force microscopy: Influence of molecular-scale friction. *Scanning*, 14(4):212–217, 1992. ISSN 19328745. doi: [10.1002/sca.4950140405](https://doi.org/10.1002/sca.4950140405).

- [30] H. Bei, E. P. George, J. L. Hay, and G. M. Pharr. Influence of indenter tip geometry on elastic deformation during nanoindentation. *Physical Review Letters*, 95(4):1–4, 2005. ISSN 00319007. doi: [10.1103/PhysRevLett.95.045501](https://doi.org/10.1103/PhysRevLett.95.045501).
- [31] A. T. Winzer, C. Kraft, S. Bhushan, V. Stepanenko, and I. Tessmer. Correcting for AFM tip induced topography convolutions in protein-DNA samples. *Ultramicroscopy*, 121:8–15, 2012. ISSN 03043991. doi: [10.1016/j.ultramic.2012.07.002](https://doi.org/10.1016/j.ultramic.2012.07.002).
- [32] J. S. Villarrubia. Algorithms for scanned probe microscope image simulation, surface reconstruction, and tip estimation. *Journal of Research of the National Institute of Standards and Technology*, 102(4):425–454, 1997. ISSN 1044677X. doi: [10.6028/jres.102.030](https://doi.org/10.6028/jres.102.030).
- [33] L. S. Dongmo, J. S. Villarrubia, S. N. Jones, T. B. Renegar, M. T. Postek, and J. F. Song. Experimental test of blind tip reconstruction for scanning probe microscopy. *Ultramicroscopy*, 85(3):141–153, 2000. ISSN 03043991. doi: [10.1016/S0304-3991\(00\)00051-6](https://doi.org/10.1016/S0304-3991(00)00051-6).
- [34] Erin E. Flater, George E. Zacharakis-Jutz, Braulio G. Dumba, Isaac A. White, and Charles A. Clifford. Towards easy and reliable AFM tip shape determination using blind tip reconstruction. *Ultramicroscopy*, 146:130–143, 2014. ISSN 18792723. doi: [10.1016/j.ultramic.2013.06.022](https://doi.org/10.1016/j.ultramic.2013.06.022).
- [35] U. Hübner, W. Morgenroth, H. G. Meyer, T. Sulzbach, B. Brendel, and W. Mirandé. Downwards to metrology in nanoscale: Determination of the AFM tip shape with well-known sharp-edged calibration structures. *Applied Physics A: Materials Science and Processing*, 76(6):913–917, 2003. ISSN 09478396. doi: [10.1007/s00339-002-1975-6](https://doi.org/10.1007/s00339-002-1975-6).
- [36] Minh Hieu Trinh, Michael Odorico, Laurent Bellanger, Mireille Jacquemond, Pierre Parot, and Jean Luc Pellequer. Tobacco mosaic virus as an AFM tip calibrator. *Journal of Molecular Recognition*, 24(3):503–510, 2011. ISSN 09523499. doi: [10.1002/jmr.1118](https://doi.org/10.1002/jmr.1118).
- [37] Toshio Ando. High-speed AFM imaging. *Current Opinion in Structural Biology*, 28(1):63–68, 2014. ISSN 1879033X. doi: [10.1016/j.sbi.2014.07.011](https://doi.org/10.1016/j.sbi.2014.07.011).
- [38] Georg E. Fantner, Georg Schitter, Johannes H. Kindt, Tzvetan Ivanov, Katarina Ivanova, Rohan Patel, Niels Holten-Andersen, Jonathan Adams, Philipp J. Thurner, Ivo W. Rangelow, and Paul K. Hansma. Components for high speed atomic force microscopy. *Ultramicroscopy*, 106(8-9):881–887, 2006. ISSN 03043991. doi: [10.1016/j.ultramic.2006.01.015](https://doi.org/10.1016/j.ultramic.2006.01.015).
- [39] Yanyan Wang, Xiaodong Hu, Linyan Xu, and Xiaotang Hu. Improving the scanning speed of atomic force microscopy at the scanning range of several tens of micrometers. *Ultramicroscopy*, 124:102–107, 2013. ISSN 03043991. doi: [10.1016/j.ultramic.2012.08.001](https://doi.org/10.1016/j.ultramic.2012.08.001).
- [40] Masashi Kitazawa, Koichi Shiotani, and Akitoshi Toda. Batch fabrication of sharpened silicon nitride tips. *Japanese Journal of Applied Physics, Part 1: Regular Papers and Short Notes and Review Papers*, 42(7 B):4844–4847, 2003. ISSN 00214922. doi: [10.1143/jjap.42.4844](https://doi.org/10.1143/jjap.42.4844).
- [41] Noriyuki Kodera, Mitsuru Sakashita, and Toshio Ando. Dynamic proportional-integral-differential controller for high-speed atomic force microscopy. *Review of Scientific Instruments*, 77(8):083704, 2006. ISSN 0034-6748. doi: [10.1063/1.2336113](https://doi.org/10.1063/1.2336113).
- [42] Noriyuki Kodera, Daisuke Yamamoto, Ryoki Ishikawa, and Toshio Ando. Video imaging of walking myosin v by high-speed atomic force microscopy. *Nature*, 468(7320):72–76, 2010. ISSN 00280836. doi: [10.1038/nature09450](https://doi.org/10.1038/nature09450).
- [43] Toshio Ando, Takayuki Uchihashi, and Noriyuki Kodera. High-speed AFM and applications to biomolecular systems. *Annual Review of Biophysics*, 42(1):393–414, 2013. ISSN 1936122X. doi: [10.1146/annurev-biophys-083012-130324](https://doi.org/10.1146/annurev-biophys-083012-130324).

- [44] Toshio Ando. High-speed atomic force microscopy. *Current Opinion in Chemical Biology*, 51:105–112, 2019. ISSN 18790402. doi: [10.1016/j.cbpa.2019.05.010](https://doi.org/10.1016/j.cbpa.2019.05.010).
- [45] Yves F. Dufrêne, Toshio Ando, Ricardo Garcia, David Alsteens, David Martinez-Martin, Andreas Engel, Christoph Gerber, and Daniel J. Müller. Imaging modes of atomic force microscopy for application in molecular and cell biology. *Nature Nanotechnology*, 12(4):295–307, 2017. ISSN 17483395. doi: [10.1038/nnano.2017.45](https://doi.org/10.1038/nnano.2017.45).
- [46] Daniel J. Müller and Yves F. Dufrêne. Atomic force microscopy: A nanoscopic window on the cell surface. *Trends in Cell Biology*, 21(8):461–469, 2011. ISSN 09628924. doi: [10.1016/j.tcb.2011.04.008](https://doi.org/10.1016/j.tcb.2011.04.008).
- [47] George R. Heath, Ekaterina Kots, Janice L. Robertson, Shifra Lansky, George Khelashvili, Harel Weinstein, and Simon Scheuring. Localization atomic force microscopy. *Nature*, 594(7863):385–390, 2021. ISSN 0028-0836. doi: [10.1038/s41586-021-03551-x](https://doi.org/10.1038/s41586-021-03551-x).
- [48] Bruce Alberts, Alexander Johnson, Julian Lewis, David Morgan, Martin Raff, Keith Roberts, and Peter Walter. *Molecular Biology of the Cell*, volume 6th Editio. 2014. ISBN 9780815344322. doi: [10.1249/mss.0b013e318185ce9d](https://doi.org/10.1249/mss.0b013e318185ce9d).
- [49] Francis S. Collins, Michael Morgan, and Aristides Patrinos. The Human Genome Project: Lessons from large-scale biology. *Science*, 300(5617):286–290, 2003. ISSN 00368075. doi: [10.1126/science.1084564](https://doi.org/10.1126/science.1084564).
- [50] J D Watson and F H C Crick. Molecular structure of nucleic acids. *Nature*, 4356:737–738, 1953. ISSN 14346001. doi: [10.1140/epja/i2001-10240-x](https://doi.org/10.1140/epja/i2001-10240-x).
- [51] Dean R. Hewish and Leigh A. Burgoyne. Chromatin sub-structure. The digestion of chromatin DNA at regularly spaced sites by a nuclear deoxyribonuclease. *Biochemical and Biophysical Research Communications*, 52(2):504–510, 1973. ISSN 10902104. doi: [10.1016/0006-291X\(73\)90740-7](https://doi.org/10.1016/0006-291X(73)90740-7).
- [52] Roger D. Kornberg. Chromatin Structure: A Repeating Unit of Histones and DNA. *Science*, 184:868–871, 1974.
- [53] Steven L. McKnight and Oscar L. Miller. Ultrastructural patterns of RNA synthesis during early embryogenesis of *Drosophila melanogaster*. *Cell*, 8(2):305–319, 1976. ISSN 00928674. doi: [10.1016/0092-8674\(76\)90014-3](https://doi.org/10.1016/0092-8674(76)90014-3).
- [54] Roger D Kornberg. Structure of Chromatin. *Annu*, 46:931–954, 1977.
- [55] Sandro Baldi, Philipp Korber, and Peter B Becker. Beads on a string—nucleosome array arrangements and folding of the chromatin fiber. *Nature Structural & Molecular Biology*, 27(2):109–118, 2020. ISSN 1545-9985. doi: [10.1038/s41594-019-0368-x](https://doi.org/10.1038/s41594-019-0368-x).
- [56] Dmitry V. Fyodorov, Bing Rui Zhou, Arthur I. Skoultchi, and Yawen Bai. Emerging roles of linker histones in regulating chromatin structure and function. *Nature Reviews Molecular Cell Biology*, 19:192–206, 2018. ISSN 14710080. doi: [10.1038/nrm.2017.94](https://doi.org/10.1038/nrm.2017.94).
- [57] Kazuhiro Maeshima, Ryan Rogge, Sachiko Tamura, Yasumasa Joti, Takaaki Hikima, Heather Szerlong, Christine Krause, Jake Herman, Erik Seidel, Jennifer DeLuca, Tetsuya Ishikawa, and Jeffrey C Hansen. Nucleosomal arrays self-assemble into supramolecular globular structures lacking 30-nm fibers. *The EMBO Journal*, 35(10):1115–1132, 2016. ISSN 0261-4189. doi: [10.15252/embj.201592660](https://doi.org/10.15252/embj.201592660).
- [58] Thomas A. Volpe, Catherine Kidner, Ira M. Hall, Grace Teng, Shiv I.S. Grewal, and Robert A. Martienssen. Regulation of heterochromatic silencing and histone H3 lysine-9 methylation by RNAi. *Science*, 297(5588):1833–1837, 2002. ISSN 00368075. doi: [10.1126/science.1074973](https://doi.org/10.1126/science.1074973).
- [59] T. J. Richmond, J. T. Finch, B. Rushton, D. Rhodes, and A. Klug. Structure of the nucleosome core particle at 7 resolution. *Nature*, 311(5986):532–537, 1984. ISSN 00280836. doi: [10.1038/311532a0](https://doi.org/10.1038/311532a0).

- [60] Karolin Luger, Armin W Mäder, Robin K Richmond, David F Sargent, and Timothy J Richmond. Crystal structure of the nucleosome core particle at 2.8 Å resolution. *Nature*, 389:251 – 260, 1997.
- [61] Curt A. Davey, David F. Sargent, Karolin Luger, Armin W. Maeder, and Timothy J. Richmond. Solvent mediated interactions in the structure of the nucleosome core particle at 1.9 Å resolution. *Journal of Molecular Biology*, 319(5):1097–1113, 2002. ISSN 00222836. doi: [10.1016/S0022-2836\(02\)00386-8](https://doi.org/10.1016/S0022-2836(02)00386-8).
- [62] Fei Xu and Wilma K Olson. DNA Architecture, Deformability, and Nucleosome Positioning. *Journal of Biomolecular Structure and Dynamics*, 27(6):725–739, 2010. ISSN 15378276.
- [63] Gina Arents and Evangelos N. Moudrianakis. The histone fold: A ubiquitous architectural motif utilized in DNA compaction and protein dimerization. *Proceedings of the National Academy of Sciences of the United States of America*, 92(24):11170–11174, 1995. ISSN 00278424. doi: [10.1073/pnas.92.24.11170](https://doi.org/10.1073/pnas.92.24.11170).
- [64] Magdalena Gebala, Stephanie L. Johnson, Geeta J. Narlikar, and Dan Herschlag. Ion counting demonstrates a high electrostatic field generated by the nucleosome. *eLife*, 8:1–20, 2019. ISSN 2050084X. doi: [10.7554/eLife.44993](https://doi.org/10.7554/eLife.44993).
- [65] Melvin Noe Gonzalez, Ronald C. Conaway, and Joan W. Conaway. Frozen in Transcription: Cryo-EM Structures of Pol II Transcribing through a Nucleosome. *Molecular Cell*, 72(5):802–804, 2018. ISSN 10974164. doi: [10.1016/j.molcel.2018.11.027](https://doi.org/10.1016/j.molcel.2018.11.027).
- [66] Michael A. Hall, Alla Shundrovsky, Lu Bai, Robert M. Fulbright, John T. Lis, and Michelle D. Wang. High-resolution dynamic mapping of histone-DNA interactions in a nucleosome. *Nature Structural and Molecular Biology*, 16(2):124–129, 2009. ISSN 15459993. doi: [10.1038/nsmb.1526](https://doi.org/10.1038/nsmb.1526).
- [67] K. J. Polach and J. Widom. Mechanism of protein access to specific DNA sequences in chromatin: A dynamic equilibrium model for gene regulation. *Journal of Molecular Biology*, 254(2):130–149, 1995. ISSN 00222836. doi: [10.1006/jmbi.1995.0606](https://doi.org/10.1006/jmbi.1995.0606).
- [68] Silviya Bilokapić, Mike Strauss, and Mario Halić. Histone octamer rearranges to adapt to DNA unwrapping. *Nature Structural and Molecular Biology*, 25:101–108, 2018. ISSN 15459985. doi: [10.1038/s41594-017-0005-5](https://doi.org/10.1038/s41594-017-0005-5).
- [69] Thuy T.M. Ngo, Qiucen Zhang, Ruobo Zhou, Jaya G. Yodh, and Taekjip Ha. Asymmetric unwrapping of nucleosomes under tension directed by DNA local flexibility. *Cell*, 160:1135–1144, 2015. ISSN 10974172. doi: [10.1016/j.cell.2015.02.001](https://doi.org/10.1016/j.cell.2015.02.001).
- [70] P T Lowary and J Widom. New DNA sequence rules for high affinity binding to histone octamer and sequence-directed nucleosome positioning. *Journal of Molecular Biology*, 276:19–42, 1998.
- [71] P. T. Lowary and J. Widom. Nucleosome packaging and nucleosome positioning of genomic DNA. *Proceedings of the National Academy of Sciences*, 94(4):1183–1188, jul 1997. ISSN 0027-8424. doi: [10.1073/pnas.94.4.1183](https://doi.org/10.1073/pnas.94.4.1183).
- [72] A Thåström, P.T Lowary, and J Widom. Measurement of histone–DNA interaction free energy in nucleosomes. *Methods*, 33(1):33–44, may 2004. ISSN 10462023. doi: [10.1016/j.ymeth.2003.10.018](https://doi.org/10.1016/j.ymeth.2003.10.018).
- [73] Eran Segal, Yvonne Fondufe-Mittendorf, Lingyi Chen, Annchristine Thåström, Yair Field, Irene K. Moore, Ji Ping Z Wang, and Jonathan Widom. A genomic code for nucleosome positioning. *Nature*, 442(7104):772–778, aug 2006. ISSN 14764687. doi: [10.1038/nature04979](https://doi.org/10.1038/nature04979).
- [74] Eugene Y.D. Chua, Dileep Vasudevan, Gabriela E. Davey, Bin Wu, and Curt A. Davey. The mechanics behind DNA sequence-dependent properties of the nucleosome. *Nucleic Acids Research*, 40(13):6338–6352, 2012. ISSN 03051048. doi: [10.1093/nar/gks261](https://doi.org/10.1093/nar/gks261).

- [75] Aakash Basu, Dmitriy G Bobrovnikov, Zan Qureshi, Tunc Kayikcioglu, and Thuy T M Ngo. Measuring DNA mechanics on the genome scale. *Nature*, (April):1–24, 2020. ISSN 1476-4687. doi: 10.1038/s41586-020-03052-3.
- [76] M. Kruijthof and J. Van Noort. Hidden Markov analysis of nucleosome unwrapping under force. *Biophysical Journal*, 96(9):3708–3715, 2009. ISSN 15420086. doi: 10.1016/j.bpj.2009.01.048.
- [77] Shirley Mihadja, Andrew J. Spakowitz, Yongli Zhang, and Carlos Bustamante. Effect of force on mononucleosomal dynamics. *Proceedings of the National Academy of Sciences of the United States of America*, 103(43):15871–15876, 2006. ISSN 00278424. doi: 10.1073/pnas.0607526103.
- [78] Gu Li, Marcia Levitus, Carlos Bustamante, and Jonathan Widom. Rapid spontaneous accessibility of nucleosomal DNA. *Nature Structural and Molecular Biology*, 12(1):46–53, 2005. ISSN 15459993. doi: 10.1038/nsmb869.
- [79] Hannah S. Tims, Kaushik Gurunathan, Marcia Levitus, and Jonathan Widom. Dynamics of nucleosome invasion by DNA binding proteins. *Journal of Molecular Biology*, 411(2):430–448, 2011. ISSN 10898638. doi: 10.1016/j.jmb.2011.05.044.
- [80] Cedric R. Clapier and Bradley R. Cairns. The biology of chromatin remodeling complexes. *Annual Review of Biochemistry*, 78:273–304, 2009. ISSN 00664154. doi: 10.1146/annurev.biochem.77.062706.153223.
- [81] Felix Mueller-Planitz, Henrike Klinker, and Peter B. Becker. Nucleosome sliding mechanisms: New twists in a looped history. *Nature Structural and Molecular Biology*, 20(9):1026–1032, 2013. ISSN 15459993. doi: 10.1038/nsmb.2648.
- [82] Atsushi Miyagi, Toshio Ando, and Yuri L. Lyubchenko. Dynamics of nucleosomes assessed with time-lapse high-speed atomic force microscopy. *Biochemistry*, 50(37):7901–7908, sep 2011. ISSN 00062960. doi: 10.1021/bi200946z.
- [83] Allard J. Katan, Rifka Vlijm, Alexandra Lusser, and Cees Dekker. Dynamics of nucleosomal structures measured by high-speed atomic force microscopy. *Small*, 11(8):976–984, feb 2015. ISSN 16136829. doi: 10.1002/smll.201401318.
- [84] Julien Mozziconacci and Jean Marc Victor. Nucleosome gaping supports a functional structure for the 30 nm chromatin fiber. *Journal of Structural Biology*, 143(1):72–76, jul 2003. ISSN 10478477. doi: 10.1016/S1047-8477(03)00102-3.
- [85] Thuy T.M. Ngo and Taekjip Ha. Nucleosomes undergo slow spontaneous gaping. *Nucleic Acids Research*, 43(8):3964–3971, mar 2015. ISSN 13624962. doi: 10.1093/nar/gkv276.
- [86] Ju Yeon Lee and Tae Hee Lee. Effects of DNA methylation on the structure of nucleosomes. *Journal of the American Chemical Society*, 134(1):173–175, 2012. ISSN 00027863. doi: 10.1021/ja210273w.
- [87] Silvija Bilokapic, Mike Strauss, and Mario Halic. Structural rearrangements of the histone octamer translocate DNA. *Nature Communications*, 9(1):1–11, 2018. ISSN 20411723. doi: 10.1038/s41467-018-03677-z.
- [88] Alexandra Stützer, Stamatios Liokatis, Anja Kiesel, Dirk Schwarzer, Remco Sprangers, Johannes Söding, Philipp Selenko, and Wolfgang Fischle. Modulations of DNA Contacts by Linker Histones and Post-translational Modifications Determine the Mobility and Modifiability of Nucleosomal H3 Tails. *Molecular Cell*, 61:247–259, 2016. ISSN 10974164. doi: 10.1016/j.molcel.2015.12.015.
- [89] Hisashi Ishida and Hidetoshi Kono. H4 Tails Potentially Produce the Diversity in the Orientation of Two Nucleosomes. *Biophysical Journal*, 113(5):978–990, 2017. ISSN 15420086. doi: 10.1016/j.bpj.2017.07.015.

- [90] Keda Zhou, Guillaume Gaullier, and Karolin Luger. Nucleosome structure and dynamics are coming of age. *Nature Structural and Molecular Biology*, 26:3–13, 2019. ISSN 15459985. doi: [10.1038/s41594-018-0166-x](https://doi.org/10.1038/s41594-018-0166-x).
- [91] Igor Nazarov, Iana Chekharova, Georgy Rychkov, Andrey V. Ilatovskiy, Colyn Crane-Robinson, and Alexey Tomilin. AFM studies in diverse ionic environments of nucleosomes reconstituted on the 601 positioning sequence. *Biochimie*, 121:5–12, feb 2016. ISSN 61831638. doi: [10.1016/j.biochi.2015.11.010](https://doi.org/10.1016/j.biochi.2015.11.010).
- [92] Jan Lipfert, Sebastian Doniach, Rhiju Das, and Daniel Herschlag. *Understanding Nucleic Acid–Ion Interactions*, volume 83. Annual Reviews, jun 2014. ISBN 0604090927. doi: [10.1146/annurev-biochem-060409-092720](https://doi.org/10.1146/annurev-biochem-060409-092720).
- [93] Ali Hamiche, Patrick Schultz, V. Ramakrishnan, Pierre Oudet, and Ariel Prunell. Linker histone-dependent DNA structure in linear mononucleosomes. *Journal of Molecular Biology*, 257(1):30–42, 1996. ISSN 00222836. doi: [10.1006/jmbi.1996.0144](https://doi.org/10.1006/jmbi.1996.0144).
- [94] Martin Würtz, Dennis Aumiller, Lina Gundelwein, Philipp Jung, Christian Schütz, Kathrin Lehmann, Katalin Tóth, and Karl Rohr. DNA accessibility of chromatosomes quantified by automated image analysis of AFM data, dec 2019. ISSN 2045-2322, <http://www.nature.com/articles/s41598-019-49163-4>.
- [95] Jochen Felix Kepert, Katalin Fejes Tóth, Maiwen Caudron, Norbert Mücke, Jörg Langowski, and Karsten Rippe. Conformation of Reconstituted Mononucleosomes and Effect of Linker Histone H1 Binding Studied by Scanning Force Microscopy. *Biophysical Journal*, 85(6):4012–4022, 2003. ISSN 00063495. doi: [10.1016/S0006-3495\(03\)74815-2](https://doi.org/10.1016/S0006-3495(03)74815-2).
- [96] Jordanka Zlatanova, Sanford H. Leuba, and Kensal Van Holde. Chromatin fiber structure: Morphology, molecular determinants, structural transitions. *Biophysical Journal*, 74(5):2554–2566, 1998. ISSN 00063495. doi: [10.1016/S0006-3495\(98\)77963-9](https://doi.org/10.1016/S0006-3495(98)77963-9).
- [97] Sanford H. Leuba, Carlos Bustamante, Kensal Van Holde, and Jordanka Zlatanova. Linker histone tails and N-tails of histone H3 are redundant: Scanning force microscopy studies of reconstituted fibers. *Biophysical Journal*, 74(6):2830–2839, 1998. ISSN 00063495. doi: [10.1016/S0006-3495\(98\)77990-1](https://doi.org/10.1016/S0006-3495(98)77990-1).
- [98] Daniël P. Melters, Mary Pitman, Tatini Rakshit, Emiliós K. Dimitriadis, Minh Bui, Garegin A. Papoian, and Yamini Dalal. Intrinsic elasticity of nucleosomes is encoded by histone variants and calibrated by their binding partners. *Proceedings of the National Academy of Sciences of the United States of America*, 116(48):24066–24074, 2019. ISSN 10916490. doi: [10.1073/pnas.1911880116](https://doi.org/10.1073/pnas.1911880116).
- [99] Yamini Dalal, Hongda Wang, Stuart Lindsay, and Steven Henikoff. Tetrameric structure of centromeric nucleosomes in interphase *Drosophila* cells. *PLoS Biology*, 5(8):1798–1809, 2007. ISSN 15449173. doi: [10.1371/journal.pbio.0050218](https://doi.org/10.1371/journal.pbio.0050218).
- [100] Matthew D.D. Miell, Colin J. Fuller, Annika Guse, Helena M. Barysz, Andrew Downes, Tom Owen-Hughes, Juri Rappsilber, Aaron F. Straight, and Robin C. Allshire. CENP-A confers a reduction in height on octameric nucleosomes. *Nature Structural and Molecular Biology*, 20(6):763–765, jun 2013. ISSN 15459993. doi: [10.1038/nsmb.2574](https://doi.org/10.1038/nsmb.2574).
- [101] Marcin P. Walkiewicz, Emiliós K. Dimitriadis, and Yamini Dalal. CENP-A octamers do not confer a reduction in nucleosome height by AFM. *Nature Structural and Molecular Biology*, 21(1):2–3, 2014. ISSN 15459993. doi: [10.1038/nsmb.2742](https://doi.org/10.1038/nsmb.2742).
- [102] Christine A. Codomo, Takehito Furuyama, and Steven Henikoff. CENP-A octamers do not confer a reduction in nucleosome height by AFM. *Nature Structural and Molecular Biology*, 21(1):4–5, jan 2014. ISSN 15459993. doi: [10.1038/nsmb.2743](https://doi.org/10.1038/nsmb.2743).

- [103] Yuri L. Lyubchenko. Centromere chromatin: a loose grip on the nucleosome? *Nature Structural and Molecular Biology*, 21(1):8, jan 2014. ISSN 15459993. doi: [10.1038/nsmb.2745](https://doi.org/10.1038/nsmb.2745).
- [104] Luda S. Shlyakhtenko, Alexander Y. Lushnikov, and Yuri L. Lyubchenko. Dynamics of nucleosomes revealed by time-lapse atomic force microscopy. *Biochemistry*, 48(33):7842–7848, aug 2009. ISSN 00062960. doi: [10.1021/bi900977t](https://doi.org/10.1021/bi900977t).
- [105] Micah P. Stumme-Diers, Siddhartha Banerjee, Mohtadin Hashemi, Zhiqiang Sun, and Yuri L. Lyubchenko. Nanoscale dynamics of centromere nucleosomes and the critical roles of CENP-A. *Nucleic Acids Research*, 46(1):94–103, 2018. ISSN 13624962. doi: [10.1093/nar/gkx933](https://doi.org/10.1093/nar/gkx933).
- [106] Tommy Stormberg, Micah Stumme-Diers, and Yuri L. Lyubchenko. Sequence-dependent nucleosome nanoscale structure characterized by atomic force microscopy. *The FASEB Journal*, 33(10): 10916–10923, oct 2019. ISSN 0892-6638. doi: [10.1096/fj.201901094r](https://doi.org/10.1096/fj.201901094r).
- [107] Lacramioara Bintu, Marta Kopaczynska, Courtney Hodges, Lucyna Lubkowska, Mikhail Kashlev, and Carlos Bustamante. The elongation rate of RNA polymerase determines the fate of transcribed nucleosomes. *Nature Structural and Molecular Biology*, 18(12):1394–1399, dec 2011. ISSN 15459993. doi: [10.1038/nsmb.2164](https://doi.org/10.1038/nsmb.2164).
- [108] Nina A. Filenko, Dmytro B. Palets, and Yuri L. Lyubchenko. Structure and Dynamics of Dinucleosomes Assessed by Atomic Force Microscopy. *Journal of Amino Acids*, 2012:1–6, 2012. ISSN 2090-0104. doi: [10.1155/2012/650840](https://doi.org/10.1155/2012/650840).
- [109] Paula Wiggins, Thijn Van Der Heijden, Fernando Moreno-Herrero, Andrew Spakowitz, Rob Phillips, Jonathan Widom, Cees Dekker, and Philip C. Nelson. High flexibility of DNA on short length scales probed by atomic force microscopy. *Nature Nanotechnology*, 1(2):137–141, 2006. ISSN 17483395. doi: [10.1038/nnano.2006.63](https://doi.org/10.1038/nnano.2006.63).
- [110] Disha M. Bangalore, Hannah S. Heil, Christian F. Mehringer, Lisa Hirsch, Katherina Hemmen, Katrina G. Heinze, and Ingrid Tessmer. Automated AFM analysis of DNA bending reveals initial lesion sensing strategies of DNA glycosylases. *Scientific Reports*, 10(1):1–15, 2020. ISSN 20452322. doi: [10.1038/s41598-020-72102-7](https://doi.org/10.1038/s41598-020-72102-7).
- [111] S. Venkataraman, D. P. Allison, H. Qi, J. L. Morrell-Falvey, N. L. Kallewaard, J. E. Crowe, and M. J. Doktycz. Automated image analysis of atomic force microscopy images of rotavirus particles. *Ultramicroscopy*, 106(8-9):829–837, jun 2006. ISSN 03043991. doi: [10.1016/j.ultramic.2006.01.014](https://doi.org/10.1016/j.ultramic.2006.01.014).
- [112] Sebastian F. Konrad, Willem Vanderlinden, Wout Frederickx, Tine Brouns, Björn H Menze, Steven De Feyter, and Jan Lipfert. High-throughput AFM analysis reveals unwrapping pathways of H3 and CENP-A nucleosomes. *Nanoscale*, 13:5435–5447, 2021. doi: [10.1039/d0nr08564b](https://doi.org/10.1039/d0nr08564b).
- [113] Irina Menshikova, Evgeny Menshikov, Nina Filenko, and Yuri L. Lyubchenko. Nucleosomes structure and dynamics: Effect of CHAPS. *International Journal of Biochemistry and Molecular Biology*, 2(2): 129–137, 2011. ISSN 21524114.
- [114] Chloe M. Rivera and Bing Ren. Mapping Human Epigenomes, sep 2013. ISSN 00928674.
- [115] Brian R. Keppler and Trevor K. Archer. Chromatin-modifying enzymes as therapeutic targets - Part 2. *Expert Opinion on Therapeutic Targets*, 12(10):1301–1312, 2008. ISSN 14728222. doi: [10.1517/14728222.12.11.1457](https://doi.org/10.1517/14728222.12.11.1457).
- [116] G Allfrey, R Faulkner, and A E Mirsky. Acetylation and methylation of histones and their possible role in the regulation of RNA synthesis. *Proceedings of the National Academy of Sciences*, 51(5):786–794, 1964.

- [117] Anna Sadakierska-Chudy and Małgorzata Filip. A Comprehensive View of the Epigenetic Landscape. Part II: Histone Post-translational Modification, Nucleosome Level, and Chromatin Regulation by ncRNAs. *Neurotoxicity Research*, 27:172–197, 2015. ISSN 14763524. doi: [10.1007/s12640-014-9508-6](https://doi.org/10.1007/s12640-014-9508-6).
- [118] C. Ann Blakey and Michael D. Litt. Histone modifications-models and mechanisms. In *Epigenetic Gene Expression and Regulation*, pages 21–42. 2015. ISBN 9780128004715.
- [119] Feng Xu, Kangling Zhang, and Michael Grunstein. Acetylation in histone H3 globular domain regulates gene expression in yeast. *Cell*, 121:375–385, 2005. ISSN 00928674. doi: [10.1016/j.cell.2005.03.011](https://doi.org/10.1016/j.cell.2005.03.011).
- [120] Stephanie K. Williams, David Truong, and Jessica K. Tyler. Acetylation in the globular core of histone H3 on lysine-56 promotes chromatin disassembly during transcriptional activation. *Proceedings of the National Academy of Sciences of the United States of America*, 105(26):9000–9005, 2008. ISSN 00278424. doi: [10.1073/pnas.0800057105](https://doi.org/10.1073/pnas.0800057105).
- [121] Hiroshi Masumoto, David Hawke, Ryuji Kobayashi, and Alain Verreault. A role for cell-cycle-regulated histone H3 lysine 56 acetylation in the DNA damage response. *Nature*, 436, 2005. ISSN 00280836. doi: [10.1038/nature03714](https://doi.org/10.1038/nature03714).
- [122] John C. Shimko, Justin A. North, Aaron N. Bruns, Michael G. Poirier, and Jennifer J. Ottesen. Preparation of fully synthetic histone H3 reveals that acetyl-lysine 56 facilitates protein binding within nucleosomes. *Journal of Molecular Biology*, 408:187–204, 2011. ISSN 00222836. doi: [10.1016/j.jmb.2011.01.003](https://doi.org/10.1016/j.jmb.2011.01.003).
- [123] Heinz Neumann, Susan M. Hancock, Ruth Buning, Andrew Routh, Lynda Chapman, Joanna Somers, Tom Owen-Hughes, John van Noort, Daniela Rhodes, and Jason W. Chin. A Method for Genetically Installing Site-Specific Acetylation in Recombinant Histones Defines the Effects of H3 K56 Acetylation. *Molecular Cell*, 36:153–163, 2009. ISSN 10972765. doi: [10.1016/j.molcel.2009.07.027](https://doi.org/10.1016/j.molcel.2009.07.027).
- [124] Ruihan Zhang, Jochen Erler, and Jörg Langowski. Histone Acetylation Regulates Chromatin Accessibility: Role of H4K16 in Inter-nucleosome Interaction. *Biophysical Journal*, 112:450–459, 2017. ISSN 15420086. doi: [10.1016/j.bpj.2016.11.015](https://doi.org/10.1016/j.bpj.2016.11.015).
- [125] Michael Shogren-Knaak, Haruhiko Ishii, Jian Min Sun, Michael J. Pazin, James R. Davie, and Craig L. Peterson. Histone H4-K16 acetylation controls chromatin structure and protein interactions. *Science*, 311(5762):844–847, feb 2006. ISSN 00368075. doi: [10.1126/science.1124000](https://doi.org/10.1126/science.1124000).
- [126] Surbhi Dhar, Ozge Gursoy-Yuzugullu, Ramya Parasuram, and Brendan D. Price. The tale of a tail: Histone H4 acetylation and the repair of DNA breaks. *Philosophical Transactions of the Royal Society B: Biological Sciences*, 372(1731), 2017. ISSN 14712970. doi: [10.1098/rstb.2016.0284](https://doi.org/10.1098/rstb.2016.0284).
- [127] Christopher R. Vakoc, Sean A. Mandat, Benjamin A. Olenchock, and Gerd A. Blobel. Histone H3 lysine 9 methylation and HP1 $\gamma$  are associated with transcription elongation through mammalian chromatin. *Molecular Cell*, 19(3):381–391, 2005. ISSN 10972765. doi: [10.1016/j.molcel.2005.06.011](https://doi.org/10.1016/j.molcel.2005.06.011).
- [128] Matthew Brehove, Tao Wang, Justin North, Yi Luo, Sarah J. Dreher, John C. Shimko, Jennifer J. Ottesen, Karolin Luger, and Michael G. Poirier. Histone core phosphorylation regulates DNA accessibility. *Journal of Biological Chemistry*, 290(37):22612–22621, 2015. ISSN 1083351X. doi: [10.1074/jbc.M115.661363](https://doi.org/10.1074/jbc.M115.661363).
- [129] Justin A. North, Sarah Javaid, Michelle B. Ferdinand, Nilanjana Chatterjee, Jonathan W. Picking, Matthew Shoffner, Robin J. Nakkula, Blaine Bartholomew, Jennifer J. Ottesen, Richard Fishel, and Michael G. Poirier. Phosphorylation of histone H3(T118) alters nucleosome dynamics and remodeling. *Nucleic Acids Research*, 39(15):6465–6474, aug 2011. ISSN 03051048. doi: [10.1093/nar/gkr304](https://doi.org/10.1093/nar/gkr304).

- [130] Justin A. North, Marek Šimon, Michelle B. Ferdinand, Matthew A. Shoffner, Jonathan W. Picking, Cecil J. Howard, Alex M. Mooney, John Van Noort, Michael G. Poirier, and Jennifer J. Ottesen. Histone H3 phosphorylation near the nucleosome dyad alters chromatin structure. *Nucleic Acids Research*, 42(8):4922–4933, 2014. ISSN 13624962. doi: [10.1093/nar/gku150](https://doi.org/10.1093/nar/gku150).
- [131] Rakesh Kumar Singh and Akash Gunjan. Histone tyrosine phosphorylation comes of age. *Epigenetics*, 6(2):153–160, 2011. ISSN 15592308. doi: [10.4161/epi.6.2.13589](https://doi.org/10.4161/epi.6.2.13589).
- [132] Jun Y. Fan, Faye Gordon, Karolin Luger, Jeffrey C. Hansen, and David John Tremethick. The essential histone variant H2A.Z regulates the equilibrium between different chromatin conformational states. *Nature Structural Biology*, 9(3):172–176, 2002. ISSN 10728368. doi: [10.1038/nsb767](https://doi.org/10.1038/nsb767).
- [133] Srinivas Chakravarthy, Ashok Patel, and Gregory D. Bowman. The basic linker of macroH2A stabilizes DNA at the entry/exit site of the nucleosome. *Nucleic Acids Research*, 40(17):8285–8295, 2012. ISSN 03051048. doi: [10.1093/nar/gks645](https://doi.org/10.1093/nar/gks645).
- [134] Yunhe Bao, Kasey Konesky, Young Jun Park, Simona Rosu, Pamela N. Dyer, Danny Rangasamy, David J. Tremethick, Paul J. Laybourn, and Karolin Luger. Nucleosomes containing the histone variant H2A.Bbd organize only 118 base pairs of DNA. *EMBO Journal*, 23(16):3314–3324, 2004. ISSN 02614189. doi: [10.1038/sj.emboj.7600316](https://doi.org/10.1038/sj.emboj.7600316).
- [135] Sara Martire and Laura A. Banaszynski. The roles of histone variants in fine-tuning chromatin organization and function. *Nature Reviews Molecular Cell Biology*, 21(9):522–541, 2020. ISSN 14710080. doi: [10.1038/s41580-020-0262-8](https://doi.org/10.1038/s41580-020-0262-8).
- [136] Chunyuan Jin and Gary Felsenfeld. Nucleosome stability mediated by histone variants H3.3 and H2A.Z. *Genes and Development*, 21(12):1519–1529, 2007. ISSN 08909369. doi: [10.1101/gad.1547707](https://doi.org/10.1101/gad.1547707).
- [137] Hiroaki Tachiwana, Wataru Kagawa, Tatsuya Shiga, Akihisa Osakabe, Yuta Miya, Kengo Saito, Yoko Hayashi-Takanaka, Takashi Oda, Mamoru Sato, Sam Yong Park, Hiroshi Kimura, and Hitoshi Kurumizaka. Crystal structure of the human centromeric nucleosome containing CENP-A. *Nature*, 476(7359):232–235, aug 2011. ISSN 00280836. doi: [10.1038/nature10258](https://doi.org/10.1038/nature10258).
- [138] Timothy J Richmond and Curt A Davey. The structure of DNA in the nucleosome core. *Nature*, 423:145–150, 2003. doi: [10.1038/nature01595](https://doi.org/10.1038/nature01595).
- [139] Geeta J. Narlikar, Ramasubramanian Sundaramoorthy, and Tom Owen-Hughes. Mechanisms and functions of ATP-dependent chromatin-remodeling enzymes. *Cell*, 154(3):490–503, 2013. ISSN 00928674. doi: [10.1016/j.cell.2013.07.011](https://doi.org/10.1016/j.cell.2013.07.011).
- [140] Orkide Ordu, Alexandra Lusser, and Nynke H. Dekker. Recent insights from in vitro single-molecule studies into nucleosome structure and dynamics. *Biophysical Reviews*, 8:33–49, 2016. ISSN 18672469. doi: [10.1007/s12551-016-0212-z](https://doi.org/10.1007/s12551-016-0212-z).
- [141] George Sirinakis, Cedric R. Clapier, Ying Gao, Ramya Viswanathan, Bradley R. Cairns, and Yongli Zhang. The RSC chromatin remodelling ATPase translocates DNA with high force and small step size. *EMBO Journal*, 30(12):2364–2372, 2011. ISSN 02614189. doi: [10.1038/emboj.2011.141](https://doi.org/10.1038/emboj.2011.141).
- [142] Gu Li and Jonathan Widom. Nucleosomes facilitate their own invasion. *Nature Structural and Molecular Biology*, 11(8):763–769, aug 2004. doi: [10.1038/nsmb801](https://doi.org/10.1038/nsmb801).
- [143] Artur Kaczmarczyk, He Meng, Orkide Ordu, John van Noort, and Nynke H. Dekker. Chromatin fibers stabilize nucleosomes under torsional stress. *Nature Communications*, 11(1):1–12, 2020. ISSN 20411723. doi: [10.1038/s41467-019-13891-y](https://doi.org/10.1038/s41467-019-13891-y).

- [144] S. Mihardja, A. J. Spakowitz, Y. Zhang, and C. Bustamante. Effect of force on mononucleosomal dynamics. *Proceedings of the National Academy of Sciences*, 103(43):15871–15876, oct 2006. ISSN 0027-8424. doi: [10.1073/pnas.0607526103](https://doi.org/10.1073/pnas.0607526103).
- [145] Daniel J. Schlingman, Andrew H. Mack, Masha Kamenetska, Simon G.J. Mochrie, and Lynne Regan. Routes to DNA accessibility: Alternative pathways for nucleosome unwinding. *Biophysical Journal*, 107(2):384–392, 2014. ISSN 15420086. doi: [10.1016/j.bpj.2014.05.042](https://doi.org/10.1016/j.bpj.2014.05.042).
- [146] Toshio Ando. High-speed atomic force microscopy and its future prospects. *Biophysical Reviews*, 10(2):285–292, 2018. ISSN 18672469. doi: [10.1007/s12551-017-0356-5](https://doi.org/10.1007/s12551-017-0356-5).
- [147] T. Brouns, H. De Keersmaecker, S.F. Konrad, N. Kodera, T. Ando, J. Lipfert, S. De Feyter, and W. Vanderlinden. Free Energy Landscape and Dynamics of Supercoiled DNA by High-Speed Atomic Force Microscopy. *ACS Nano*, 12:11907–11916, 2018. ISSN 1936086X.
- [148] M. Bussiek, N. Mücke, and J. Langowski. Polylysine-coated mica can be used to observe systematic changes in the supercoiled DNA conformation by scanning force microscopy in solution. *Nucleic Acids Research*, 31(22):e137, 2003. ISSN 1362-4962. doi: [10.1093/nar/gng137](https://doi.org/10.1093/nar/gng137).
- [149] Nils Krietenstein, Christian J. Wippo, Corinna Lieleg, and Philipp Korber. Genome-wide in vitro reconstitution of yeast chromatin with in vivo-like nucleosome positioning. *Methods in Enzymology*, 513:205–232, 2012. ISSN 15577988. doi: [10.1016/B978-0-12-391938-0.00009-4](https://doi.org/10.1016/B978-0-12-391938-0.00009-4).
- [150] Nic Mullin and Jamie K. Hobbs. A non-contact, thermal noise based method for the calibration of lateral deflection sensitivity in atomic force microscopy. *Review of Scientific Instruments*, 85(11), 2014. ISSN 10897623. doi: [10.1063/1.4901221](https://doi.org/10.1063/1.4901221).
- [151] John Van Noort, Francesco Orsini, Andre Eker, Claire Wyman, Bart De Groot, and Jan Greve. DNA bending by photolyase in specific and non-specific complexes studied by atomic force microscopy. *Nucleic Acids Research*, 27(19):3875–3880, 1999. ISSN 03051048. doi: [10.1093/nar/27.19.3875](https://doi.org/10.1093/nar/27.19.3875).
- [152] Andrew J. Bannister and Tony Kouzarides. Regulation of chromatin by histone modifications. *Cell Research*, 21:381–395, 2011.
- [153] Peter Tessarz and Tony Kouzarides. Histone core modifications regulating nucleosome structure and dynamics. *Nature Reviews Molecular Cell Biology*, 15:703–708, 2014. ISSN 14710080. doi: [10.1038/nrm3890](https://doi.org/10.1038/nrm3890).
- [154] Karolin Luger. Dynamic nucleosomes. *Chromosome Research*, 14(1):5–16, feb 2006. ISSN 09673849. doi: [10.1007/s10577-005-1026-1](https://doi.org/10.1007/s10577-005-1026-1).
- [155] Courtney Hodges, Lacramioara Bintu, Lucyna Lubkowska, Mikhail Kashlev, and Carlos Bustamante. Nucleosomal fluctuations govern the transcription dynamics of RNA polymerase II. *Science*, 325(5940):626–628, 2009. ISSN 00368075. doi: [10.1126/science.1172926](https://doi.org/10.1126/science.1172926).
- [156] Fabrizio Cleri, Fabio Landuzzi, and Ralf Blossey. Mechanical evolution of DNA double-strand breaks in the nucleosome. *PLoS Computational Biology*, 14(6):1–24, 2018. ISSN 15537358. doi: [10.1371/journal.pcbi.1006224](https://doi.org/10.1371/journal.pcbi.1006224).
- [157] Ozge Gursoy-Yuzugullu, Nealia House, and Brendan D. Price. Patching Broken DNA: Nucleosome Dynamics and the Repair of DNA Breaks. *Journal of Molecular Biology*, 428(9):1846–1860, 2016. ISSN 10898638. doi: [10.1016/j.jmb.2015.11.021](https://doi.org/10.1016/j.jmb.2015.11.021).
- [158] Yi Luo, Justin A. North, Sean D. Rose, and Michael G. Poirier. Nucleosomes accelerate transcription factor dissociation. *Nucleic Acids Research*, 42(5):3017–3027, 2014. ISSN 13624962. doi: [10.1093/nar/gkt1319](https://doi.org/10.1093/nar/gkt1319).

- [159] Ralf Blossey and Helmut Schiessel. The dynamics of the nucleosome: Thermal effects, external forces and ATP. *FEBS Journal*, 278(19):3619–3632, 2011. ISSN 17424658. doi: [10.1111/j.1742-4658.2011.08283.x](https://doi.org/10.1111/j.1742-4658.2011.08283.x).
- [160] Kurt Andresen, Isabel Jimenez-Useche, Steven C. Howell, Chongli Yuan, and Xiangyun Qiu. Solution scattering and FRET studies on nucleosomes reveal DNA unwrapping effects of H3 and H4 tail removal. *PLoS ONE*, 8(11):1–9, 2013. ISSN 19326203. doi: [10.1371/journal.pone.0078587](https://doi.org/10.1371/journal.pone.0078587).
- [161] Douglas K Palmer, Kathleen O'Day Day, Hai Le Trong, Harry Charbonneau, and Robert L Margolis. Purification of the centromere-specific protein CENP-A and demonstration that it is a distinctive histone. *Proceedings of the National Academy of Sciences of the United States of America*, 88(May): 3734–3738, 1991.
- [162] Yael Nechemia-Arbely, Daniele Fachinetti, Karen H. Miga, Nikolina Sekulic, Gautam V. Soni, Dong Hyun Kim, Adeline K. Wong, Ah Young Lee, Kristen Nguyen, Cees Dekker, Bing Ren, Ben E. Black, and Don W. Cleveland. Human centromeric CENP-A chromatin is a homotypic, octameric nucleosome at all cell cycle points. *The Journal of cell biology*, 216(3):607–621, mar 2017. ISSN 15408140. doi: [10.1083/jcb.201608083](https://doi.org/10.1083/jcb.201608083).
- [163] Ahmad Ali-Ahmad, Silvija Bilokapić, Ingmar B Schäfer, Mario Halić, and Nikolina Sekulić. CENP-C unwraps the human CENP-A nucleosome through the H2A C-terminal tail. *EMBO reports*, 20:1–13, sep 2019. ISSN 1469-221X. doi: [10.15252/embr.201948913](https://doi.org/10.15252/embr.201948913).
- [164] Willem Vanderlinden, Jan Lipfert, Jonas Demeulemeester, Zeger Debyser, and Steven De Feyter. Structure, mechanics, and binding mode heterogeneity of LEDGF/p75-DNA nucleoprotein complexes revealed by scanning force microscopy. *Nanoscale*, 6(9):4611–4619, 2014. ISSN 20403372. doi: [10.1039/c4nr00022f](https://doi.org/10.1039/c4nr00022f).
- [165] T Y Zhang and C Y Suen. A fast parallel algorithm for thinning digital patterns, 1984.
- [166] Claudio Rivetti, Martin Guthold, and Carlos Bustamante. Scanning force microscopy of DNA deposited onto mica: Equilibration versus kinetic trapping studied by statistical polymer chain analysis. *Journal of Molecular Biology*, 264(5):919–932, 1996. ISSN 00222836. doi: [10.1006/jmbi.1996.0687](https://doi.org/10.1006/jmbi.1996.0687).
- [167] Thomas Zettl, Rebecca S. Mathew, Sönke Seifert, Sebastian Doniach, Pehr A.B. Harbury, and Jan Lipfert. Absolute Intramolecular Distance Measurements with Angstrom-Resolution Using Anomalous Small-Angle X-ray Scattering. *Nano Letters*, 16(9):5353–5357, 2016. ISSN 15306992. doi: [10.1021/acs.nanolett.6b01160](https://doi.org/10.1021/acs.nanolett.6b01160).
- [168] Mekonnen Lemma Dechassa, Katharina Wyns, Ming Li, Michael A. Hall, Michelle D. Wang, and Karolin Luger. Structure and Scm3-mediated assembly of budding yeast centromeric nucleosomes, 2011. ISSN 20411723.
- [169] Ming Li and Michelle D. Wang. *Unzipping single DNA molecules to study nucleosome structure and dynamics*, volume 513. Elsevier Inc., 1 edition, 2012. ISBN 9780123919380. doi: [10.1016/B978-0-12-391938-0.00002-1](https://doi.org/10.1016/B978-0-12-391938-0.00002-1).
- [170] Malte Bussiek, Katalin Tóth, Nathalie Brun, and Jörg Langowski. DNA-loop formation on nucleosomes shown by in situ scanning force microscopy of supercoiled DNA. *Journal of Molecular Biology*, 345(4): 695–706, 2005. ISSN 00222836. doi: [10.1016/j.jmb.2004.11.016](https://doi.org/10.1016/j.jmb.2004.11.016).
- [171] Alexander Gansen, Alessandro Valeri, Florian Hauger, Suren Felekyan, Stanislav Kalinin, Katalin Tóth, Jörg Langowski, and Claus A.M. Seidel. Nucleosome disassembly intermediates characterized by single-molecule FRET. *Proceedings of the National Academy of Sciences of the United States of America*, 106(36): 15308–15313, 2009. ISSN 00278424. doi: [10.1073/pnas.0903005106](https://doi.org/10.1073/pnas.0903005106).

- [172] W. J. A. Koopmans, R. Buning, T. Schmidt, and J. Van Noort. spFRET using alternating excitation and FCS reveals progressive DNA unwrapping in nucleosomes. *Biophysical Journal*, 97(1):195–204, 2009. ISSN 15420086. doi: [10.1016/j.bpj.2009.04.030](https://doi.org/10.1016/j.bpj.2009.04.030).
- [173] Kathrin Lehmann, Ruihan Zhang, Nathalie Schwarz, Alexander Gansen, Norbert Mücke, Jörg Langowski, and Katalin Toth. Effects of charge-modifying mutations in histone H2A  $\alpha$ 3-domain on nucleosome stability assessed by single-pair FRET and MD simulations. *Scientific Reports*, 7(1):1–14, 2017. ISSN 20452322. doi: [10.1038/s41598-017-13416-x](https://doi.org/10.1038/s41598-017-13416-x).
- [174] Dengke Zhao, Jenny V. Le, Michael A. Darcy, Kyle Crocker, Michael G. Poirier, Carlos Castro, and Ralf Bundschuh. Quantitative Modeling of Nucleosome Unwrapping from Both Ends. *Biophysical Journal*, 117(11):2204–2216, 2019. ISSN 15420086. doi: [10.1016/j.bpj.2019.09.048](https://doi.org/10.1016/j.bpj.2019.09.048).
- [175] Lennart De Bruin, Marco Tompitak, Behrouz Eslami-Mossallam, and Helmut Schiessel. Why do nucleosomes unwrap asymmetrically? *Journal of Physical Chemistry B*, 120(26):5855–5863, jul 2016. ISSN 15205207. doi: [10.1021/acs.jpcc.6b00391](https://doi.org/10.1021/acs.jpcc.6b00391).
- [176] Tanya Panchenko, Troy C. Sorensen, Christopher L. Woodcock, Zhong Yuan Kan, Stacey Wood, Michael G. Resch, Karolin Luger, S. Walter Englander, Jeffrey C. Hansen, and Ben E. Black. Replacement of histone H3 with CENP-A directs global nucleosome array condensation and loosening of nucleosome superhelical termini. *Proceedings of the National Academy of Sciences of the United States of America*, 108(40):16588–16593, 2011. ISSN 00278424. doi: [10.1073/pnas.1113621108](https://doi.org/10.1073/pnas.1113621108).
- [177] Sung Hyun Kim, Rifka Vlijm, Jaco Van Der Torre, Yamini Dalal, and Cees Dekker. CENP-A and H3 nucleosomes display a similar stability to force-mediated disassembly. *PLoS ONE*, 11(11):1–18, 2016. ISSN 19326203. doi: [10.1371/journal.pone.0165078](https://doi.org/10.1371/journal.pone.0165078).
- [178] Kinya Yoda, Satoshi Ando, Setsuo Morishita, Kenichi Houmura, Keiji Hashimoto, Kunio Takeyasu, and Tuneko Okazaki. Human centromere protein A (CENP-A) can replace histone H3 in nucleosome reconstitution in vitro. *Proceedings of the National Academy of Sciences of the United States of America*, 97(13):7266–7271, 2000. ISSN 00278424. doi: [10.1073/pnas.130189697](https://doi.org/10.1073/pnas.130189697).
- [179] Natalia Conde e Silva, Ben E. Black, Andrei Sivolob, Jan Filipinski, Don W. Cleveland, and Ariel Prunell. CENP-A-containing Nucleosomes: Easier Disassembly versus Exclusive Centromeric Localization. *Journal of Molecular Biology*, 370(3):555–573, 2007. ISSN 00222836. doi: [10.1016/j.jmb.2007.04.064](https://doi.org/10.1016/j.jmb.2007.04.064).
- [180] Ramachandran Boopathi, Radostin Danev, Maryam Khoshouei, Seyit Kale, Sunil Nahata, Lorrie Ramos, Dimitar Angelov, Stefan Dimitrov, Ali Hamiche, Carlo Petosa, and Jan Bednar. Phase-plate cryo-EM structure of the Widom 601 CENP-A nucleosome core particle reveals differential flexibility of the DNA ends. *Nucleic acids research*, 48(10):5735–5748, 2020. ISSN 13624962. doi: [10.1093/nar/gkaa246](https://doi.org/10.1093/nar/gkaa246).
- [181] Samantha J. Falk, Lucie Y. Guo, Nikolina Sekulic, Evan M. Smoak, Tomoyasu Mani, Glennis A. Logsdon, Kushol Gupta, Lars E. T. Jansen, Gregory D. Van Duyne, Sergei A. Vinogradov, Michael A. Lampson, and Ben E. Black. CENP-C reshapes and stabilizes CENP-A nucleosomes at the centromere. *Science*, 348(6235):699–703, 2015.
- [182] Hidetoshi Kono, Shun Sakuraba, and Hisashi Ishida. Free energy profile for unwrapping outer superhelical turn of CENP-A nucleosome. *Biophysics and Physicobiology*, 16:337–343, 2019. doi: [10.2142/biophysico.16.0](https://doi.org/10.2142/biophysico.16.0).
- [183] Minh Bui, Emiliós K. Dimitriadis, Christian Hoischen, Eunkyung An, Delphine Quénet, Sindy Giebe, Aleksandra Nita-Lazar, Stephan Diekmann, and Yamini Dalal. Cell-cycle-dependent structural transitions in the human CENP-A nucleosome in vivo. *Cell*, 150(2):317–326, 2012. ISSN 00928674. doi: [10.1016/j.cell.2012.05.035](https://doi.org/10.1016/j.cell.2012.05.035).

- [184] Minh Bui, Marcin P. Walkiewicz, Emiliós K. Dimitriadis, and Yamini Dalal. The CENP-A nucleosome. A battle between Dr. Jekyll and Mr. Hyde. *Nucleus (United States)*, 4(1):37–42, 2013. ISSN 19491042. doi: [10.4161/nucl.23588](https://doi.org/10.4161/nucl.23588).
- [185] Tatini Rakshit, Daniël P. Melters, Emiliós K. Dimitriadis, and Yamini Dalal. Mechanical properties of nucleoprotein complexes determined by nanoindentation spectroscopy. *Nucleus*, 11(1):264–282, 2020. ISSN 19491042. doi: [10.1080/19491034.2020.1816053](https://doi.org/10.1080/19491034.2020.1816053).
- [186] David Winogradoff, Haiqing Zhao, Yamini Dalal, and Garegin A. Papoian. Shearing of the CENP-A dimerization interface mediates plasticity in the octameric centromeric nucleosome. *Scientific Reports*, 5 (June):1–14, 2015. ISSN 20452322. doi: [10.1038/srep17038](https://doi.org/10.1038/srep17038).
- [187] Marta Garcia-Ramirez, Corinne Rocchini, and Juan Ausio. Modulation of Chromatin Folding by Histone Acetylation. *The Journal of Biological Chemistry*, 270:17923–17928, 1995.
- [188] Benedetta Dorigo, Thomas Schalch, Kerstin Bystricky, and Timothy J. Richmond. Chromatin fiber folding: Requirement for the histone H4 N-terminal tail. *Journal of Molecular Biology*, 327(1):85–96, 2003. ISSN 00222836. doi: [10.1016/S0022-2836\(03\)00025-1](https://doi.org/10.1016/S0022-2836(03)00025-1).
- [189] Manisha Sinha and Craig L. Peterson. Chromatin dynamics during repair of chromosomal DNA double-strand breaks. *Epigenomics*, 1(2):371–385, 2009. ISSN 17501911. doi: [10.2217/EPI.09.22](https://doi.org/10.2217/EPI.09.22).
- [190] Geneviève Almouzni and Howard Cedar. Maintenance of epigenetic information, 2016. ISSN 19430264.
- [191] Alexander W. Mauney, Joshua M. Tokuda, Lisa M. Gloss, Oscar Gonzalez, and Lois Pollack. Local DNA Sequence Controls Asymmetry of DNA Unwrapping from Nucleosome Core Particles. *Biophysical Journal*, 115(5):773–781, sep 2018. ISSN 15420086. doi: [10.1016/j.bpj.2018.07.009](https://doi.org/10.1016/j.bpj.2018.07.009).
- [192] Kaige Yan, Ziguó Zhang, Jing Yang, Stephen H. McLaughlin, and David Barford. Architecture of the CBF3–centromere complex of the budding yeast kinetochore. *Nature Structural and Molecular Biology*, 25(12):1103–1110, 2018. ISSN 15459985. doi: [10.1038/s41594-018-0154-1](https://doi.org/10.1038/s41594-018-0154-1).
- [193] H. Masumoto, H. Masukata, Y. Muro, N. Nozaki, and T. Okazaki. A human centromere antigen (CENP-B) interacts with a short specific sequence in alphoid DNA, a human centromeric satellite. *Journal of Cell Biology*, 109(5):1963–1973, 1989. ISSN 00219525. doi: [10.1083/jcb.109.5.1963](https://doi.org/10.1083/jcb.109.5.1963).
- [194] Gaurav Arya and Tamar Schlick. A tale of tails: how histone tails mediate chromatin compaction in different salt and linker histone environments. *Journal of Physical Chemistry A*, 113(16):4045–4059, 2009. ISSN 10895639. doi: [10.1021/jp810375d](https://doi.org/10.1021/jp810375d).
- [195] Rosana Collepardo-Guevara, Guillem Portella, Michele Vendruscolo, Daan Frenkel, Tamar Schlick, and Modesto Orozco. Chromatin unfolding by epigenetic modifications explained by dramatic impairment of internucleosome interactions: A multiscale computational study. *Journal of the American Chemical Society*, 137(32), 2015. ISSN 15205126. doi: [10.1021/jacs.5b04086](https://doi.org/10.1021/jacs.5b04086).
- [196] Stephen E. Farr, Esmée J. Woods, Jerelle A. Joseph, Adiran Garaizar, and Rosana Collepardo-Guevara. Nucleosome plasticity is a critical element of chromatin liquid–liquid phase separation and multivalent nucleosome interactions. *Nature Communications*, 12(1):1–17, 2021. ISSN 20411723. doi: [10.1038/s41467-021-23090-3](https://doi.org/10.1038/s41467-021-23090-3).
- [197] Michael S. Cosgrove and Cynthia Wolberger. How does the histone code work? *Biochemistry and Cell Biology*, 83(4):468–476, 2005. ISSN 08298211. doi: [10.1139/o05-137](https://doi.org/10.1139/o05-137).
- [198] Erica L. Mersfelder and Mark R. Parthun. The tale beyond the tail: Histone core domain modifications and the regulation of chromatin structure. *Nucleic Acids Research*, 34(9):2653–2662, 2006. ISSN 03051048. doi: [10.1093/nar/gkl338](https://doi.org/10.1093/nar/gkl338).

- [199] Simon Nadal, Ritu Raj, Shabaz Mohammed, and Benjamin G. Davis. Synthetic post-translational modification of histones. *Current Opinion in Chemical Biology*, 45:35–47, 2018. ISSN 18790402. doi: 10.1016/j.cbpa.2018.02.004.
- [200] Scott B. Rothbart and Brian D. Strahl. Interpreting the language of histone and DNA modifications. *Biochimica et Biophysica Acta - Gene Regulatory Mechanisms*, 1839(8):627–643, 2014. ISSN 18764320. doi: 10.1016/j.bbagr.2014.03.001.
- [201] Michael S. Cosgrove, Jef D. Boeke, and Cynthia Wolberger. Regulated nucleosome mobility and the histone code. *Nature Structural and Molecular Biology*, 11(11):1037–1043, 2004. ISSN 15459993. doi: 10.1038/nsmb851.
- [202] Bing Li, Michael Carey, and Jerry L. Workman. The Role of Chromatin during Transcription. *Cell*, 128(4):707–719, 2007. ISSN 00928674. doi: 10.1016/j.cell.2007.01.015.
- [203] Tony Kouzarides. Chromatin Modifications and Their Function. *Cell*, 128(4):693–705, 2007. ISSN 00928674. doi: 10.1016/j.cell.2007.02.005.
- [204] Catherine A. Musselman, Marie Eve Lalonde, Jacques Côté, and Tatiana G. Kutateladze. Perceiving the epigenetic landscape through histone readers. *Nature Structural and Molecular Biology*, 19(12):1218–1227, 2012. ISSN 15459993. doi: 10.1038/nsmb.2436.
- [205] Catherine A. Musselman, Matthew D. Gibson, Erik W. Hartwick, Justin A. North, Jovylyn Gatchalian, Michael G. Poirier, and Tatiana G. Kutateladze. Binding of PHF1 Tudor to H3K36me3 enhances nucleosome accessibility. *Nature Communications*, 4, 2013. ISSN 20411723. doi: 10.1038/ncomms3969.
- [206] Matthew D. Gibson, Jovylyn Gatchalian, Andrew Slater, Tatiana G. Kutateladze, and Michael G. Poirier. PHF1 Tudor and N-terminal domains synergistically target partially unwrapped nucleosomes to increase DNA accessibility. *Nucleic Acids Research*, 45(7):3767–3776, 2017. ISSN 13624962. doi: 10.1093/nar/gkw1320.
- [207] Lacramioara Bintu, Toyotaka Ishibashi, Manchuta Dangkulwanich, Yueh Yi Wu, Lucyna Lubkowska, Mikhail Kashlev, and Carlos Bustamante. Nucleosomal elements that control the topography of the barrier to transcription. *Cell*, 151(4):738–749, 2012. ISSN 00928674. doi: 10.1016/j.cell.2012.10.009.
- [208] Dorota Komar and Przemyslaw Juszczynski. Rebelled epigenome: histone H3S10 phosphorylation and H3S10 kinases in cancer biology and therapy. *Clinical Epigenetics*, 12(1):1–14, 2020. ISSN 18687083. doi: 10.1186/s13148-020-00941-2.
- [209] Yuri L. Lyubchenko. Direct AFM visualization of the nanoscale dynamics of biomolecular complexes. *Journal of Physics D: Applied Physics*, 51, 2018. ISSN 13616463. doi: 10.1088/1361-6463/aad898.
- [210] Tine Brouns, Herlinde De Keersmaecker, Sebastian F. Konrad, Noriyuki Kodera, Toshio Ando, Jan Lipfert, Steven De Feyter, and Willem Vanderlinden. Free Energy Landscape and Dynamics of Supercoiled DNA by High-Speed Atomic Force Microscopy. *ACS Nano*, 12(12):11907–11916, dec 2018. ISSN 1936086X. doi: 10.1021/acsnano.8b06994.
- [211] William Hadley Richardson. Bayesian-Based Iterative Method of Image Restoration. *Journal of The Optical Society of America*, 62(1):55–59, 1972. ISSN 03915603. doi: 10.5301/RU.2013.11151.
- [212] L. B. Lucy. An iterative technique for the rectification of observed distributions. *The Astronomical Journal*, 79(6):745–754, 1974. ISSN 00046256. doi: 10.1086/111605.
- [213] M. Soledad Ivaldi, Caline S. Karam, and Victor G. Corces. Phosphorylation of histone H3 at Ser10 facilitates RNA polymerase II release from promoter-proximal pausing in *Drosophila*. *Genes and Development*, 21(21):2818–2831, 2007. ISSN 08909369. doi: 10.1101/gad.1604007.

- [214] Grant A. Hartzog and John W. Tamkun. A new role for histone tail modifications in transcription elongation. *Genes and Development*, 21(24):3209–3213, 2007. ISSN 08909369. doi: [10.1101/gad.1628707](https://doi.org/10.1101/gad.1628707).
- [215] Alexander Gansen, Katalin Tóth, Nathalie Schwarz, and Jörg Langowski. Opposing roles of H3- and H4-acetylation in the regulation of nucleosome structure - A FRET study. *Nucleic Acids Research*, 43(3):1433–1443, 2015. ISSN 13624962. doi: [10.1093/nar/gku1354](https://doi.org/10.1093/nar/gku1354).
- [216] D. A. Potoyan and G. A. Papoian. Regulation of the H4 tail binding and folding landscapes via Lys-16 acetylation. *Proceedings of the National Academy of Sciences*, 109(44):17857–17862, 2012. ISSN 0027-8424. doi: [10.1073/pnas.1201805109](https://doi.org/10.1073/pnas.1201805109).
- [217] Eric J. Wagner and Phillip B. Carpenter. Understanding the language of Lys36 methylation at histone H3. *Nature Reviews Molecular Cell Biology*, 13(2):115–126, 2012. ISSN 14710072. doi: [10.1038/nrm3274](https://doi.org/10.1038/nrm3274).
- [218] Sushmita Roy, Jason Ernst, Peter V Kharchenko, Pouya Kheradpour, Nicolas Negre, Matthew L Eaton, Jane M Landolin, Christopher A Bristow, Lijia Ma, Michael F Lin, Stefan Washietl, I Bradley, Ferhat Ay, Patrick E Meyer, Nicolas Robine, L Nicole, Luisa Di Stefano, Eugene Berezikov, Christopher D Brown, Rogerio Candeias, Joseph W Carlson, Adrian Carr, Irwin Jungreis, Rachel Sealfon, Michael Y Tolstorukov, Sebastian Will, A Artyom, Carlo Artieri, Benjamin W Booth, Angela N Brooks, Qi Dai, A Carrie, Philipp Kapranov, Renhua Li, Heather K Macalpine, John Malone, Akiko Sakai, Anastasia Samsonova, Jeremy E Sandler, and Yuri B Schwartz. Identification of Functional Elements and Regulatory Circuits by Drosophila modENCODE. *Science*, 330(6012):1787–1797, 2010. doi: [10.1126/science.1198374](https://doi.org/10.1126/science.1198374). Identification.
- [219] Peter V. Kharchenko, Artyom A. Alekseyenko, Yuri B. Schwartz, Aki Minoda, Nicole C. Riddle, Jason Ernst, Peter J. Sabo, Erica Larschan, Andrey A. Gorchakov, Tingting Gu, Daniela Linder-Basso, Annette Plachetka, Gregory Shanower, Michael Y. Tolstorukov, Lovelace J. Luquette, Ruibin Xi, Youngsook L. Jung, Richard W. Park, Eric P. Bishop, Theresa K. Canfield, Richard Sandstrom, Robert E. Thurman, David M. MacAlpine, John A. Stamatoyannopoulos, Manolis Kellis, Sarah C.R. Elgin, Mitzi I. Kuroda, Vincenzo Pirrotta, Gary H. Karpen, and Peter J. Park. Comprehensive analysis of the chromatin landscape in *Drosophila melanogaster*. *Nature*, 471(7339):480–486, 2011. ISSN 00280836. doi: [10.1038/nature09725](https://doi.org/10.1038/nature09725).
- [220] Sabine M. Görisch, Malte Wachsmuth, Katalin Fejes Tóth, Peter Lichter, and Karsten Rippe. Histone acetylation increases chromatin accessibility. *Journal of Cell Science*, 118(24):5825–5834, 2005. ISSN 00219533. doi: [10.1242/jcs.02689](https://doi.org/10.1242/jcs.02689).
- [221] Tadasu Nozaki, Ryosuke Imai, Mai Tanbo, Ryosuke Nagashima, Sachiko Tamura, Tomomi Tani, Yasumasa Joti, Masaru Tomita, Kayo Hibino, Masato T. Kanemaki, Kerstin S. Wendt, Yasushi Okada, Takeharu Nagai, and Kazuhiro Maeshima. Dynamic Organization of Chromatin Domains Revealed by Super-Resolution Live-Cell Imaging. *Molecular Cell*, 67(2):282–293.e7, 2017. ISSN 10974164. doi: [10.1016/j.molcel.2017.06.018](https://doi.org/10.1016/j.molcel.2017.06.018).
- [222] Neil Macdonald, Julie P.I. Welburn, Martin E.M. Noble, Anhco Nguyen, Michael B. Yaffe, David Clynes, Jonathan G. Moggs, George Orphanides, Stuart Thomson, John W. Edmunds, Alison L. Clayton, Jane A. Endicott, and Louis C. Mahadevan. Molecular basis for the recognition of phosphorylated and phosphoacetylated histone H3 by 14-3-3. *Molecular Cell*, 20(2):199–211, 2005. ISSN 10972765. doi: [10.1016/j.molcel.2005.08.032](https://doi.org/10.1016/j.molcel.2005.08.032).
- [223] Anna Sawicka and Christian Seiser. Sensing core histone phosphorylation - A matter of perfect timing. *Biochimica et Biophysica Acta - Gene Regulatory Mechanisms*, 2014. ISSN 18764320. doi: [10.1016/j.bbagr.2014.04.013](https://doi.org/10.1016/j.bbagr.2014.04.013).
- [224] John A. Latham and Sharon Y.R. Dent. Cross-regulation of histone modifications. *Nature Structural and Molecular Biology*, 14(11):1017–1024, 2007. ISSN 15459993. doi: [10.1038/nsmb1307](https://doi.org/10.1038/nsmb1307).

- [225] Qing Duan, Haobin Chen, Max Costa, and Wei Dai. Phosphorylation of H3S10 blocks the access of H3K9 by specific antibodies and histone methyltransferase: Implication in regulating chromatin dynamics and epigenetic inheritance during mitosis. *Journal of Biological Chemistry*, 283(48):33585–33590, 2008. ISSN 00219258. doi: [10.1074/jbc.M803312200](https://doi.org/10.1074/jbc.M803312200).
- [226] Peter Cheung, Kirk G. Tanner, Wang L. Cheung, Paolo Sassone-Corsi, John M. Denu, and C. David Allis. Synergistic coupling of histone H3 phosphorylation and acetylation in response to epidermal growth factor stimulation. *Molecular Cell*, 5(6):905–915, 2000. ISSN 10972765. doi: [10.1016/S1097-2765\(00\)80256-7](https://doi.org/10.1016/S1097-2765(00)80256-7).



# A

## Protocols

### A.0.1 PCR for nucleosome reconstitution

Polymerase chain reaction was used to amplify the linear DNA constructs ordered at and delivered from ThermoFisher Scientific GeneArts (*Strings DNA fragments*). Primers were designed using *SnapGene* and ordered at Eurofins.

#### Step 1: Mix components

When preparing content for multiple PCR eppis, mix everything in a large eppi and then aliquot to several PCR reaction tubes. PCR mix per PCR eppendorf tube (20  $\mu$ L):

1. 1  $\mu$ L forward primer (at concentration of 10  $\mu$ M, 500 nM are required in the final 20  $\mu$ l mix. Primer was delivered dry and diluted to 100  $\mu$ M for long term storage in the -20 °C freezer.)
2. 1  $\mu$ L reverse primer (same concentration as forward primer).
3. 1  $\mu$ L 486 bp template DNA fragment (at concentration of 1.3 ng/ $\mu$ L, final concentration of 0.065 ng/ $\mu$ L in 20  $\mu$ l mix required. DNA fragments originally delivered dry and subsequently brought to required concentration by resuspension with ddH<sub>2</sub>O and stored at -20 °C.)
4. 7  $\mu$ L ddH<sub>2</sub>O.
5. 10  $\mu$ L 2 x Pfu Master Mix (ordered at biotechrabbit).

#### Notes:

1. Pfu polymerase is a rather old-school polymerase that is a little slower than for example Phusion polymerase. However, I tried to perform PCR with the Phusion master mix several times and the results (band width in the gel and final concentration) were the same or better for the Pfu master mix.
2. The protocol can be easily adapted to shorter or longer DNA templates.
3. To obtain sufficient amounts of DNA for subsequent nucleosome reconstitution (3  $\mu$ g of DNA necessary for each NR reaction tube) I usually performed PCR on 16 x 20  $\mu$ L eppis and afterwards added everything together. More than 16 eppis does not make sense since during PCR clean up (Step 3) only a limited amount of DNA can be caught in the membrane which is already maxed out at 16 eppis.

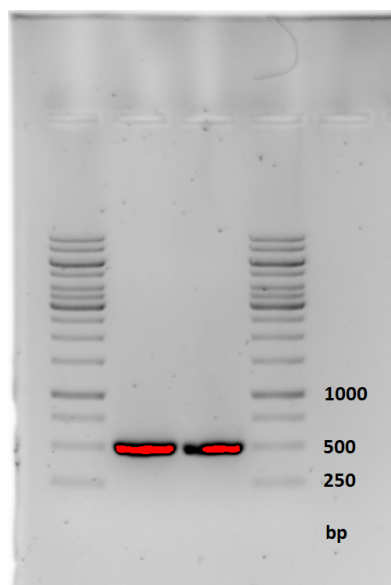


**Figure A.1:** Agarose gel to test DNA quality after PCR. Column 1 and 4 show the reference 1 kb DNA ladder and columns 2 and 3 show the purified 486 bp DNA construct after PCR purification. Red color indicates saturated pixel when measuring the gel in the GelDoc.

### Step 2: Thermocycling

Place the PCR tubes in the thermocycler and let it run with the following cycling settings:

1. 95 °C for 3 minutes
2. 95 °C for 30 seconds
3. 52 °C for 30 seconds
4. 72 °C for 1 minute
5. 72 °C for 15 minutes
6. 4 °C storage hold

Repeat cycling steps 2-4 for 35 times consecutively.

### Step 3: PCR purification

PCR purification was performed using a QIAGEN PCR purification kit. The steps here describe the case of using 16 x 20  $\mu$ L eppis for PCR.

1. Place the volume of all 16 PCR eppis in one large 2 mL eppi (total of 320  $\mu$ L PCR reaction volume). Add 5x the volume of PB buffer (1600  $\mu$ L) and mix thoroughly.
2. Use the spin column from the PCR kit in three consecutive rounds each time with 640  $\mu$ L of the mix. The maximum volume of the column is around 800  $\mu$ L and thus it is not possible to do it in one round. Spin down at 13000 rpm over 1 minute and discard the flow-through.

3. Use 750  $\mu\text{L}$  PE buffer to wash everything. Spin it twice at 13000 rpm over 1 minute and discard flow-through inbetween.
4. Use ddH<sub>2</sub>O (instead of the delivered elution buffer EB) to elute the DNA into a new DNA low-bind eppi. Depending on the required final DNA concentration, elution can be performed with either 30  $\mu\text{L}$  or 50  $\mu\text{L}$  ddH<sub>2</sub>O. with 30  $\mu\text{L}$  I usually obtained final concentrations of 300-400 ng/ $\mu\text{L}$  and with 50  $\mu\text{L}$  of 200-250 ng/ $\mu\text{L}$ .

#### **Step 4: DNA quality control**

To check DNA quality after PCR, run an agarose gel and measure the DNA concentration in the NanoDrop. I usually made a 1 % agarose gel, stained it with 2  $\mu\text{L}$  of RotiSafe gel stain and let the gel run for 30-35 minutes at 100 V. As a reference, I used a 1 kb DNA ladder. For the DNA sample, I typically mixed 0.5  $\mu\text{L}$  5x loading dye with 2  $\mu\text{L}$  DNA sample to save sample volume. (see Fig. A.1)

### A.0.2 Nucleosome reconstitution

The nucleosome reconstitution is performed according to a previously published protocol<sup>149</sup>. Histones and DNA are all added together at high salt concentrations and over the course of 15 hours the salt concentration is reduced such that the nucleosomes can form. Before starting with this protocol, prepare the DNA according to the PCR protocol and make sure that enough histones are in stock.

#### Step 1: Buffer stocks

Three different buffers are necessary in total:

1. 1x high-salt buffer (2 M NaCl, 10 mM TRIS, 1 mM EDTA) - 1 L
2. 10x low-salt buffer (50 mM NaCl, 10 mM TRIS, 1 mM EDTA) - 1 L
3. 2.4x high-salt buffer (2 M NaCl, 10 mM TRIS, 1 mM EDTA) - 100 mL

Bring all buffers to pH 7.6 at room temperature and afterwards filter them through a hydrophilic filter with a vacuum pump.

#### Notes:

1. Prepare stock solutions of the 1x HS buffer and the 10x LS buffer of 1 L. 300 mL of the HS buffer and 400 mL of the LS buffer are required for one nucleosome reconstitution. While the buffers should be used soon after preparation, several reconstitutions can be performed with the same batch of buffers when used within a few weeks.
2. In the original protocol, 2x HS buffer instead of 2.4x HS buffer is used for sample mixing. However, I found it easier to use 2.4x HS buffer and thus have more space for the other materials such as DNA and nucleosomes. 2.4x HS is the highest concentration of salt I was able to achieve to still have the salt properly dissolved in the mix.

#### Step 2: Buffer beakers for overnight dialysis

All beakers should be cleaned properly by rinsing with ethanol/isopropanol and subsequently washed with mQ. A 3 L and a 5 L beaker are necessary.

1. Prepare the LS buffer in a 3 L beaker. The original protocol says 3 L of total buffer volume but due to the limited volume of the beaker I usually prepared 2.9 L of the LS buffer: 290 mL 10x LS stock + 2610 mL mQ. Add 1.45 mL 100% Triton to the buffer and mix well with a magnetic stirrer. Seal the beaker with parafilm and put the beaker with the buffer into the cold room such that it cools down to 4 °C before starting the nucleosome reconstitution. Shortly before starting the reconstitution, add 300 µL beta-mercapthoethanol to the and mix.
2. Prepare the HS buffer in a 5 L beaker (300 mL of the previously prepared stock solution). Add 150 µL of Triton 100%. Since it is difficult to pipette small volumes of 100% Triton due to its viscosity, I usually dilute the Triton before to a concentration of 20% or so and then add the required amount. Again, seal the beaker with parafilm and put it into the cold room to cool down to 4 °C before starting the reconstitution.

*Notes:*

1. Triton does not dissolve properly at 4 °C so make sure to prepare the buffer/Triton solutions before cooling the buffer in the cold room.
2. In the original protocol it says that Igepal instead of Triton should be used. However, we tested the protocol with Triton (due to a lack of Igepal in the lab) and it worked fine.

**Step 3: Prepare setup for overnight dialysis**

1. Place the two beakers with the LS and HS buffer on a magnetic stirring plate each in the cold room. Take a peristaltic pump that is later used to transfer the buffer from one beaker to the other and place on something high (I usually used empty ice boxes) such that it is located at the same height as the beakers.
2. Place the tubing of the peristaltic pump in such a manner that the tubing reaches the bottom of the LS buffer beaker. (It needs to be able to transfer all the volume) Additionally, make sure that the tubing is fixed to the inner side of the HS beaker such that the transferred fluid flows on the glass and does not contaminate the freely floating sample by accident.
3. Add 300  $\mu\text{L}$   $\beta$ -mercaptoethanol to each beaker and set the magnetic stirring to a continuous low frequency stirring. Seal the beakers thoroughly with the parafilm.

**Step 4: Dialysis chambers**

With the buffer beakers set up and cooled down, it is time to prepare the dialysis chambers that contain the DNA and histones. Compared to the 100  $\mu\text{L}$  sample volume mentioned in the 2012 protocol<sup>149</sup>, I always used 30  $\mu\text{L}$  sample volume. This will result in plenty of nucleosomes for measurements (>50 surface depositions) and save materials. Each chamber contains:

1. 12.5  $\mu\text{L}$  2.4x HS buffer
2. 0.5  $\mu\text{L}$  Triton (3 %)
3. 0.5  $\mu\text{L}$  BSA (12  $\mu\text{g}/\mu\text{L}$ )- BSA diluted in milliQ shortly before the reconstitution.
4. 3  $\mu\text{g}$  DNA (of 486 bp DNA)
5. 1  $\mu\text{g}$  histone octamers
6. X  $\mu\text{L}$  milliQ to fill up to 30  $\mu\text{L}$

*Notes:*

1. By using only 0.5  $\mu\text{L}$  of volume for Triton and BSA at high concentrations there is more space for DNA in case that DNA concentrations were low after PCR.

2. I usually added everything but the histones together in a protein lobind eppi, mixed it gently and then transferred it to an eppi with the histones. There, I only mix gently by stirring with the pipette.
3. Make sure that the membranes do not touch anything to avoid contamination. A good way to fill the membranes is by placing the membranes in a floater and putting the floater on the top of a small beaker such that the membranes cannot get in contact with anything.

### Step 5: Overnight dialysis

After preparing the beakers and the pump in the cold room, add 300  $\mu\text{L}$  beta-mercaptoethanol to the low salt buffer, close it again and mix well with the magnetic stirring plate. Place the floater with the dialysis chambers in it on the high-salt buffer in a way that the stirrer is slowly mixing everything while not moving the floater with the samples around. It is important to not have any air bubbles on the dialysis membranes in the buffer that could disturb the proper exchange of the buffer through the dialysis membranes.

Finally, add 300  $\mu\text{L}$  beta-mercaptoethanol to the high-salt buffer. Close everything and turn on the peristaltic pump such that all the fluid is transferred from the low-salt buffer to the high-salt buffer within 15 hours. Usually, I go check on everything after an hour or so to make sure that the low-salt buffer is properly transferred and to adjust the pumping speed in case that it is too fast or slow.

### Step 6: Transfer to fresh low-salt buffer

After all of the low-salt buffer was transferred to the beaker now containing the mix of the LS and the HS buffer, transfer the floater with the sample containing dialysis chamber to a new beaker containing 1 L of fresh low-salt buffer (again with 300  $\mu\text{L}$  beta-mercaptoethanol). Prepare this buffer from the LS buffer stock that was prepared in the beginning. It makes sense to prepare this buffer already directly when starting the overnight reconstitution and to put it into the cold room sealed with parafilm such that it can already cool down to 4  $^{\circ}\text{C}$  aswell. Keep the samples on the fresh LS buffer for at least 2 hours.

Finally, pipette the samples contained in the dialysis chambers into lobind protein eppis. The volume can vary significantly between chambers and reconstitutions (50  $\mu\text{L}$  to up to 200  $\mu\text{L}$  were quite common). To estimate the volume contained in each eppi it makes sense to use a 20  $\mu\text{L}$  pipette and note the approximate amount of volume transferred. This will help in choosing the right concentration of nucleosomes for subsequent preparation of AFM measurement surfaces.

# Acknowledgements

When printing this dissertation, I will be approximately 3.5 years into my doctoral studies summing up to a total of almost 5 years at the chair when combined with the time that I already spent within the group during my master thesis. During that time I had the chance to meet, get to know and work with a large number of people that all helped in shaping the person I am today and without these people the past 5 years would not have been the same unforgettable experience. Therefore, I'd like to use the next couple of paragraphs to say thank you.

First and foremost, I want to thank **Jan Lipfert**. When I first started my master thesis in your lab 5 years ago, I never considered doing a PhD. However, learning how exciting and fulfilling science can be within that first year in your group made me decide to pursue a doctoral thesis afterwards, a decision that I never regretted within the last couple of years. Thanks for enabling me to stay in science, teaching me a lot about how to write proper scientific articles, always being approachable and in a good mood, and of course also for all the fun conversations over a cold drink after paper submissions or during group outings.

Similarly, I'd like to thank **Willem Vanderlinden** who very much helped me in getting acquainted with my favorite topic of all times: Nucleosomes. Introducing me to a bunch of people in Leuven, never becoming tired of discussing AFM and nucleosomes, and consistently questioning data analysis methods during lunch or after work had a huge impact on my scientific understanding. Thanks for all the patience and jokes you had and made during hours of revisions.

Thanks to **Hermann Gaub** for the great working environment at the institute, the constant positivity and valuable feedback to various topics.

A significant part of the great experiences I made during my PhD happened in Leuven during several measurement stays, conferences and group outings. These outings would not have been as productive and fun as they finally were without all the amazing people I met at the KU Leuven: **Steven De Feyter**, thanks for continuously supporting my research stays at the KU Leuven, providing such a great working atmosphere in the lab and for the fun group outings I was able to join when visiting. **Wout Frederickx**, thanks so much for introducing me to the world of nucleosomes, AFM measurements, lab work in general, and Belgian beer in Leuven while always being patient and a great teacher. **Tine Brouns**, thanks for sharing your desk with me during several AFM measurement campaigns in Leuven and for your hospitality during these stays in general.

During my time in Jan's group, I was lucky to always have an amazing group of like-minded people around me. My deepest gratitude goes to my fellow PhD students who made every day of coming to the office memorable:

**Samuel Stubhan**, you are not only the king of the sky but also the king of office mates. Thanks for an uncountable amount of jokes, good stories, lunches, after work drinks, and always being positive and helpful. I'm looking forward to future uses of the verticoal for manifold occasions.

**Sophia Gruber**, if positivity and enthusiasm combined would get a new word, it should be "Sophia". I couldn't have asked for better company for dozens of ice cream and cake break conversations. Thanks for all the positivity and knowledge you spread around the office always helping to keep up the mood.

**Yi-Yun Lin**, thanks for being my comrade-in-arms with nucleosomes, all the dancing and for introducing me to K-Pop. Your constant laughter is absolutely inspiring and communication is key.

**Adina Hausch**, thanks for making my new office desks a prime spot for your coffee break and the conversations that came along with it. All the luck for your future less magnetic endeavours.

**Pauline Kolbeck**, thanks for being my comrade-in-arms with the AFM. Your positivity definitely added to the great working environment at the chair.

**Magnus Bauer**, the one person that can answer all the questions ever coming up. I admire your fascination for all these different techniques, methods, and tools you are working with. Thanks for your constant helpfulness and patience.

Next, I want to thank **Thomas Zettl**, **Philipp Walker**, **Linda Brützel**, **Franziska Kriegel**, **Steffen Sedlak** and **Leonard Schendel** for always being approachable, helpful and significantly affecting the great working environment at the department.

Similarly, I'd like to thank **Thomas Nicolaus** for making the lab space an enjoyable working environment and **Sylvia Kreuzer**, **Sabine Hohenester** and **Barbara Müller** for always providing help with organizational matters.

I'd also like to thank **Susanne Hennig** and the CeNS Team for organizing multiple awesome events such as the Venice meeting, the JNN, and everything regarding additional training and courses. All of these events were awesome to participate in and without these conferences and events my PhD definitely would have been a less wholesome experience.

Finally, during the last five years my life of course also has taken place outside the chair. My deepest gratitude goes to all the people who supported me along the way: Thanks to my mom, my dad and my family for always being there and for supporting me to study physics in the first place, to Paulina for tirelessly listening to my amazing work stories about publication writing and AFM measurements, and my friends for making PhD jokes and sometimes asking me physics questions.